MAGNETIC TOPOLOGY ANALYSIS OF THE SWITCHED RELUCTANCE MOTOR FOR TORQUE IMPROVEMENT

JINGWEI ZHU

M.Phil

THE HONG KONG POLYTECHNIC UNIVERSITY

2018

The Hong Kong Polytechnic University
Department of Electrical Engineering

Magnetic Topology Analysis of the Switched Reluctance Motor for Torque Improvement

Jingwei ZHU

A thesis submitted in partial fulfilment of the requirements for the degree of Master of Philosophy

August, 2017

CERTIFICATE OF ORIGINALITY

I hereby declare that this thesis is my own work and that, to the best of my knowledge and belief, it reproduces no material previously published or written, nor material that has been accepted for the award of any other degree or diploma, except where due acknowledgement has been made in the text.

_____(Signed)

Jingwei ZHU (Name of student)

Abstract

Various motors have been investigated for electric vehicle (EV) application, namely the brushed and brushless DC motor, induction motor, permanent magnet (PM) motor. Each of the above motors, however, have its own deficiency. The switched reluctance motor (SRM) has superior features of simple, robust structure, low cost and better fault tolerance. Therefore, it a better candidate for EV application.

However, limitation of the SRM is relatively lower torque density in comparison with the PM motor. In this thesis, two topologies of in-wheel motors based on switched reluctance principle are proposed to enhance the torque density. The first topology combines the idea of multi-tooth per stator pole and more rotor poles than stator teeth together. The magnetic principle of the proposed topology is analyzed initially for torque improvement. Then, the structure determination is made, including number of teeth per stator pole, number of rotor poles and number of phase, on the basis of higher torque output and efficiency. Moreover, the motor topology is optimized by genetic algorithm (GA) and equivalent magnetic circuit (EMC) model, while taking the design constraints for SRMs into consideration. The EMC model is utilized to obtain the value of self-inductance based on the calculation of different magnetic flux lines. The formula of fitness function, which focuses on specific torque and torque per unit of copper loss, can be defined from the calculation result of the self-inductance for GA optimization.

A new hybrid reluctance motor by inserting permanent magnets between adjacent

stator poles of a multi-teeth SRM is put forward as the second topology. The operations are based on switched reluctance principle and the direction of winding configuration on adjacent phases is reversed corresponding to the magnetization direction of PMs. The function of PMs is not only to increase the flux quantity in the airgap, but also to regulate the flux density in the stator pole, reducing the saturation, to enhance the torque output. Then, the structural analysis is carried out to determine the shape of stator pole by using FEM, which concentrates on lower magnetic saturation. In addition, the optimization process is also on the basis of EMC model and GA method. Unlike SRMs, the EMC model of this topology takes the effect of PMs into consideration. For GA method, the objective function based on highest specific torque is obtained by EMC model calculation. With the design constraints for motors and some constant parameters considered, multi-variable optimization is implemented for the maximum value of objective function.

After that, a motor with a smaller size and the same working principle of the hybrid reluctance topology is manufactured for high torque density experimental verification. The motor is an outer stator and inner rotor topology, designed and optimized by EMC model and GA method for the best torque performance. The static torque performance are measured and compared with FEM results. Besides, the torque-speed and output power-speed curves can be obtained from the experimental measurement. The experimental results demonstrate that the prototype can achieve high torque density, power output and efficiency.

Publications

Journal Papers

1. **Jingwei Zhu**, Ka Wai Eric Cheng, Xiangdang Xue, Yu Zou, "Design of a New Enhanced Torque In-Wheel Switched Reluctance Motor with Divided Teeth for Electric Vehicles", *IEEE Trans. Magn.*, vol 53, no. 11, 2017.

2. **Jingwei Zhu**, Ka Wai Eric Cheng, and Xiangdang Xue, "Design and Analysis of a New Enhanced Torque Hybrid Switched Reluctance Motor", *IEEE Trans. Energy Convers.* (Special issue, abstract accepted, full paper submitted)

3. J. F. Pan, Li Qiu, **J. Zhu**, Eric Cheng, Bo Zhang, "Optimal Positioning Coordination for Multiple Linear Switched Reluctance Machines", *IEEE Trans. Magn.*, vol 53, no. 11, 2017.

4. Siyang Li, Ka Wai Eric Cheng, **Jingwei Zhu**, Yulong Fan, Yu Zou, "Design and Application of a Decoupled Rotary-Linear Switched Reluctance Motor for Concentrated Photovoltaic Power Generation", *IET Elect. Power Appl.* (Accepted)

Conference Papers

1. **Jingwei Zhu**, Ka Wai Eric Cheng, Xiangdang Xue, Yu Zou, "A Novel Hybrid Reluctance Motor with Multiple Teeth per Stator Pole for In-wheel Applications", oral presentation at International Magnetics Conference (Intermag 2017), Dublin, Ireland, 2017.

2. **Jingwei Zhu**, K. W. E Cheng, Xiangdang Xue**,** "Torque Analysis for In-wheel

Switched Reluctance Motors with Varied Number of Rotor Poles", 2016 International Symposium on Electrical Engineering (ISEE), Hong Kong, 2016.

3. **Jingwei Zhu**, K. W. E Cheng, "Energy Factor Analysis for Switched Reluctance Motors Under Various Conditions", 2015 6th International Conference on Power Electronics Systems and Applications (PESA), Hong Kong, 2015.

4. **Jingwei Zhu**, Ka Wai Eric Cheng, Xiangdang Xue, "Comparison Study of rare-earth-free motors with permanent magnet motors in EV applications", 2017 7th International Conference on Power Electronics Systems and Applications (PESA), Hong Kong, 2017.

Acknowledgement

First of all, I would like to express my sincere gratitude and respect to my supervisor, Prof. Ka Wai Eric Cheng, for his invaluable instruction and support throughout my MPhil research period.

Then, I would like to appreciate the academic help from Dr. Xiangdang Xue. His guidance and experience in motor design & control are quite useful for me.

Moreover, I would like to thank Mr. Yulong Fan for his great patience and assistance in motor manufacture process. Special thanks go to teachers and colleagues in the Electric Vehicle Laboratory, the Hong Kong Polytechnic University, including Mr. K. Y. Tse, Mr. Daohong Wang, Mr. Jones Chan, Dr. Cuidong Xu, Mr. Yu Zou, Ms. Xiaolin Wang, Mr. Siyang Li, Mr. Yat Chi Fong, Mr. Raghu Raman, Mr. William Fan Chen, Mr. Manxin Chen, Mr. Jie Mei, Mr. Wenbin Qi and Dr. Junfeng Liu.

I also gratefully thank to the Research Office, the Hong Kong Polytechnic University, for the financial support of my study.

Last but not least, I must deeply thank my parents with regards to their generous love and spirit encouragement staying with me all along to complete my study.

Contents

List of Figures

List of Tables

List of Acronyms

EV	Electric vehicle
ICE	Internal combustion engine
DC	Direct current
PM	Permanent magnet
PID	Proportion Integration Differentiation
IM	Induction motor
AC	Alternating current
PMSM	Permanent magnet synchronous motor
FSM	Flux switching motor
SRM	Switched reluctance motor
FEM	Finite element method
FEA	Finite element analysis
IGBT	Insulated Gate Bipolar Translator
SCR	Silicon Controlled Rectifier
MMF	Magnetic motive force
GA	Genetic algorithm
EMC	Equivalent magnetic circuit
RMS	Root Mean Square
KVL	Kirchhoff’s Voltage Law
KCL	Kirchhoff’s Current Law

List of Symbols

T_e	Electromagnetic torque
W_m, W_f	Co-energy and energy storage
θ	Angle position
λ	Flux linkage
i	Phase current
L	Inductance
e	Input voltage
θ_s, θ_r, θ_{slot}	Arc angle of stator tooth, rotor pole, stator inner slot
N_r	Number of rotor poles
l	Length
r	Radius
Φ	Magnetic flux
F	Magnetic motive force
R	Magnetic reluctance
B	Flux density
H	Magnetic field intensity
A	Average cross area
h	Height
D	Diameter

Chapter 1

Introduction

In the past few decades, the transportation systems in the world are becoming necessary tools for mankind. The key transportation system is still based on petroleum because of the mature technology in internal combustion engine. However, due to lower efficiency of inner combustion engines, various kinds of toxic substances and greenhouse gases, like carbon dioxide and NO_x, are emitted into the air. Also, the shortage and unstable supply of nonrenewable resources, mainly fossil fuels, together with air pollution and global warming, trigger the demands in development of next generation of electric vehicles (EVs) [1].

According to [2], 27% global energy consumption derives from the transportation sector. EVs have the capability of reducing energy consumption due to its inherit high performance in power conversion [3]. In EVs, electrical machines replace conventional internal combustion engines which have poor efficiency.

In this chapter, motors based on switched reluctance principle are examined. Background discussion on different kinds of dynamic devices to drive the vehicles is described. Then, different types of motors for the application of EVs are discussed. Moreover, the importance of a suitable motor for EVs is illustrated and the organization of the whole thesis is outlined.

1.1 Background

The appearance of the automobile dates back to around 1672 [4]. It can be classified into three main types based on its engine after decades of development: internal combustion engine, hybrid and electric type.

The most dominant power supply installed on the car is the internal combustion engine (ICE) because of its long time history, mature technology and massive production. It is an engine where the combustion of one or more kinds of fuels occur with air in a combustion chamber. Then, the high temperature and pressure gases apply direct force to a moveable part, usually pistons, of the engine. The part is pushed over a distance, transforming chemical energy into useful mechanical energy [5]. The major fuel type is petrol, also known as gasoline, in the area of transportation [6]. Most engine's thermodynamic efficiency, however, is usually less than 40%. For vehicle application, it may be even less than 20%. Furthermore, the incomplete burning of fuels not only sacrifices the efficiency, but causes toxic emissions, such as CO, NO_x, as well, that pollutes the environment.

To improve the energy conversion process, substantial research has been conducted: a fuel injection method is utilized to improve air fuel ratio [7]. Diesel fuel has been an alternative for gasoline due to the advantage of higher fuel efficiency [8]. It, however, increases the noise of the system. The turbocharger was introduced into automobiles to increase efficiency and power output by circulating exhaust gas [9]. Utilizing exhaust gas for power generation is put forward [10-12]. The efficiency has been improved, but slightly.

The natural gas automobile becomes a cleaner and cheaper alternative due to its low emission and widespread resources [13]. Large amount of investigation has been made for natural gas application to vehicles [14-18]. But efficiency is not improved compared with gasoline engines and low compression ratio may cause cropping of delivered power. Also, the emission of global warming gas, carbon dioxide, is not decreased.

Hybrid vehicles utilize two or more types of power sources, usually ICE plus electric machines [19]. It has the advantages of regenerative braking, dual power and automatic start to improve efficiency and performance [20]. Several scholars have conducted deep research into this field to achieve low energy consumption and improve fuel economy by introducing advanced control or management method into the multisource system [21-24]. Nevertheless, this kind of automobile does not realize zero emission in the urban city and its cost is quite high.

The electric vehicle is a new trend for the focus on renewable energy and increasing its proportion in the market in the 21st century. Further analysis and experiments are carried out to strengthen the battery life, efficiency and performance of the whole vehicles [25-29]. Also, the efficiency of electric motors is much higher than that of ICE. The greatest advantage, which determines its rapid increase in transportation, over other automobiles is achieving zero road side emission.

1.2 Literature Review

1.2.1 Driven Motors for Electric Vehicles

A. DC Motor

It is the simplest type of motor to convert mechanical energy into electricity. It is widely used in the early stage of EVs as a result of its low cost and high reliability. The principle of it is shown in Fig. 1-1, which contains a commutator and two brushes to ensure continuous performing. The converter for the DC motor is also simple as shown in Fig. 1-2: with Q1, Q4 on, Q2, Q3 off, positive rotation; with Q2, Q3 on, Q1, Q4 off, negative rotation; with Q1, Q3 on or Q2, Q4 on, free-wheeling mode. Some improvements in the control system of DC motor are proposed in [30-31]. However, because of the existence of carbon brushes and the commutator, the life-span is low. Furthermore, the weight and size is quite large with lower efficiency compared with other kinds of machines [32].

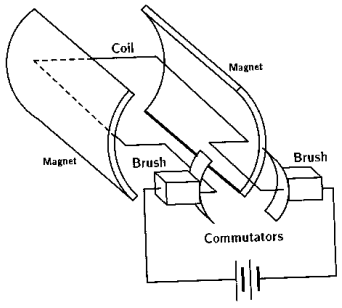

Fig. 1-1 Principle of the DC motor [33]

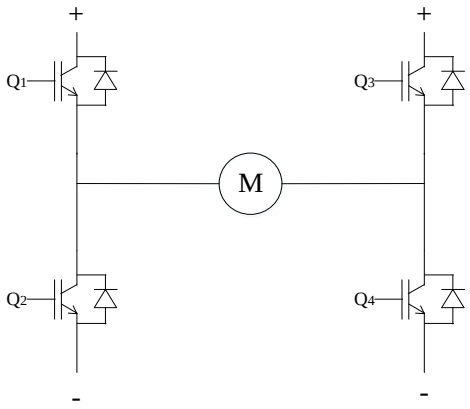

Fig. 1-2 Converter of the DC motor

B. Brushless DC Motor

It merged in the 1960s following the advancement in solid state technology [34]. Better permanent magnet (PM) materials give further improvement to its performance. Due to the structure of no brushes or commutators, the life-span is long. Moreover, it has several other advantages over brushed DC motor, including high specific torque, efficiency, torque density and reduced noise. The schematic and converter circuit of a three phase six state brushless DC motor can be obtained from Fig. 1-3 and Fig. 1-4, respectively. To further improve the energy conversion efficiency, much study is conducted in this field. A position sensor-less and hybrid terminal sliding mode control have been proposed in [35] to enhance the dynamic performance and robust stability with more recovered energy. Research on the regenerative braking system containing fuzzy logic, PID method and artificial neutral network is carried out to take advantage of the maximum kinetic energy in [36-37]. The drawback of this kind of motor is that the cost is high, including power electronics circuit and PM materials.

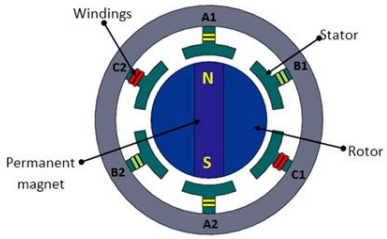

Fig. 1-3 Schematic of a brushless DC motor [38]

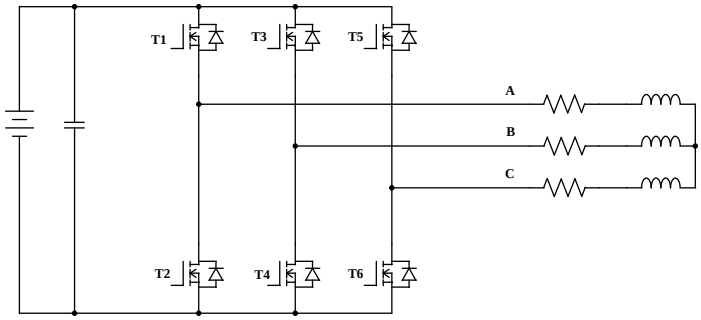

Fig. 1-4 Converter circuit for a brushless DC motor

C. Induction Motor

Unlike the above two DC motors, the induction motor (IM) is an AC electric motor usually with three phases. It can be classified into a wound type and a squirrel-cage type. A prototype of it is shown in Fig. 1-5. Its advantage is that it contains no rare earth materials which are quite limited and expensive. The efficiency is also improved compared with a brushed DC motor. A loss model of the induction motor is proposed in [39] to minimize loss and ensures a high efficiency. A speed sensor-less control without a current controller for the IM is put forward in [40] to reduce the cost. A high performance IM drive is invented in [41] by adopting the maximum torque per ampere control to improve energy efficiency. A current control strategy for performance improvement in the flux weakening region for the IM is proposed in [42]. A sensor-less control combining the idea of vector and sliding mode control is mentioned in [43]. All the researches above enhance the performance of IMs.

But there are some shortcomings for this kind of machine: windings on the rotor making the structure more complex, insufficient torque density and specific torque, relatively low power factor although many improvements have been made.

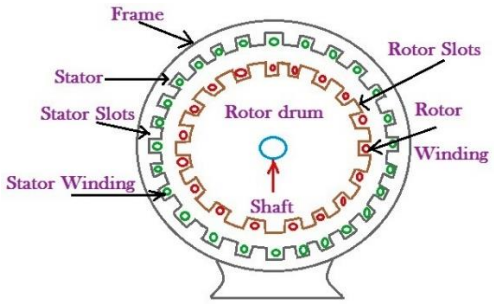

Fig. 1-5 A prototype of the IM [44]

D. PM Motor

This type can be classified into two research categories: permanent magnet synchronous motor (PMSM) and flux switching motor (FSM). Because of the utilization of NdFeB material, it is around two percent more efficient than the highest efficient IMs. The prototype of a surface-mounted and interior PMSM can be obtained from Fig. 1-6 (a) and (b). The PM motor has the feature of smaller size, higher torque and efficiency. This is the reason why the most experiments and investigations have been conducted in this field. Some methods of diagnosis and reduction of noise for PMSM are proposed in [45-47]. Documents [48-49] described the invention of novel fault diagnosis and tolerant control methods for normal operation. Some calculation and control techniques to optimize the performance of the motor are introduced in [50-51]. Some design optimization and novel topologies of PMSM have been put forward in [52-56]. The contributions to this area make the PMSM a high performance candidate for EVs. But the existence of PMs introduces more cogging torque and

induced voltage in the stator windings due to the fluctuation of the rotor, which is unsafe for electric mobility.

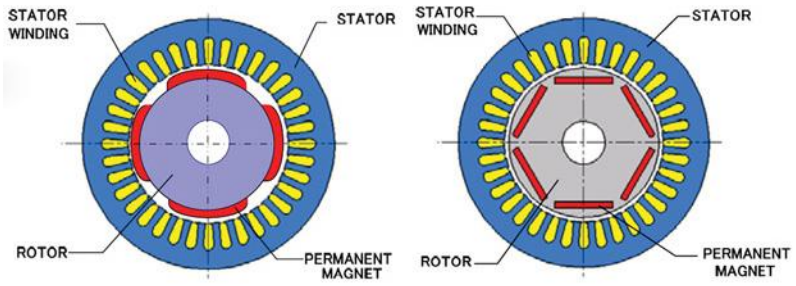

Fig. 1-6 (a) Prototype of a surface-mounted PMSM (b) prototype of an interior PMSM [57]

A new type of motor inserting PMs into the stator is named FSM with the schematic shown in Fig. 1-7. Design and optimization methods of this kind of machine to improve the torque density can be found in [58-60]. However, the problem of cogging torque still exists and the manufacturing is more difficult. Both of them utilize PM material to enhance the excitation, which is rare earth and costly. Moreover, because of the sensitivity of PM material to the variation of temperature, irreversible demagnetization may occur under higher temperature condition and limits its application on high power occasion. Further exploration about alternative materials, such as soft magnetic composites, ferrite magnets, has been exerted in [61-64]. But the performance, like torque density and efficiency, is weakened.

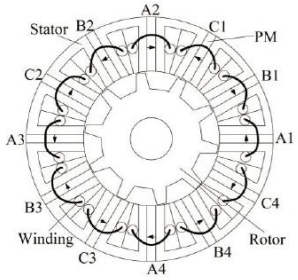

Fig. 1-7 Schematic of an FSM [58]

D. Reluctance Motor

It can be divided into two categories: synchronous reluctance motor (Syn-RM) and switched reluctance motor. Both of them are driven by reluctance torque. The difference is that the torque produced by the synchronous reluctance motor depends on flux barriers in the rotor while that produced by the switched reluctance motor depends on salient pole structure of the rotor. Also the current in the windings of the synchronous reluctance motor is sinusoidal AC while that of the switched reluctance motor is DC.

The topology of a synchronous reluctance motor is shown in Fig. 1-8. Many researchers have considered it as a candidate for EV application. Rotor structure design and magnetic material assisted methods are proposed to reduce torque ripple and improve torque density in [65] and [66], respectively. But mostly this kind of machine only has application in low power occasion.

For the switched reluctance motors, the thesis will discuss more about it in the application of EVs in the following chapters.

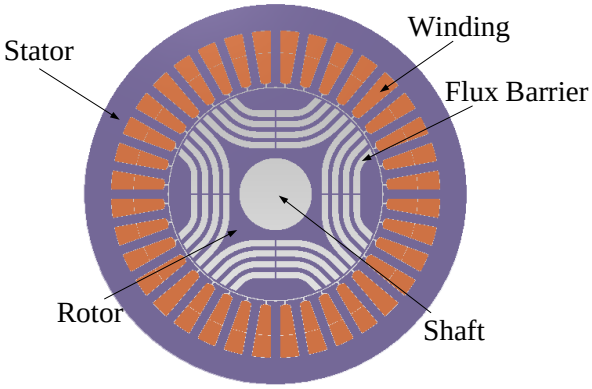

Fig. 1-8 Topology of a synchronous reluctance motor [67]

1.2.2 Switched Reluctance Motors

The switched reluctance motor (SRM) has superior features of simple and robust configuration, low cost, wide speed range and fault tolerance. It has a double salient structure and there are no PMs or windings on or around the rotor. The principle of minimum magnetic reluctance determines the rotation of the motor. The torque production comes from the magnetic saliency between the stator and rotor poles when the concentrated windings around stator poles are under excitation, which indicates higher salient level brings higher torque output. Therefore, there is no need for windings or PMs to be added on the rotor. This enhances the safety factor when it is applied to EVs because there is no induced voltage in the winding even if there is a fluctuation on the rotor [68-69].

Furthermore, the motor demonstrates a higher specific torque (torque per unit of weight) for a wide range of speed than the IM. But because of the elimination of PM materials, its torque density is lower than that of a brushless DC motor. And torque ripple is a major problem causing more noise during motor running. So, a design and optimization of high torque density and low torque ripple SRM topology is preferred for its application to EVs.

To improve the torque density, a great deal of research work has been done in this field. Segmented rotor topology has an improvement in torque output [70-71]. In [70], multi-teeth and single-tooth winding for a segmented rotor SRM offer 40% more torque than its conventional counterparts. Document [71] put forward a segmented rotor SRM combining the ideas of full-pitch winding and multiple phase together to

enhance torque density, which allows two phases to conduct simultaneously and utilizes bipolar excitation.

Similarly, segmented stator topologies can also be proposed to increase output torque [72-75]. In [72], a 6/10 E-core SRM is compared with a 6/3 SRM in [73]. The former can reduce the iron mass and losses greatly. Eskandari [74] takes advantage of the empty space of the 6/10 E-core SRM and form a 9/12 new topology. The torque density increases by 30% at the expense of more copper loss. Paper [75] introduces a 24/22 stator segmented SRM producing 20% more torque output and solving the copper loss problem in [74]. The iron loss, however, goes up as a result of increasing the number of rotor poles.

Many other structures to increase the torque density have also been tried. A double-layer-per-phase SRM with windings between the layers of the stators in each phase is proposed in [76]. It increases the rotor length to produce more torque. The concept of double-stator SRM is put forward in [77-78]. For this topology, more composite of electromagnetic force is in the tangential direction to produce more torque. Axial-type SRM is designed and optimized for high torque density occasion [79-81]. But the airgap of this topology cannot be very small in case of rotor movement distortion.

The converter system is asymmetric half-bridge unlike other AC and brushless DC motors, making each phase of the motor independent and of high fault tolerance, thus, improving the stability. According to the principle of asymmetric half-bridge, some derived converter topologies are proposed and applied to EVs. A winding-tapped topology of SRM is proposed allowing AC and DC charging with different voltage

levels through stator windings [82]. It utilizes the circuits of buck, boost and buck-boost converter tactfully. Also, this kind of topology can achieve battery balancing and fault tolerant control [83-85]. Windings without taps on them can also achieve AC and DC charging via converter circuits [86].

To sum up, a torque density SRM has a vast potential for future development in EVs.

The advantages and disadvantages of different types of motors as mentioned in section 1.2.1 and 1.2.2 can be acquired from Table 1-1.

Table 1-1 Comparison of Different Types of Motors

Motor type	Brushed DC	IM	SRM	Syn-RM	PMSM	FSM
Life span	Short	Long (Squirrel type) Short (Wound type)	Long	Long	Long	Long
Motor start	Normal	Low torque (Squirrel type) Normal (Wound type)	Normal	Normal	Long	Long
Efficiency	Low	Low	High	High	High	High
Structure	Simple	Simple (Squirrel type) Complex (Wound type)	Simple	Complex	Complex	Simple
Torque density	Low	Low	Low	Low	High	High (lower than PMSM)
Speed range	Long	Short	Long	Short	Short	Short
Torque ripple	High	Low	High	Low	Low	Low
Cost	Low	Low	Low	Low	High	High

1.3 Objectives and Structures

1.3.1 Objectives

Although the SRM has many advantages over other types of motors, its torque density is not as high as that of a brushless DC motor, while having a higher torque ripple. The previous research has done some useful contributions in this field, but the torque improvement has been minimum and the cost of manufacturing is very high, along with no improvements in efficiency. Therefore, the primary objective of the thesis is to design and optimize a high torque, low loss motor on the basis of switched reluctance with simple manufacture process for the application to EVs. Moreover, low torque ripple is also considered in the design and control process.

1.3.2 Structures

The structure of the thesis is outlined as follows:

Chapter 1 introduces the background on the dynamic devices for the drive of vehicles and different motors applied to EV drive. In this chapter, the advantages of EVs are put forward. Then various types of motors for EV application are discussed and compared. In the end, the objectives and structure of the thesis are outlined.

An overview of special types of the switched reluctance motor is given in Chapter 2. One type is the switched reluctance motor with more rotor poles than stator poles. The other is the switched reluctance motor with multiple teeth per stator pole. These two types are analyzed and discussed for torque improvement.

In Chapter 3, a novel enhanced torque density in-wheel switched reluctance motor is proposed. The performing principle and design considerations are analyzed in detail. Moreover, the optimization and comparison with conventional SRMs for the novel topology is conducted. The performance is simulated and confirmed by finite element method (FEM).

Another high torque hybrid reluctance motor is introduced in Chapter 4. The working principle and structure analysis is carried out. Multi-variable optimization is made to obtain the highest specific torque for the motor. Finally, the performance of the topology is confirmed by FEM.

A prototype of the hybrid reluctance topology proposed in Chapter 4 is manufactured for experimental verification in Chapter 5. The motor has a smaller size and outer stator structure. Both of the static and dynamic performance are analyzed and compared with FEM results.

The final chapter summarized the major achievements and contributions of the whole thesis. Also, some useful suggestions for future research on motor control and optimization are concluded.

Chapter 2

Overview of Special Switched Reluctance Motors

A high torque density motor is able to reduce the weight of the whole car and save space for supercapacitors or batteries which will allow for longer usage time [87]. To improve the torque performance of SRMs, some structure changes are required.

An SRM with a larger number of rotor poles than that of stator poles can provide more output torque [88]. This is mainly because of the fact that more number of turns of windings are available due to a larger slot area, which also allows for better cooling condition. A design procedure for 6/10 SRM with a new pole design formula is proposed in detail [89]. The concept is suitable for all SRMs regardless of the number of phases: a four phase 8/14 topology using a similar pole design formula is put forward and compared with a traditional 8/6 and 8/10 SRM [90].

Multiple teeth topology is also an effective way to improve torque density and some research has been conducted on the technology. Paper [91] implements finite element analysis (FEA) for the topology and asserts that torque improvement is due to the fast change of inductance which prevents phase current from rising. Iron loss of multiple teeth per stator pole topology by utilizing FEM is calculated [92]. Some design optimization is made for multi-tooth SRM [93].

2.1 SRM With a Higher Number of Rotor Poles

The SRM mentioned in this chapter is its in-wheel version whose structure is an inner stator and an outer rotor. Its outer rotor is integrated straightly with the rim for direct drive. Therefore, it saves space and eliminates transmission loss [94].

Three phase SRMs with various numbers of rotor poles are proposed in this part for performance comparison. The number of the stator poles is chosen as six, and the number of the rotor poles is selected as four, eight and ten, respectively. The prototypes of the three motors are shown in Fig. 2-1 (a), (b) and (c).

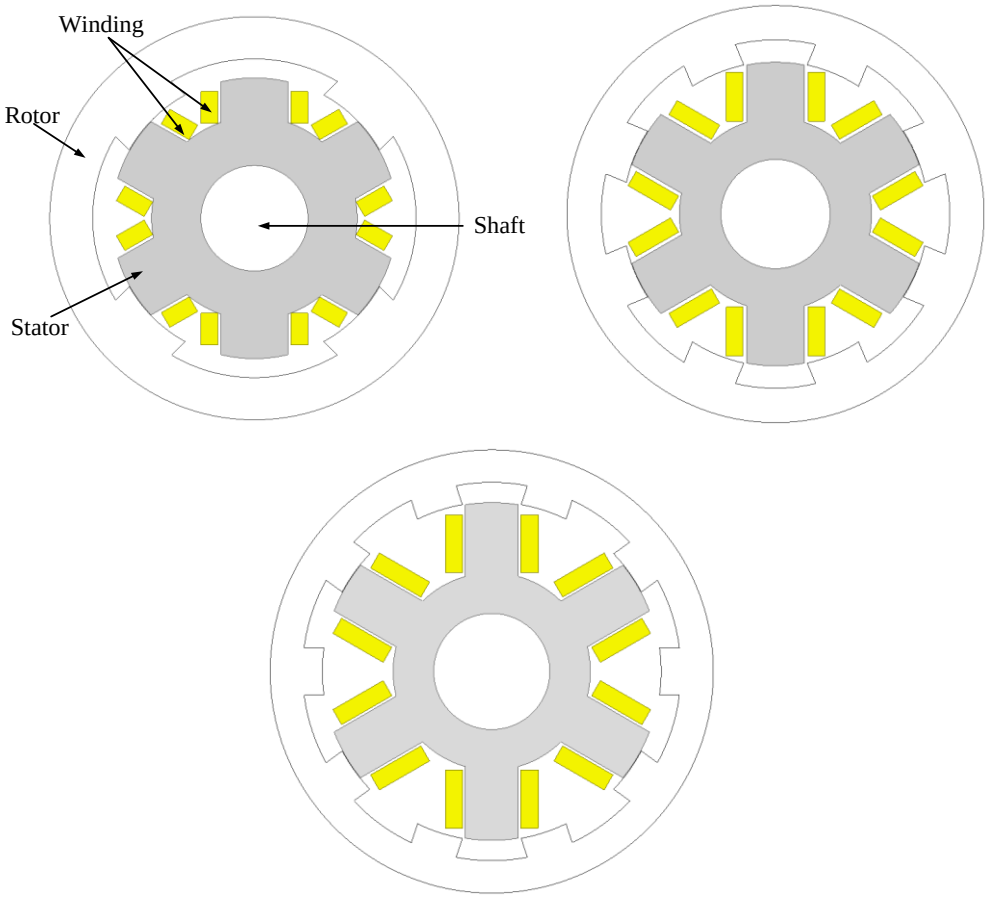

Fig. 2-1 Prototypes of (a) 6/4 (b) 6/8 (c) 6/10 SRM

Due to the fact that as the number of rotor poles increases, the conducting and commutation angles decrease, allowing thinner stator yoke for larger slot area. For high

speed application, however, there are switching frequency limitations of the device IGBT or SCR, which inhibits the motor from acquiring a higher speed and less switching loss. The commutation angle for the three topologies is 30 degrees, 15 degrees and 12 degrees, respectively. The electromagnetic torque comes from the variation of co-energy in the airgap with the angle position of the rotor. The equation of torque calculation can be expressed as:

$$T_e = \frac{\partial W_m}{\partial \theta} \tag{2-1}$$

$$W_m = \int \lambda \cdot di \tag{2-2}$$

where, T_e is the electromagnetic torque of the motor, W_m is the co-energy in the airgap, θ is the angle position of the rotor, λ is the flux linkage and i is the phase current. Also, according to the equation

$$\lambda = L(i,\theta) \cdot i \tag{2-3}$$

where, L is the inductance of each phase of the motor, if mutual inductance is neglected. Provided that the parameter L has no relationship with i, by combining the equations (2-1), (2-2) and (2-3), the electromagnetic torque can be expressed as

$$T_e = \frac{1}{2} \frac{\partial L}{\partial \theta} i^2 \tag{2-4}$$

The three motors are of the same frame, including outer rotor diameter, stack length and airgap according to the design in [95] with the value of 382mm, 74mm and 0.5mm, respectively.

For performance analysis, as a result of the increasing number of rotor poles and

decreased commutation angle, the iron loss for the latter two topologies is higher than the conventional one. For thermal consideration, all the three motors are running at the same speed and losses (iron loss plus copper loss) for their full expected load and the maximum current density of the three motors is limited to $3A/mm^2$. The flux linkage of the three motors at aligned and unaligned position with the variation of the current is shown in Fig. 2-2 and the inductance characteristic at different positions of can be obtained from Fig. 2-3.

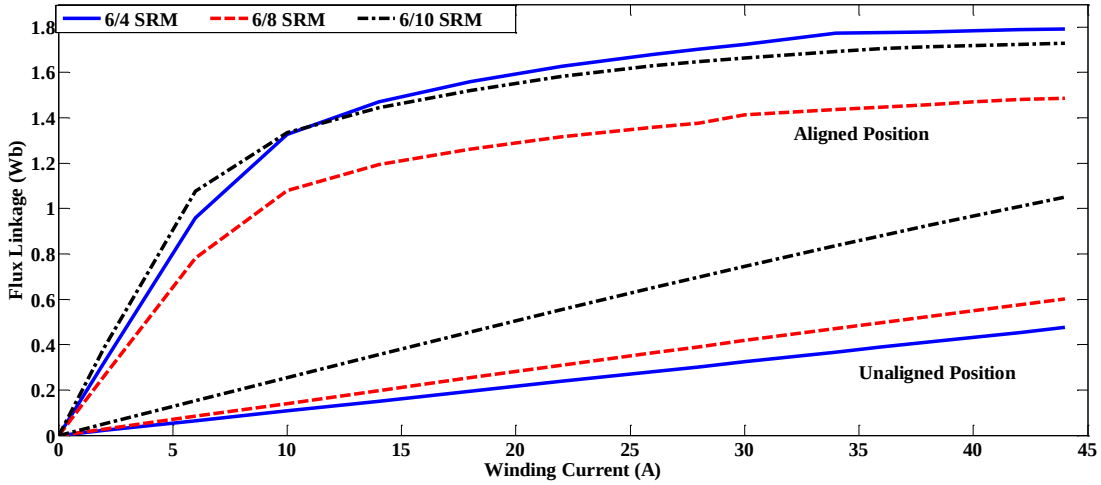

Fig. 2-2 Flux linkage characteristic of 6/4, 6/8 & 6/10 SRM

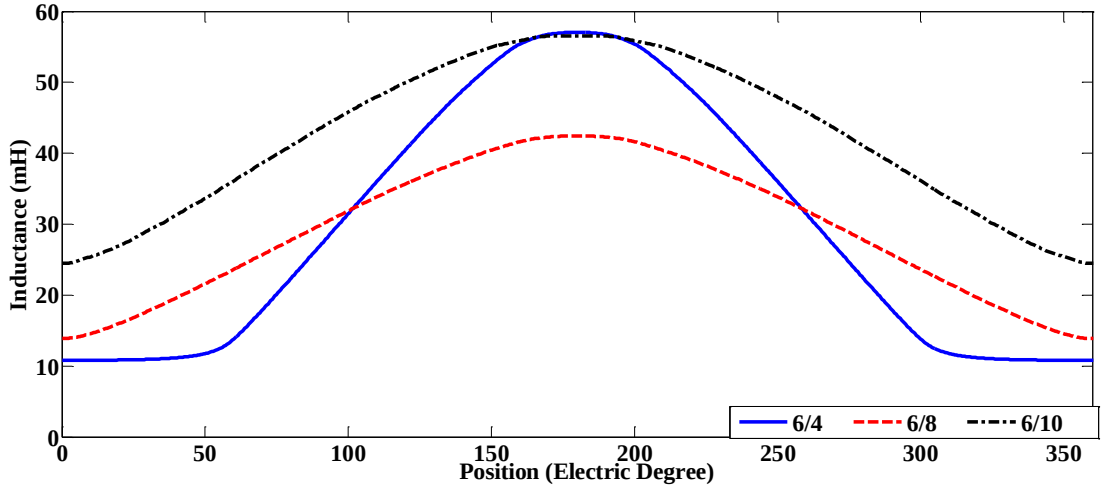

Fig. 2-3 Inductance profile for a full electric period

Although the difference between the flux linkage at aligned and unaligned position

for 6/8 and 6/10 SRM is smaller than that of their traditional 6/4 counterpart, the conducting and commutation angle is smaller as well, indicating more times of stroke during the same mechanical period. The number of stroke times for 6/8 and 6/10 SRM is twice and 2.5 times, respectively, as many as that of the conventional 6/4 SRM. Therefore, the torque characteristic is not weakened. The torque waveform for one phase and full phase conducting of the three topologies by using 2D-FEM is shown in Fig. 2-4 and Fig. 2-5, respectively.

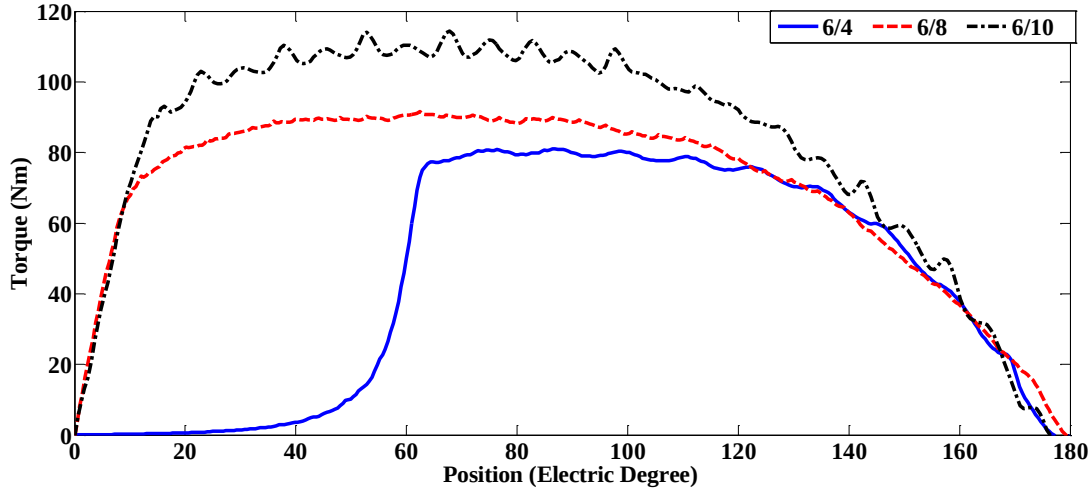

Fig. 2-4 Phase torque waveform of 6/4, 6/8 & 6/10 SRM

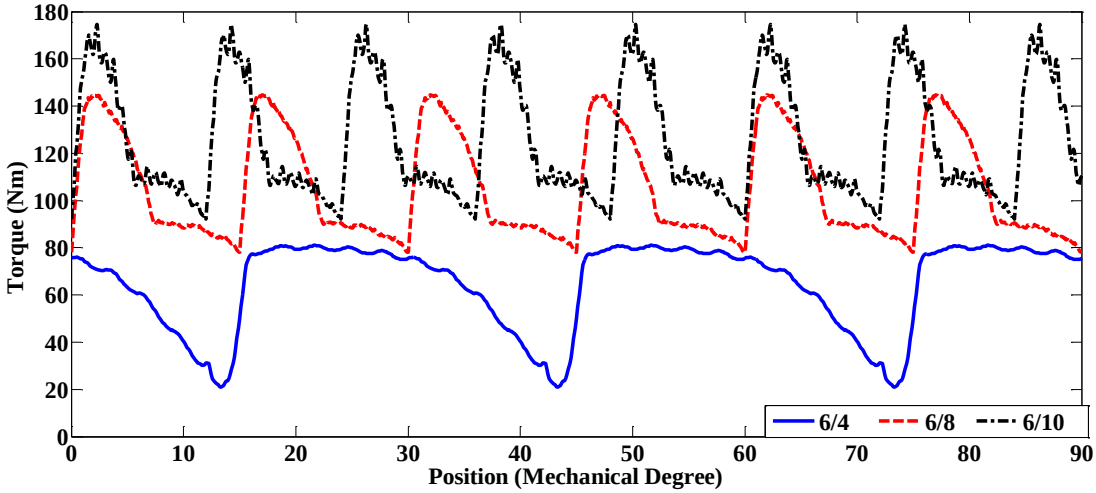

Fig. 2-5 Full torque waveform of 6/4, 6/8 & 6/10 SRM

From the curves in Fig. 2-4 and Fig. 2-5, the torque performance improvement for

SRMs with more rotor poles than stator poles is obvious. But it is at the expense of using a larger amount of copper as shown in Table 2-1, including the cost and torque performance.

Table 2-1 Winding Parameter of the Three Motors

dimensions	6/4 SRM	6/8 SRM	6/10 SRM
Turn number each phase	182	184	248
Wire type	17AWG six parallel	17AWG eight parallel	17AWG eight parallel
Copper weight (kg)	11.4	13.2	17.4
Copper price (USD/kg) [96]	6.83	6.83	6.83
Silicon Steel used for manufacturing (kg)	62.8	62.8	62.8
Silicon Steel price (USD/kg)	0.5	0.5	0.5
Coil end length (mm)	16.0	17.5	19.7
Average Torque (Nm)	64.7	105.5	123.6
Torque ripple (%)	92.7	63.5	66.3

AWG: American Wire Gauge Copper price from Oct. 6 2017

Table 2-1 indicates that about 20% and 50% more copper windings are required for 6/8 and 6/10 SRM for higher torque output, which cost 11.3% and 37.5% more, respectively, and increases the volume of the motor because of longer coil end length.

2.2 SRM with Multiple Teeth per Stator Pole

The structure for analysis is also an inner stator and outer rotor topology. The proposed prototype is 6/10 three phase SRM with two teeth per stator pole as shown in Fig. 2-6 (a) and a 6/4 SRM in Fig. 2-6 (b) with the same dimensions (rotor outer diameter 382mm, airgap length 0.5mm, stack length 74mm).

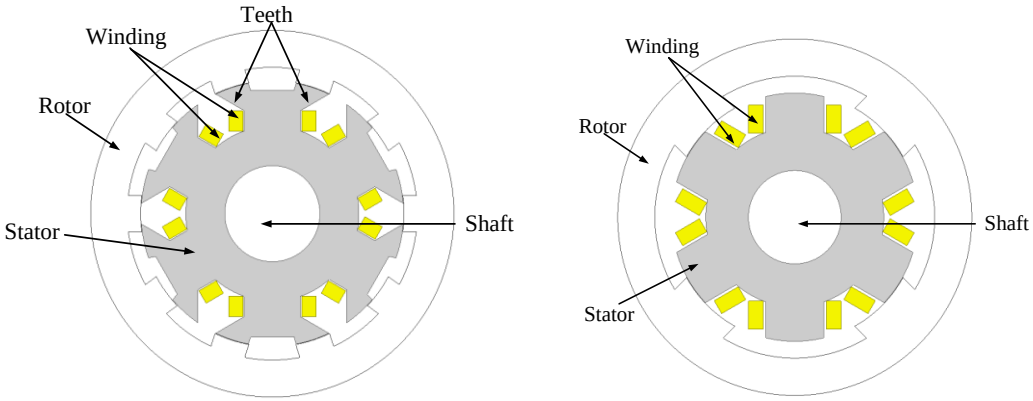

Fig. 2-6 Profile of (a) 6/10 two-teeth SRM (b) 6/4 SRM

The two teeth topology leads to the increased number of rotor poles and the commutation angle declined to 12 degrees compared with conventional 6/4 SRM whose commutation angle is 30 degrees, but it is still accessible for normal operations of the motor. The flux linkage characteristic and self-inductance feature of the two topologies are shown in Fig. 2-7 and Fig. 2-8, respectively.

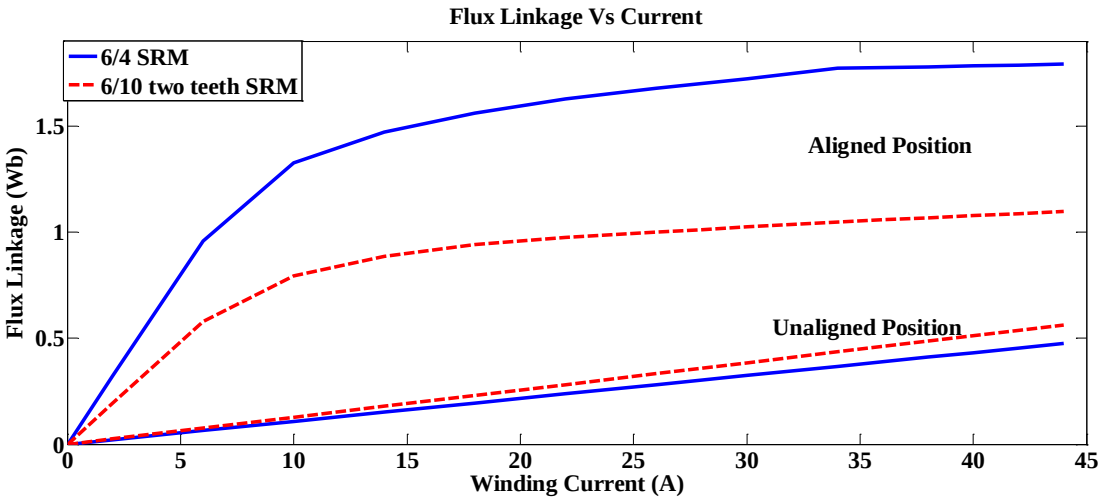

Fig. 2-7 Flux characteristic of 6/4 SRM & 6/10 two teeth SRM

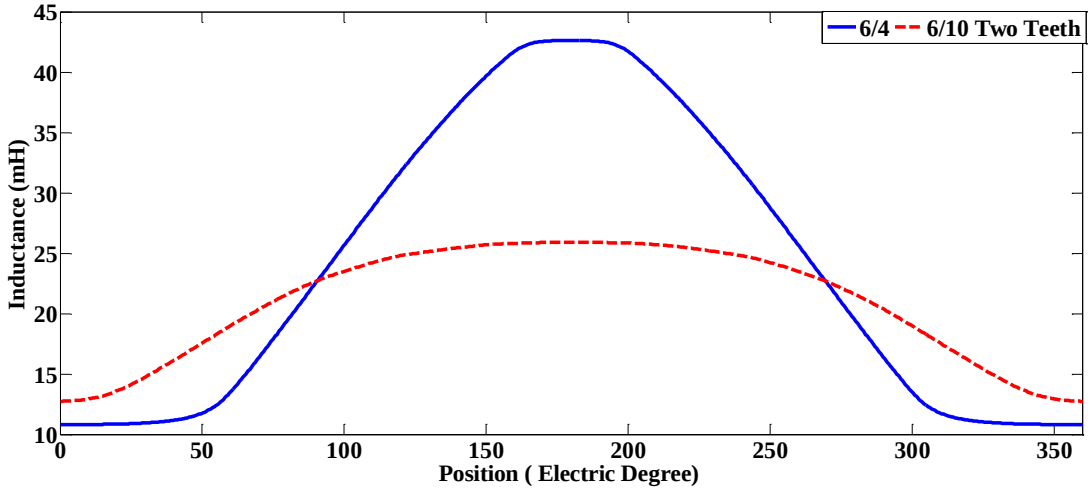

Fig. 2-8 Inductance characteristic of 6/4 SRM & 6/10 two teeth SRM

The above two figures demonstrate that the variation of flux linkage from unaligned to aligned position with different current values is more significant for 6/4 SRM than 6/10 two teeth SRM. Moreover, this leads to the slower speed of inductance variation from the unaligned to aligned electric position for 6/10 two teeth SRM. However, its stroke times per round is 2.5 times as many as that of 6/4 SRM, along with two teeth together to distribute magnetic flux. Therefore, the torque performance is not weakened.

The torque performance of the two motors under one phase and full phase conducting is analyzed in Fig. 2-9 and Fig. 2-10, respectively. For air cooling condition, the current density of both motors is set as 5A/mm^2. The torque performance comparison of the two topologies can be found in Table 2-2.

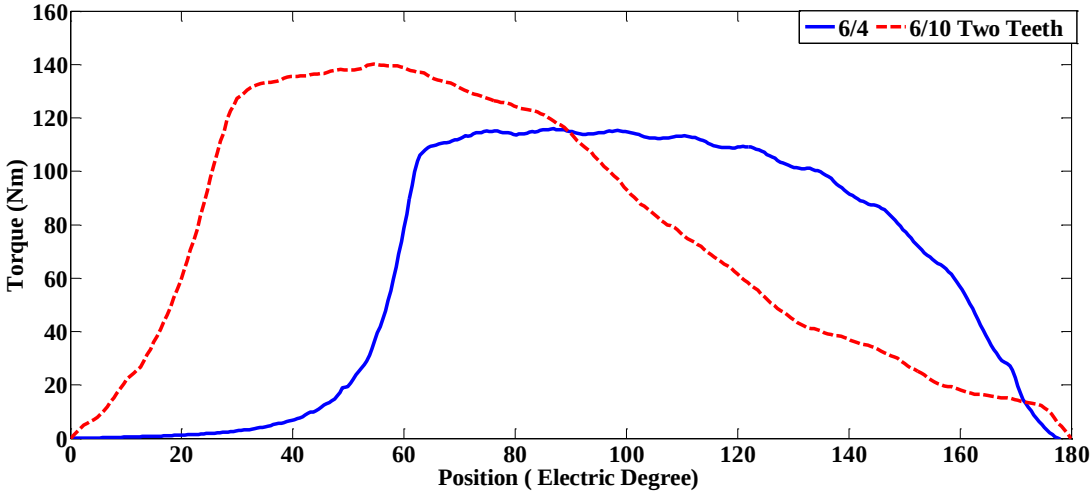

Fig. 2-9. Torque waveform of half an electric period single phase conducting for the two motors

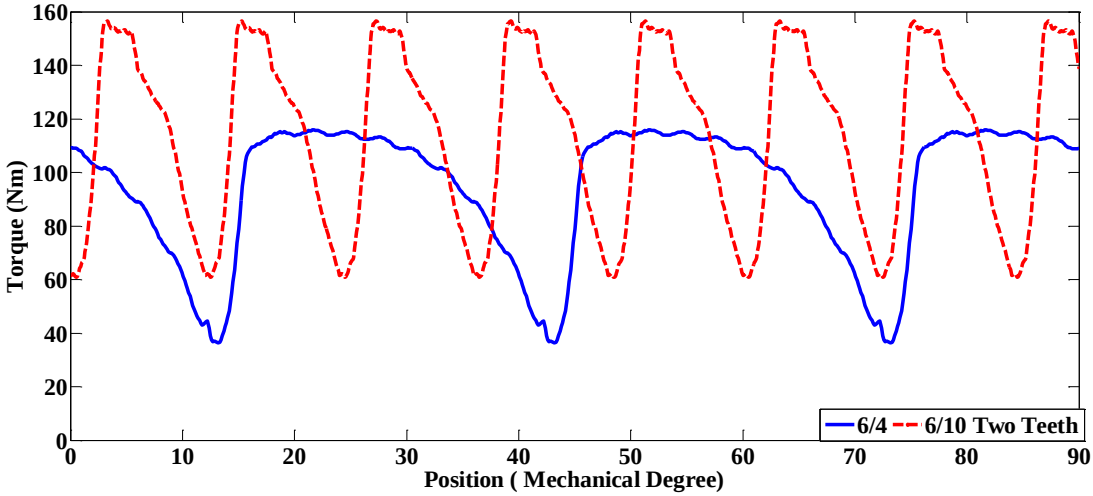

Fig. 2-10 Torque waveform of full phase conducting for the two motors

Table 2-2 Torque Performance Comparison of the Two Topologies

Parameter	6/4 SRM	6/10 two teeth SRM
Current density (A/mm^2)	5	5
Torque (Nm)	94.3	113.6
Torque ripple (%)	84.3	84.6

Fig. 2-9 shows that at the beginning from the unaligned position, 6/10 two teeth SRM has a faster respond to increase output torque and the peak value is higher than that of a conventional 6/4 SRM. But when the overlapping angle of stator teeth and rotor poles continues increasing, the magnetic saturation becomes quite significant due to the magnetic flux passing through two teeth and two rotor poles simultaneously as shown in Fig. 2-11 (a). This results in high magnetic reluctance in the stator pole, thus declining the output torque.

Fig. 2-11 (b) illustrates the flux density of 6/10 two teeth topology. The wide range of flat inductance characteristic also indicates the high saturation effect of 6/10 two teeth structure. Full phase conducting means that an ideal square current waveform is injected into each phase for half an electric period conducting from the unaligned position to aligned position. Table 2-2 demonstrates that there is torque improvement for two teeth SRM; the torque ripple, however, is not reduced.

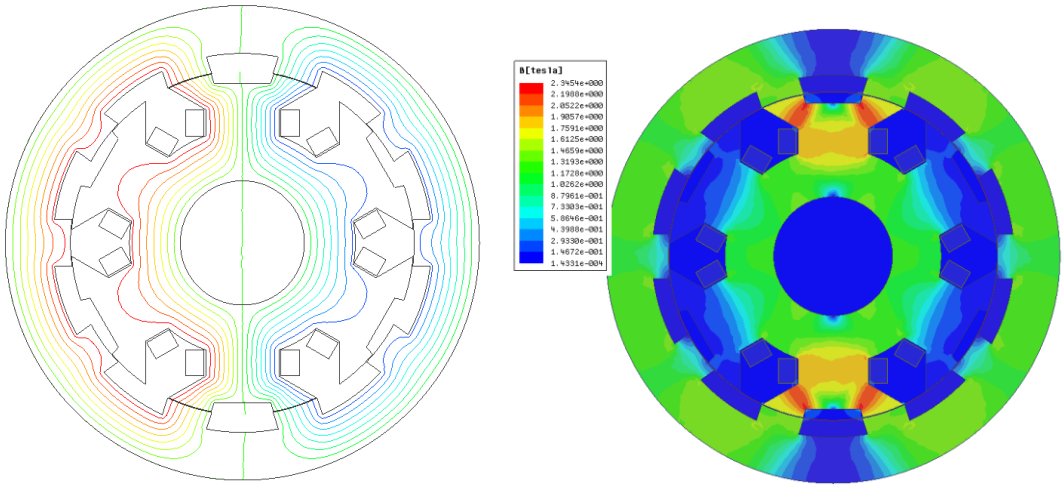

Fig. 2-11 Magnetic features of 6/10 two-teeth SRM (a) flux distribution (b) flux density

2.3 Summary

In this chapter, two kinds of special SRMs are proposed to enhance the torque characteristics of the motor. SRMs with a higher number of rotor poles than stator poles have more space for windings by reducing the commutation angle and increasing the commutation frequency. The torque performance is improved by increasing the number of turns per phase or cross sectional area of the conductor at the same current density. On the other hand, SRMs with two teeth per stator pole allows magnetic flux to pass through two teeth and two rotor poles at the same time to enhance the output torque. This topology can improve the average torque with high torque ripple because of high magnetic saturation.

Chapter 3

Design of a Novel Enhanced Torque In-Wheel Switched Reluctance Motor

Improving the torque density of the motor for the application of EVs is a popular topic now. The methods can be divided into two categories: 1) inserting the PM material into the motor and 2) changing the structure of the motor. This chapter focuses on the latter one. The proposed topology incorporates the ideas of multi-teeth per stator pole and more rotor poles than stator teeth together. The torque output can be improved at the same energy loss compared with other types of SRM and the specific torque is also enhanced.

3.1 Introduction

For the purpose of enhancing the torque performance of the SRM, numerous researchers have carried out large quantities of experiments in this field. Segmented stator or rotor structure is an effective way to improve the torque density for SRMs as mentioned before [70-75].

The ideas of more rotor poles than stator poles and segmented rotor topology are combined together for torque improvement [97-99]. J. Widmer [97] proposes a 12-16 rotor segmented SRM with full pitch winding which can produce 65% more torque per unit copper loss than its conventional counterparts. Papers [98-99] provide the design procedure of a 12/26 rotor segmented SRM with concentrate windings on alternate stator poles to improve torque performance.

Other scholars are thinking about improving the torque density by designing a complicated structure as illustrated in Chapter 1 [76-81].

However, the above design methods are at the expenses of increasing the difficulty of manufacturing and reducing the simple and robust structure of the SRM, in order to achieve torque improvement. In addition, the cost of production also rises.

In this chapter, a novel topology is proposed to enhance the torque output by utilizing multi-teeth per stator pole and more rotor poles than stator teeth together. The structure is an in-wheel version for the purpose of its application to the EVs. Although the multi-teeth structure can increase the torque output, high magnetic saturation appears in the stator pole due to the doubled overlapping arc angles between the stator teeth and rotor poles. This not only weakens the average torque, but also

causes large torque ripple. Moreover, the thick stator pole occupies the space for windings and increases the difficulty for control. The topology with a higher number of rotor poles improves the torque density at the expense of utilizing larger amount of copper which is costly and increases the overall weight. Therefore, a new topology is put forward considering combining these two together. The manufacture process of the proposed topology is not difficult and the windings are suitable for automatic coil winding. Therefore, it has a great potential for quantity production.

3.2 Design & Analysis of the Novel Topology

This part is divided into two categories: magnetic principle and design considerations.

3.2.1 Magnetic Principle of the Topology

The input electrical energy W_e can be calculated in the following equation (3-1),

$$W_e = \int ei \bullet dt = \int i \frac{d\lambda}{dt} \bullet dt = \int id\lambda \tag{3-1}$$

where, e is the input voltage, i is the phase current, λ is the flux linkage each phase. It has two components: energy stored in the windings and the energy that is converted to mechanical energy as shown in the following equation (3-2),

$$W_e = W_f + W_m \tag{3-2}$$

where, W_f is the energy storage in the windings and W_m is the mechanical energy converted. When the rotor rotates from position x_1 to x_2, the above two parameters can

be shown in Fig. 3-1 for better illustration.

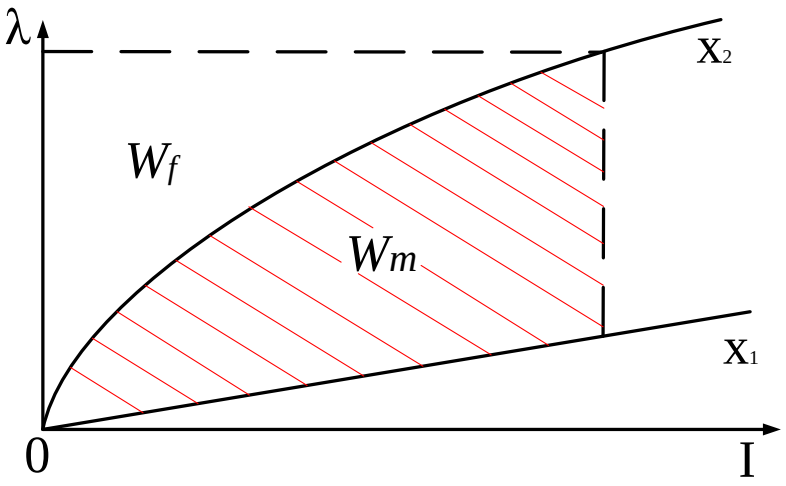

Fig. 3-1 Flux linkage feature VS current for the SRM

The equations for W_f and W_m are shown as follows:

$$\Delta W_f = \int_0^{\lambda} i(x_2)d\lambda - \int_0^{\lambda} i(x_1)d\lambda \tag{3-3}$$

$$W_m = \int_0^{i} [\lambda(x_2) - \lambda(x_1)]di \tag{3-4}$$

As a result, the transient torque of the SRM can be expressed as,

$$T_e = \frac{\partial W_m}{\partial \theta} \tag{3-5}$$

where, W_m is the mechanical energy which is converted to from electrical energy, called co-energy of the field and θ is the position of the rotor. For traditional SRMs, there is only one tooth per stator pole to allow magnetic flux to pass through while the proposed motor has multi-teeth per stator pole to distribute the flux. Multiple groups of teeth together make the flux variation larger for the same rotary angle and the variation period shorter. A flux distribution comparison between one tooth and multiple teeth

topology (two teeth for example) is shown in Fig. 3-2 (a) and (b), respectively.

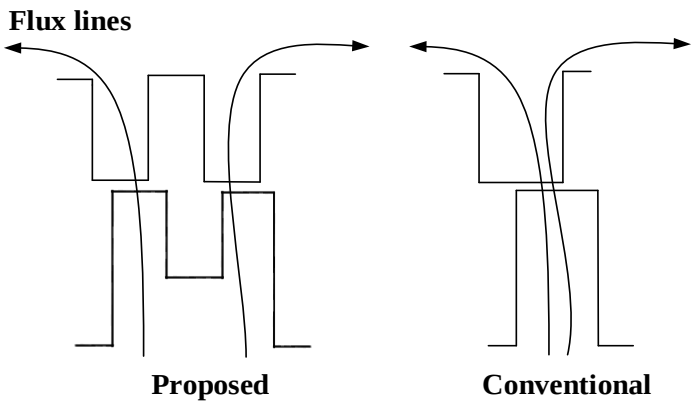

Fig. 3-2 Flux distribution of the (a) multi-teeth topology (b) conventional topology

The unaligned position of the rotor $\theta_{unalign}$ is set as zero position, therefore the transient rotor position can be expressed as,

$$\theta = \frac{l_{arc}}{r} + \frac{\pi}{N_r} - \frac{\theta_s}{2} - \frac{\theta_r}{2} \tag{3-6}$$

where, θ_s and θ_r is the arc angle of stator tooth and rotor pole, respectively; N_r is the number of rotor poles, l_{arc} is the overlapping length between one stator tooth and a rotor pole and r is the outer radius of the stator. The co-energy W_m can be calculated as,

$$\partial W_m = \int_0^I [\lambda(\theta + \Delta\theta) - \lambda(\theta)] di \tag{3-7}$$

$$\lambda = N\Phi \tag{3-8}$$

where N is the number of turns per phase, Φ is the magnetic flux of each phase. So, equation (3-7) can be expressed to

$$\partial W_m = \int_0^I N[\Phi(\theta + \Delta\theta) - \Phi(\theta)] di \,. \tag{3-9}$$

$$\Phi = \frac{NI}{R_s + R_r + 2R_g} \tag{3-10}$$

where I is the phase current; R_g, R_s, R_r is the magnetic reluctance of airgap, stator and rotor, respectively. Because of $R_g >> R_s + R_r$,

$$\Phi \approx \frac{NI}{2R_g} \tag{3-11}$$

Due to

$$R_g(\theta + \Delta\theta) = \frac{l_g}{\mu_0 m[l_{arc}(\theta + \Delta\theta)] \cdot l} \tag{3-12}$$

$$R_g(\theta) = \frac{l_g}{\mu_0 m[l_{arc}(\theta)] \cdot l} \tag{3-13}$$

The co-energy is computed as

$$\partial W_m = \int_0^I \frac{N^2 I \mu_0 m[l_{arc}(\theta + \Delta\theta) - l_{arc}(\theta)] \cdot l}{2l_g} di \tag{3-14}$$

By inserting (3-6) and (3-14) into equation (3-5) where the only variable is l_{arc}, the electromagnetic torque result is

$$T_e = \int \frac{N^2 I \mu_0 m l r}{2l_g} di \tag{3-15}$$

where, m is the number of teeth per stator pole, l_g and l is the length of airgap and the steel stack, respectively. From equation (3-15), with m increasing, the value of output torque rises. However, this may not be true because larger number of teeth per stator pole can cause smaller area for windings, thus decreasing the value of N. Moreover, the number of rotor poles grows with the increasing number of stator teeth, which leads to a smaller commutation angle, more leakage flux and higher core loss. In addition, the slot area for windings is reduced because of the growing number of stator teeth.

The flux distributions of three teeth and four teeth per stator pole are shown in Fig. 3-3 (a) and (b), respectively. And the equivalent magnetic circuit model of the topology can be found in Fig. 3-4, where F represents the magnetic motive force (MMF) produced by the excitation current; R_{sp}, R_{st}, R_{sy} is the magnetic reluctance of the stator pole, tooth and yoke, respectively; R_{rp}, R_{ry} is that of rotor pole and yoke, respectively; R_g is the airgap magnetic reluctance between a single stator tooth and its corresponding rotor pole and m is the number of teeth per stator pole.

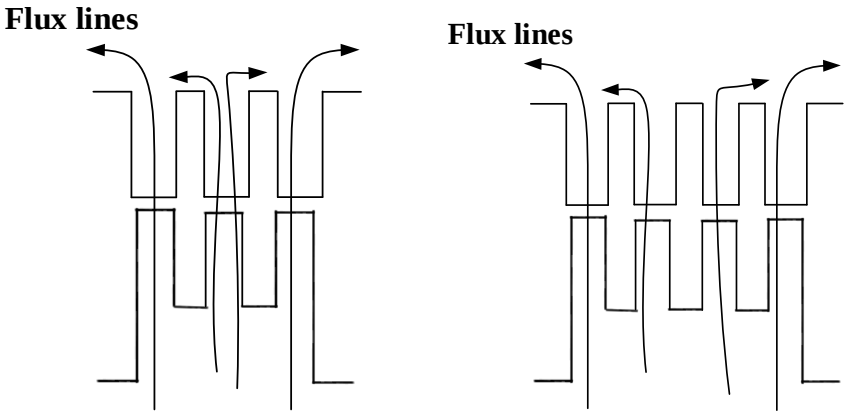

(a) (b)

Fig. 3-3 Flux distribution of (a) three teeth topology (b) four teeth topology

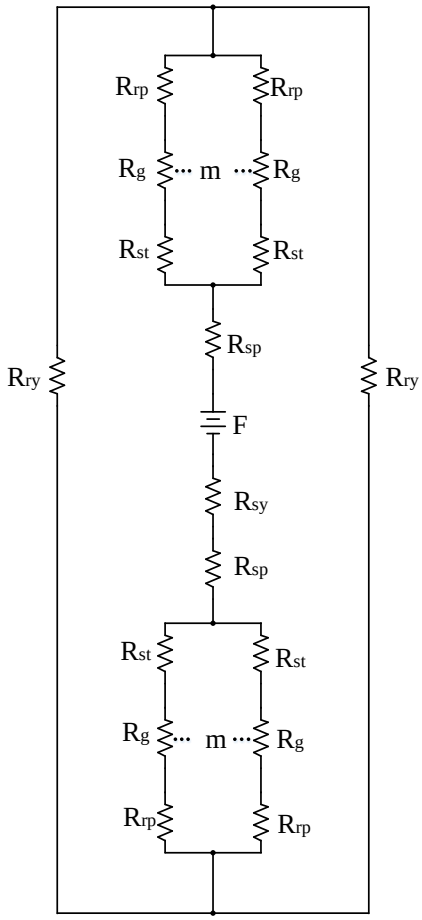

Fig. 3-4 Equivalent magnetic circuit model of the multi-teeth topology

To ensure the optimized teeth number per stator pole, three phase six stator pole motors with various number of teeth are chosen for comparison. Some parameters are the same as those mentioned in [95], with the rotor outer diameter 382 mm, airgap length 0.5 mm and stack length 74 mm. Also, the wire type and parallel number are identical. Furthermore, 20 Ampere excitation current is injected into the windings. Through 2D-FEM, the average torque output and core loss for different number of teeth can be obtained from Fig. 3-5 (a) and (b), respectively.

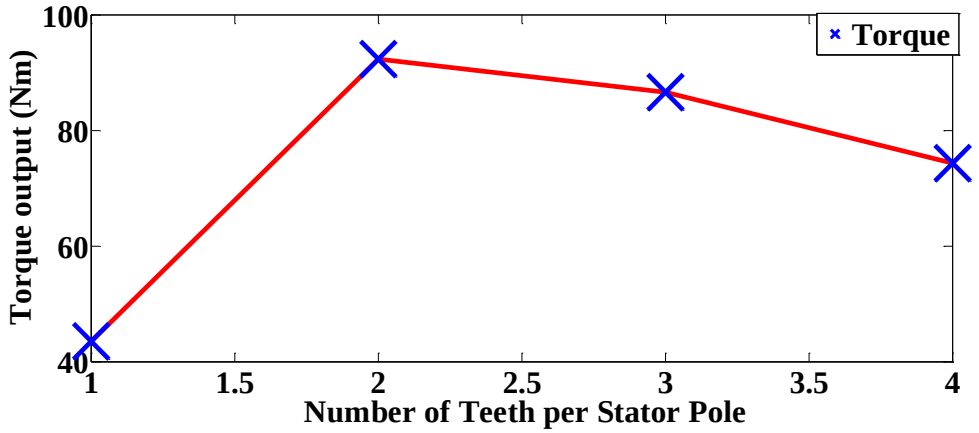

(a)

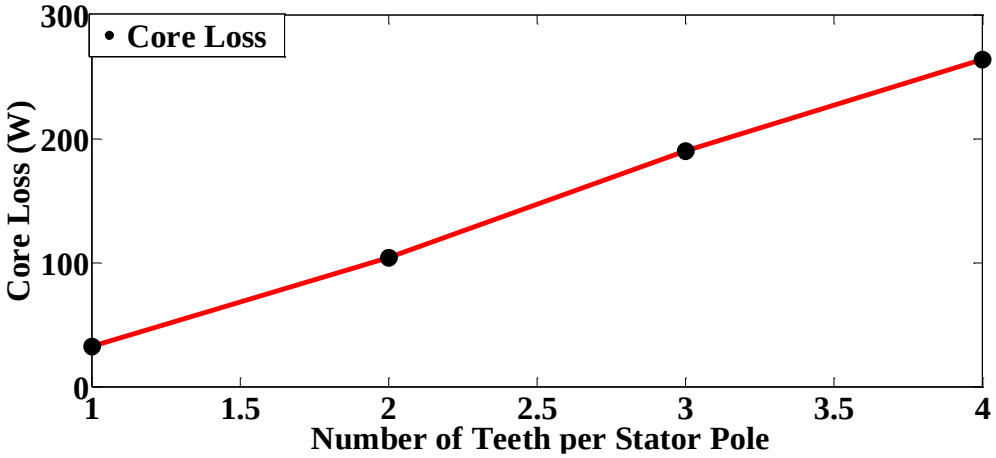

(b)

Fig. 3-5 SRMs with different teeth per stator pole (a) torque output (b) core loss

The above two figures demonstrate that the two teeth topology has the maximum energy conversion capacity. Besides, three teeth topology has at least 20 rotor poles and that of four teeth at least 26, which can result in quite small commutation angle, limited slot area for windings, high core loss and low efficiency.

3.2.2 Design Considerations for the topology

A. Selection of Number of Phase

Although large number of phases are effective in reducing torque ripple and noises,

the winding area is declining as well. Therefore, it cannot improve average torque. Moreover, for the principle of the proposed topology, increasing the number of phases will lead to higher number of rotor poles which is not suitable for high speed application. With regard to the above problems, the number of phases is selected as three.

B. Selection of Number of Rotor Poles

According to the working principle of the SRM (three phase with six stator pole), some requirements of stator and rotor arc angles and the number of the rotor poles should be taken into consideration. In Fig. 3-6, the magnetic flux distribution agrees quite well with the theoretical analysis, in which the magnetic flux passes through two teeth and goes into two individual rotor poles. Moreover, each of the stator and rotor teeth is parallel.

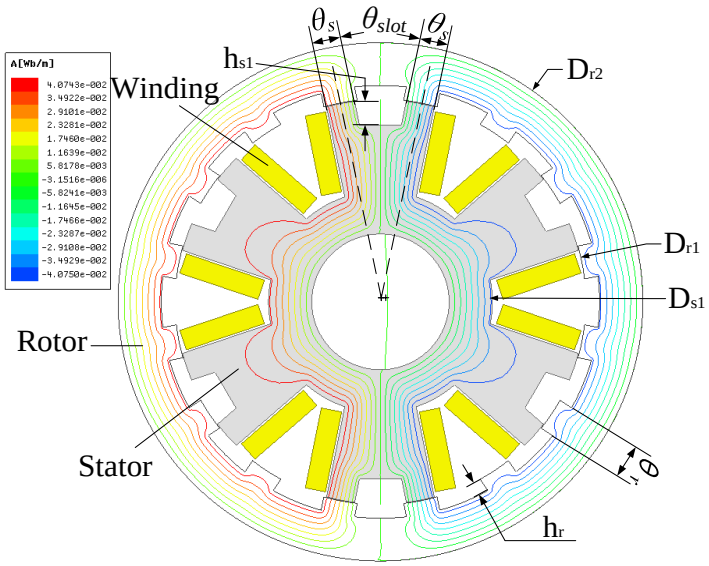

Fig. 3-6 Flux distribution & prototype of the proposed topology

The angle and rotor pole design requirements can be expressed as follows:

$$\begin{cases} \dfrac{\theta_s}{2} + \theta_{slot} + \dfrac{\theta_s}{2} = \dfrac{360^\circ}{N_r} \\ 60^\circ + \dfrac{120^\circ}{N_r} = k \cdot \dfrac{360^\circ}{N_r} \end{cases} \tag{3-16}$$

where, θ_{slot} is the arc angle of the stator inner slot and k is an integer ($k \geq 2$). The first equation of (3-16) can be understood from the arc angle between two black dash lines in the proposed prototype in Fig. 3-6; the second formula, in which $60°$ stands for the stator pole pitch arc angle and $120°/N_r$ represents the commutation angle, can be illustrated on the basis of the operating principle of the SRM due to the fact that the current conducting and commutation mode are the same as conventional three phase SRMs. After simplification, the result can be obtained as

$$\begin{cases} \theta_{slot} + \theta_s = \dfrac{360^\circ}{6k-2} \\ N_r = 6k-2 \end{cases} \tag{3-17}$$

To keep the number of rotor poles more than that of stator teeth, the value of k should be more than 2. Also, to maintain a suitable commutation angle, k is set as 3. Hence, $\theta_{slot}+\theta_s=22.5°$, N_r=16 and the commutation angle is 7.5 degree. Therefore, the basic parameters of the motor are defined.

C. Selection of the Airgap Length & Shaft Diameter

The length of airgap is quite important for the torque performance of the motor. It should be designed as small as possible to enhance the motor characteristics. But too small length of airgap not only increases the difficulty for manufacture, but requires much higher mechanical strength as well. At the time the rotor rotates, it is driven by both tangential and radial forces. The tangential force is utilized to produce torque, but radial force introduces audible noise and vibration. If the airgap is too small, the

vibration of the rotor and tiny deform of the shaft may lead to a contact between the stator and rotor, thus resulting in a motor fault.

On the basis of the size of the in-wheel motor, the airgap length is selected as 0.5 mm and shaft diameter 100 mm, the same as those in [95].

3.3 Optimization of the Topology

The optimization of the two teeth topology is conducted on the basis of genetic algorithm (GA) and equivalent magnetic circuit (EMC) model. The EMC model is utilized to calculate the self-inductance of the topology on the basis of the method mentioned in [100]. An analogical approach of obtaining various magnetic flux lines can be carried out to analyze the proposed topology.

3.3.1 Electromagnetic Torque Generation

The general voltage equation for the motor is expressed as

$$V = IR + \frac{d\lambda}{dt} \tag{3-18}$$

where, R is the resistance of the winding and V is the DC bus voltage. Neglecting the mutual inductance, the equation is expanded to be:

$$\begin{aligned} V &= IR + \frac{d(LI)}{dt} \\ &= IR + L\frac{dI}{dt} + I\frac{dL}{dt} \end{aligned} \tag{3-19}$$

where L is the self-inductance of each phase of the motor. Ignoring the relationship between the self-inductance and current since the hysteresis control keeps the current with little fluctuation, almost as a constant, the equation can be written as

$$V = IR + L\frac{di}{dt} + I\omega\frac{dL}{d\theta} \tag{3-20}$$

Therefore, with either side multiplied by current *I*, it follows that

$$P = I^2R + LI\frac{di}{dt} + I^2\omega\frac{dL}{d\theta} \tag{3-21}$$

$$\begin{aligned} LI\frac{di}{dt} &= \frac{d(\frac{1}{2}LI^2)}{dt} - \frac{1}{2}I^2\frac{dL}{dt} \\ &= \frac{d(\frac{1}{2}LI^2)}{dt} - \frac{1}{2}I^2\omega\frac{dL}{d\theta} \end{aligned} \tag{3-22}$$

So, by inserting (3-22) into (3-21), the power equation is converted to

$$P = I^2R + \frac{d(\frac{1}{2}LI^2)}{dt} + \frac{1}{2}I^2\omega\frac{dL}{d\theta} \tag{3-23}$$

The first part on the right of the equal sign is the copper loss; the second part is the energy storage per time unit and the third part is the mechanical output power. Due to the equation below,

$$P_e = T_e \cdot \omega \tag{3-24}$$

The torque equation is

$$T_e = \frac{1}{2}\frac{dL}{d\theta}I^2 \tag{3-25}$$

From equation (25), the electromagnetic torque depends mainly on the difference between the maximum and minimum self-inductance and excitation current injected into the windings.

3.3.2 Calculation of the Self-inductance

The calculation of inductance is based on

$$L = \frac{\lambda}{I} = \frac{N\Phi}{I} \tag{3-26}$$

The simplified EMC model is shown in the following Fig. 3-7.

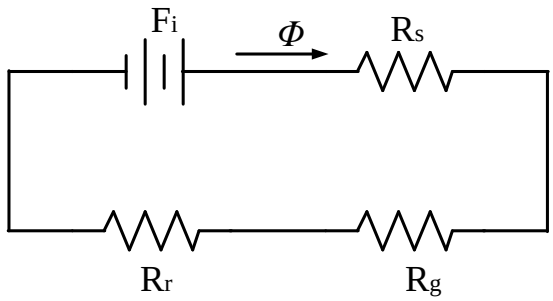

Fig. 3-7 Simplified EMC model of the topology

According the equation (3-27) and (3-28) below,

$$\Phi = \frac{F}{R_g + R_s + R_r} \tag{3-27}$$

$$F = NI \tag{3-28}$$

The value of inductance can be obtained.

The procedure of acquiring the value of inductance is as follows: initially, an estimated value of the flux density B_{sp} is given, then, the magnetic flux Φ is obtained. Later on, the magnetic flux density in the stator yoke B_{sy}, airgap B_g, rotor pole B_{rp} and rotor yoke B_{ry} can be calculated. It follows that the value of the magnetic field intensity H is known according to B-H curve of the steel material, which is DR-510 for the proposed motor. Moreover, the MMF can be calculated by the summation of $H \cdot l$ and $N \cdot I$, respectively. Eventually, if the error of the above two calculation results is less than the limit, the calculation ends; otherwise, the flux density B_{sp} will change a little (either plus or minus), and a new circulation begins. The flowchart of the calculation method is shown in Fig. 3-8.

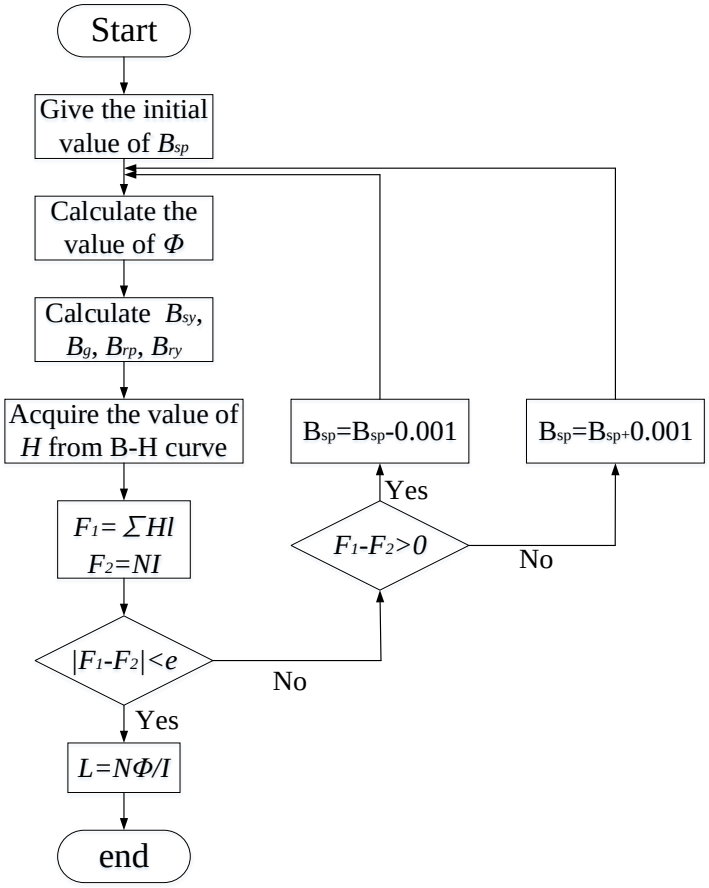

Fig. 3-8 Flowchart of the inductance calculation process

Some common equations required for self-inductance calculation should be introduced first.

$$R_g = \frac{l_g \cdot H_g}{A_g \cdot B_g} \tag{3-29}$$

$$R_{sp} = \frac{l_{sp} \cdot H_{sp}}{A_{sp} \cdot B_{sp}} \tag{3-30}$$

$$R_{sy} = \frac{l_{sy} \cdot H_{sy}}{A_{sy} \cdot B_{sy}} \tag{3-31}$$

$$R_{rp} = \frac{l_{rp} \cdot H_{rp}}{A_{rp} \cdot B_{rp}} \tag{3-32}$$

$$R_{ry} = \frac{l_{ry} \cdot H_{ry}}{A_{ry} \cdot B_{ry}} \tag{3-33}$$

where, l_g, l_{sp}, l_{sy}, l_{rp} and l_{ry} is the average length of airgap, stator pole, stator yoke, rotor

pole and rotor yoke, respectively; A_g, A_{sp}, A_{sy}, A_{rp} and A_{ry} is the average cross area of airgap, stator pole, stator yoke, rotor pole and rotor yoke, respectively. Then the inductance calculation of unaligned and aligned position is analyzed in the following part.

3.3.2.1 Unaligned Position

The minimum self-inductance can be obtained from the fully unaligned position. The flux paths distribution is shown in Fig. 3-9 (a) and (b). The schematic is an axis symmetric figure, therefore, the flux paths are bilaterally symmetric. h_s and h_r is set as the height of the stator inner slot and the rotor, respectively. The width of the rotor and stator pole is marked as l_r and l_p, respectively. Therefore, the starting and end point positions of different flux paths through the airgap are shown as follows: $r_1=(3/8)l_r$, $r_2=(1/4)l_r$, $r_3=(5/64)l_r$, $r_4=(1/4)h_{s1}$, $r_5=(5/8)h_{s1}$, $r_6=(5/6)h_r$, $r_7=(5/32)h_r$, $r_8=(3/8)h_{s1}$, $r_9=(3/32)l_r$, $r_{10}=(5/8)l_p$, $r_{11}=(7/8)l_p$, $r_{12}=(5/8)h_s$, $r_{13}=(1/4)h_s$.

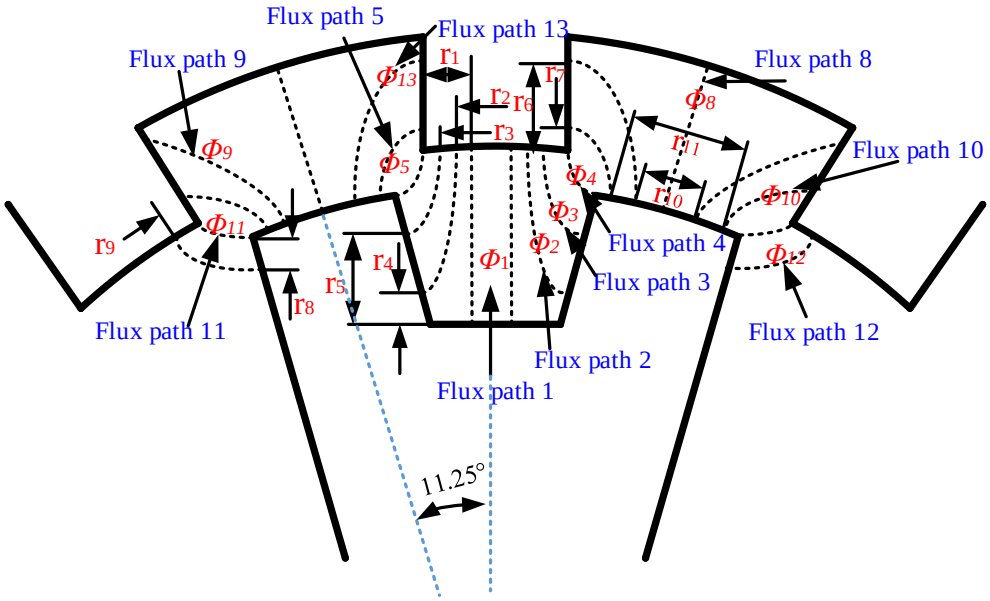

(a)

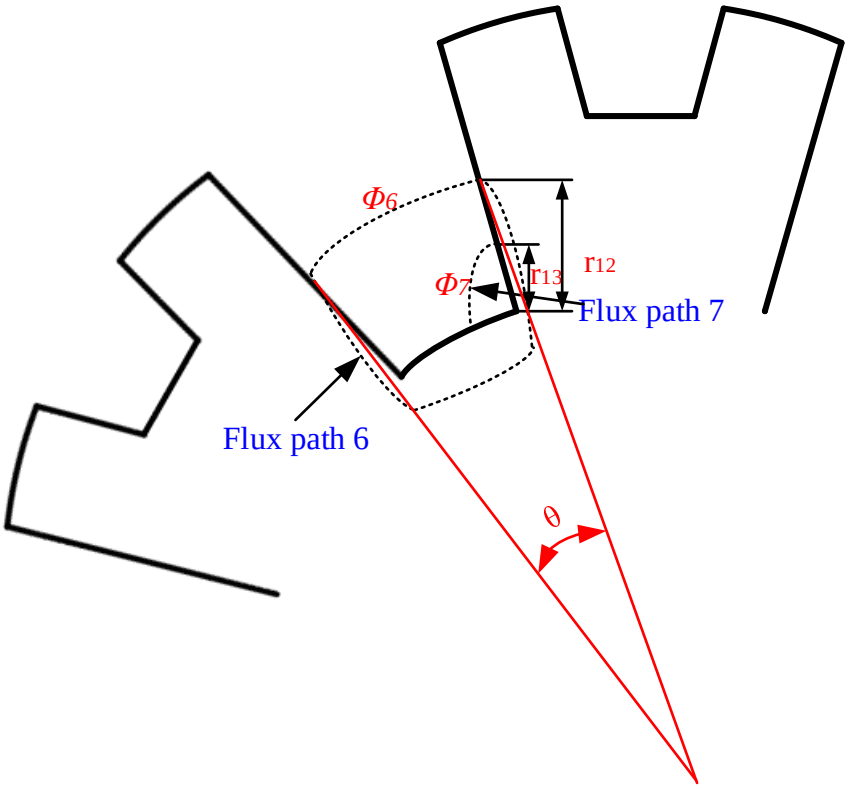

(b)

Fig. 3-9 Flux paths distribution at unaligned position between (a) the stator and rotor

(b) adjacent stator poles

A. Flux path 1

The EMC model of this path is shown in Fig. 3-10.

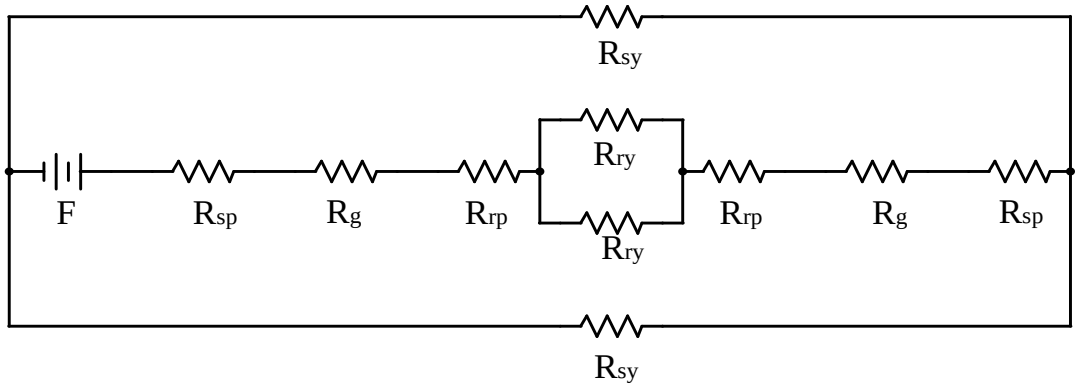

Fig. 3-10 EMC model of flux path 1

$$l_{g1} = h_{s1} + l_g \tag{3-34}$$

$$A_{sp1} = l_{slot} \cdot l \tag{3-35}$$

$$A_{rp1} = \frac{\theta_r}{4} \cdot \frac{D_{r1}}{2} \cdot l \tag{3-36}$$

$$A_{g1} = \frac{A_{sp1} + A_{rp1}}{2} \tag{3-37}$$

$$l_{sp1} = h_s - h_{s1} \tag{3-38}$$

$$l_{sy1} = \pi \cdot \frac{D_{s1} + D_{sh}}{4} \tag{3-39}$$

$$l_{ry1} = \pi \cdot \frac{D_{r2} - b_r}{4} \tag{3-40}$$

$$l_{rp1} = h_r \tag{3-41}$$

$$A_{sy1} = b_s \cdot l \tag{3-42}$$

$$A_{ry1} = b_r \cdot l \tag{3-43}$$

$$\Phi_1 = \frac{NI}{2R_{sp} + 2R_g + 2R_{rp} + \frac{R_{ry}}{2} + \frac{R_{sy}}{2}} \tag{3-44}$$

$$L_{u1} = \frac{N\Phi_1}{I} \tag{3-45}$$

In the formula above, h_{s1} is the height of stator inner slot; l_{slot} is the width of the bottom of the slot; D_{r1}, D_{r2} and D_{s1} is the inner diameter of the rotor, outer diameter of the rotor and inner diameter of the stator, respectively; b_s and b_r is the thickness of stator and rotor yoke, respectively. Some parameters are marked in Fig. 3-6.

B. Flux path 2

The effective lengths of l_{sy}, l_{ry}, l_{rp} and the cross areas of A_{sy} and A_{ry} are the same as those in flux path 1. The length of airgap is regarded as a π/3 arc angle with the corresponding chord connecting the starting point with the ending point in the airgap. The calculation method of average cross area in the airgap is the same as that in flux path 1. The EMC model is shown in Fig. 3-11.

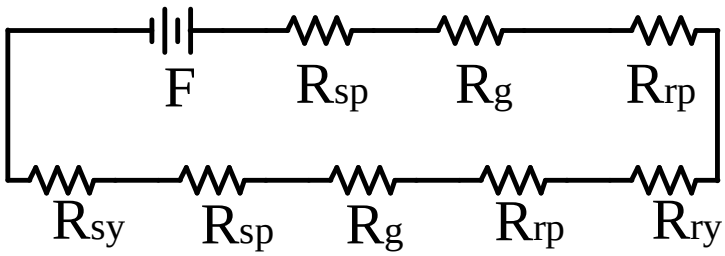

Fig. 3-11 EMC model of flux path 2

$$A_{sp2} = \frac{h_{s1} \cdot l}{2\cos(11.25^\circ)} \tag{3-46}$$

$$A_{rp2} = \frac{\theta_r}{4} \cdot \frac{D_{r1}}{2} \cdot l \tag{3-47}$$

$$l_{sp2} = h_s - \frac{3}{4} h_{s1} \tag{3-48}$$

$$\Phi_2 = \frac{F_2}{2(R_{sp} + R_g + R_{rp}) + (R_{sy} + R_{ry})} \tag{3-49}$$

$$L_{u2} = \frac{2N\Phi_2}{I} \tag{3-50}$$

C. Flux path 3

The lengths of l_{sy}, l_{ry}, l_{rp} and the cross areas of A_{sy} and A_{ry} are the same as those in flux path 1. The airgap length is also considered as π/3 arc. The EMC model is identical to Fig. 3-11.

$$A_{sp3} = \frac{h_{s1} \cdot l}{4\cos(11.25^\circ)} \tag{3-51}$$

$$A_{rp3} = \frac{3\theta_r}{32} \cdot \frac{D_{r1}}{2} \cdot l \tag{3-52}$$

$$l_{sp3} = h_s - \frac{3}{8} h_{s1} \tag{3-53}$$

$$\Phi_3 = \frac{F_3}{2(R_{sp} + R_g + R_{rp}) + (R_{sy} + R_{ry})} \tag{3-54}$$

$$L_{u3} = \frac{2N\Phi_3}{I} \tag{3-55}$$

D. Flux path 4

The lengths of l_{sy}, l_{ry}, l_{rp} and the cross areas of A_{sp}, A_{sy} and A_{ry} are the same as those in flux path 3. The airgap length is also considered as π/3 arc. The EMC model is identical to Fig. 3-11.

$$A_{rp4} = \frac{\theta_r}{32} \cdot \frac{D_{r1}}{2} \cdot l + \frac{h_r \cdot l}{16} \tag{3-56}$$

$$l_{sp4} = h_s \tag{3-57}$$

$$\Phi_4 = \frac{F_4}{2(R_{sp} + R_g + R_{rp}) + (R_{sy} + R_{ry})} \tag{3-58}$$

$$L_{u4} = \frac{2N\Phi_4}{I} \tag{3-59}$$

E. Flux path 5

The lengths of l_{sy}, l_{ry} and the cross areas of A_{sy} and A_{ry} are the same as those in flux path 3. The airgap length is considered as arc with unequal radius for approximate calculation. The EMC model is identical to Fig. 3-11.

$$A_{sp5} = \frac{\theta_s}{8} \cdot \frac{D_{s2}}{2} \cdot l \tag{3-60}$$

$$A_{rp5} = \frac{3h_r \cdot l}{16} \tag{3-61}$$

$$l_{sp5} = \frac{h_s}{\cos(11.25^\circ)} \tag{3-62}$$

$$l_{rp5} = \frac{27}{32} h_r \tag{3-63}$$

$$\Phi_5 = \frac{F_5}{2(R_{sp} + R_g + R_{rp}) + (R_{sy} + R_{ry})} \tag{3-64}$$

$$L_{u5} = \frac{2N\Phi_5}{I} \tag{3-65}$$

where D_{s2} is the stator outer diameter in the equation.

F. Flux path 6

The airgap length is considered as arc with unequal radius for approximate calculation. The EMC model is identical to Fig. 3-12.

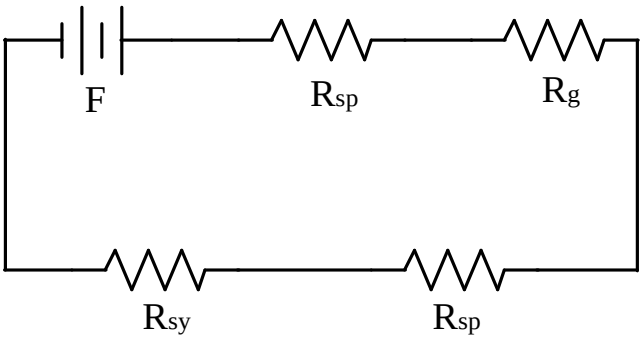

Fig. 3-12 EMC model of flux path 6

$$A_{sp6} = \frac{h_s}{4\cos(11.25^\circ)} \cdot l \tag{3-66}$$

$$A_{g6} = \frac{h_s}{4\cos(11.25^\circ)} \cdot l \tag{3-67}$$

$$l_{sp6} = \frac{5h_s}{8\cos(11.25^\circ)} \tag{3-68}$$

$$l_{sy6} = (\frac{D_{s1}}{2} - \frac{b_s}{4}) \cdot \theta \tag{3-69}$$

$$A_{sy6} = \pi \frac{D_{s1} + D_{sh}}{4} \cdot l \tag{3-70}$$

$$\Phi_6 = \frac{F_6}{2R_{sp} + R_g + R_{sy}} = \frac{\frac{3}{8} NI}{2R_{sp} + R_g + R_{sy}} \tag{3-71}$$

$$L_{u6} = \frac{4 \cdot (\frac{3}{8} N\Phi_6)}{I} \tag{3-72}$$

G. Flux path 7

The EMC model of this flux path is shown below in Fig. 3-13.

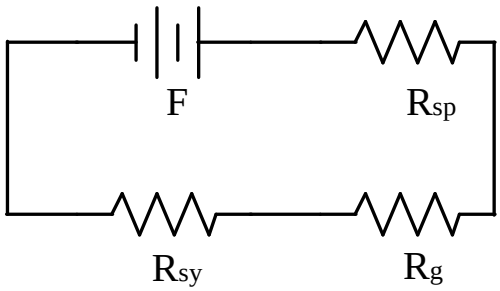

Fig. 3-13 EMC model of flux path 7

$$l_{sp7} = \frac{\frac{h_s}{4} + \frac{b_s}{4}}{\cos(11.25^\circ)} \tag{3-73}$$

$$l_{g7} = \frac{h_s}{4} \cdot \frac{\pi}{2} \tag{3-74}$$

$$l_{sy7} = \frac{h_s}{4} \tag{3-75}$$

$$A_{sp7} = \frac{h_s}{2} \cdot l \tag{3-76}$$

$$A_{g7} = \frac{h_s}{2} \cdot l \tag{3-77}$$

$$A_{sy7} = b_s \cdot l \tag{3-78}$$

$$\Phi_7 = \frac{F_7}{R_{sp} + R_g + R_{sy}} = \frac{\frac{1}{4} NI}{R_{sp} + R_g + R_{sy}} \tag{3-79}$$

$$L_{u7} = \frac{4 \cdot (\frac{1}{2} N\Phi_7)}{I} \tag{3-80}$$

H. Flux path 8

The cross areas of A_{sy} and A_{ry} are the same as those in flux path 3. The length of l_{sp} is identical to that in flux path 5. The EMC model can be obtained from Fig. 3-14.

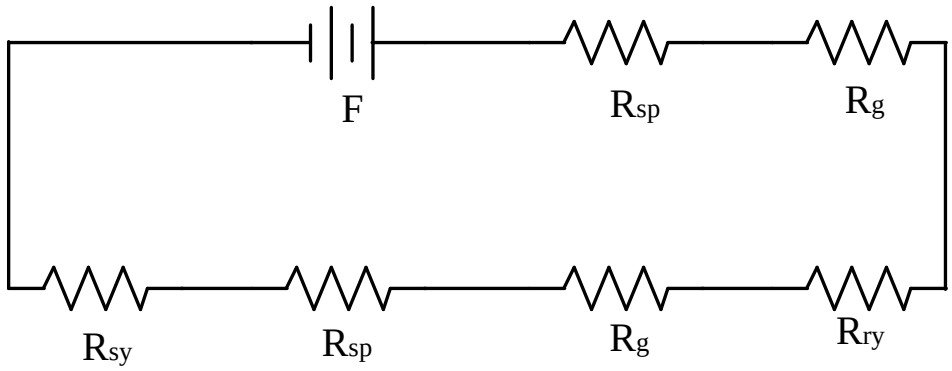

Fig. 3-14 EMC model of flux path 8

$$l_{g8} = l_g + h_r \tag{3-81}$$

$$A_{sp8} = \frac{\theta_s}{2} \cdot l \cdot \frac{D_{s2}}{2} \tag{3-82}$$

$$A_{r8} = (\frac{D_{r1}}{2} + h_r) \cdot (22.5^\circ - \theta_s) \cdot l \tag{3-83}$$

$$A_{g8} = \frac{A_{sp8} + A_{r8}}{2} \tag{3-84}$$

$$l_{ry8} = \frac{180 - 22.5}{360} \pi (D_{r2} - b_r) \tag{3-85}$$

$$l_{sy8} = \frac{180 - 22.5}{720} \pi (D_{s1} + D_{sh}) \tag{3-86}$$

$$\Phi_8 = \frac{F_8}{2R_{sp} + 2R_g + R_{sy} + R_{ry}} \tag{3-87}$$

$$L_{u8} = \frac{2N\Phi_8}{I} \tag{3-88}$$

I. Flux path 9

The length of l_{sp} and l_{sy} is the same as that in flux path 5 and flux path 8, respectively while the cross section areas of A_{sy} and A_{ry} are identical to those in flux path 3. The airgap length is considered as π/3 arc as well. Also, the EMC model is identical to Fig. 3-11.

$$A_{sp9} = \frac{\theta_s}{8} \cdot \frac{D_{s2}}{2} \cdot l \tag{3-89}$$

$$A_{rp9} = \frac{h_r}{3} \cdot l \tag{3-90}$$

$$l_{rp9} = \frac{h_r}{6} \tag{3-91}$$

$$l_{ry9} = \frac{135 + \theta_r}{360} \pi (D_{r2} - b_r) \tag{3-92}$$

$$\Phi_9 = \frac{F_9}{2(R_{sp} + R_g + R_{rp}) + (R_{sy} + R_{ry})} \tag{3-93}$$

$$L_{u9} = \frac{2N\Phi_9}{I} \tag{3-94}$$

J. Flux path 10

The cross section areas of A_{sy} and A_{ry} are identical to those in flux path 3 while the length of l_{sp} is the same as that in flux path 8. Besides, the values of l_{sy} and l_{ry} are equal to those in flux path 9. The airgap length is considered as π/3 arc and the EMC model is identical to Fig. 3-11.

$$A_{sp10} = \frac{\theta_s}{8} \cdot \frac{D_{s2}}{2} \cdot l \tag{3-95}$$

$$A_{rp10} = \frac{3h_r}{16} \cdot l \tag{3-96}$$

$$l_{rp10} = \frac{27h_r}{32} \tag{3-97}$$

$$\Phi_{10} = \frac{F_{10}}{2(R_{sp} + R_g + R_{rp}) + (R_{sy} + R_{ry})} \tag{3-98}$$

$$L_{u10} = \frac{2N\Phi_{10}}{I} \tag{3-99}$$

K. Flux path 11

l_{sp} is the same as that in flux path 5 and l_{rp}, A_{sy}, A_{ry} are equal to those in flux path 3. Moreover, the values of l_{sy} and l_{ry} are identical to those in flux 9. The airgap length is considered as π/3 arc and the EMC model is identical to Fig. 3-11.

$$A_{sp11} = \frac{h_{s1}}{4} \cdot l \tag{3-100}$$

$$A_{rp11} = \frac{h_r}{16} \cdot l + \frac{\theta_r}{32} \cdot \frac{D_{r1}}{2} \cdot l \tag{3-101}$$

$$\Phi_{11} = \frac{F_{11}}{2(R_{sp} + R_g + R_{rp}) + (R_{sy} + R_{ry})} \tag{3-102}$$

$$L_{u11} = \frac{2N\Phi_{11}}{I} \tag{3-103}$$

L. Flux path 12

The lengths of l_{rp}, l_{ry}, l_{sy} and cross sectional areas of A_{sp}, A_{ry}, A_{sy} are identical to those in flux path 11. The airgap length is considered as arc with unequal radius for approximate calculation. The EMC model is identical to Fig. 3-11.

$$A_{rp12} = \frac{\theta_r}{8} \cdot \frac{D_{r1}}{2} \cdot l \tag{3-104}$$

$$l_{sp12} = \frac{h_s - \frac{3}{8} h_{s1}}{\cos(11.25^\circ)} \tag{3-105}$$

$$\Phi_{12} = \frac{F_{12}}{2(R_{sp} + R_g + R_{rp}) + (R_{sy} + R_{ry})} \tag{3-106}$$

$$L_{u12} = \frac{2N\Phi_{12}}{I} \tag{3-107}$$

M. Flux path 13

The lengths of l_{rp}, l_{sp} and cross sectional areas of A_{sp}, A_{rp}, A_{sy}, A_{ry} are identical to those in flux path 9. Furthermore, the values of l_{sy} and l_{ry} are the same as those in flux path 5. The airgap length is considered as π/3 arc and the EMC model is identical to Fig. 3-11.

$$\Phi_{13} = \frac{F_{13}}{2(R_{sp} + R_g + R_{rp}) + (R_{sy} + R_{ry})} \tag{3-108}$$

$$L_{u13} = \frac{2N\Phi_{13}}{I} \tag{3-109}$$

Therefore, the total self-inductance at the unaligned position L_u can be expressed as

$$L_u = \sum_{i=1}^{13} L_{ui} \tag{3-110}$$

3.3.2.2 Aligned Position

The maximum self-inductance can be obtained from the fully aligned position. The flux paths distribution is shown in Fig. 3-15 (a) and (b). Due to the exactly aligned position of stator teeth and rotor poles, just two flux paths can stand for the self-inductance calculation.

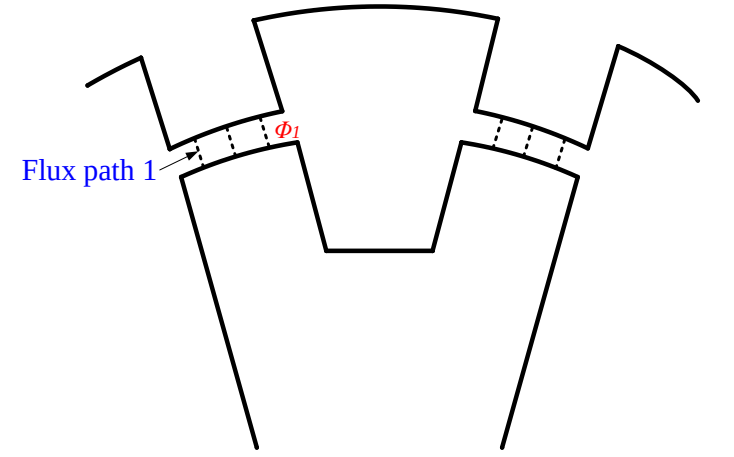

(a)

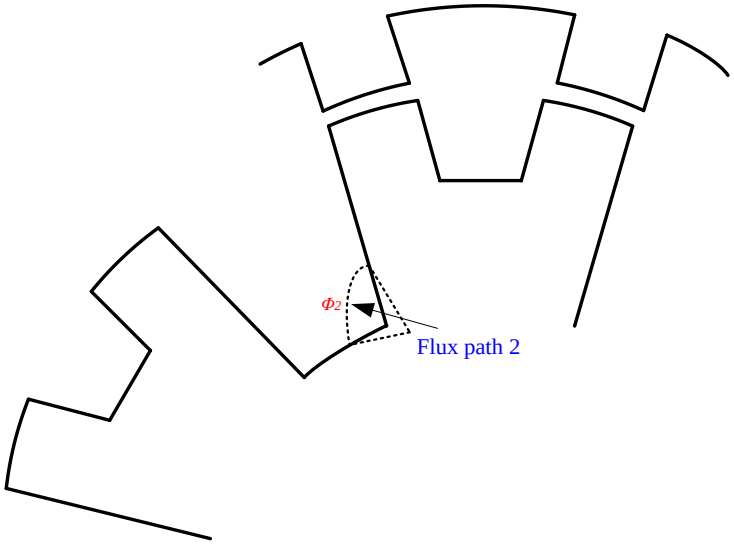

(b)

Fig. 3-15 Flux paths distribution at aligned position between (a) the stator and rotor (b) adjacent stator poles

A. Flux path 1

The EMC model is just the same as that in flux path 3 of the unaligned position. Besides, the values of A_{sy} and A_{ry} are also equal to those in flux 3.

$$l_{g1} = l_g \tag{3-111}$$

$$A_{sp1} = \frac{D_{s2}}{2} \cdot \theta_s \cdot l \tag{3-112}$$

$$A_{rp1} = \frac{D_{r1}}{2} \cdot \theta_r \cdot l \tag{3-113}$$

$$A_{g1} = \frac{A_{sp1} + A_{rp1}}{2} \tag{3-114}$$

$$l_{sp1} = \frac{h_s}{\cos(11.25^\circ)} \tag{3-115}$$

$$l_{rp1} = h_r \tag{3-116}$$

$$l_{ry1} = \frac{180 - 22.5}{360} \pi (D_{r2} - b_r) \tag{3-117}$$

$$l_{sy1} = \frac{180 - 22.5}{720} \pi (D_{s1} + D_{sh}) \tag{3-118}$$

$$\Phi_1 = \frac{F_1}{2(R_{sp} + R_g + R_{rp}) + (R_{sy} + R_{ry})} \tag{3-119}$$

$$L_{a1} = \frac{2N\Phi_1}{I} \tag{3-120}$$

B. Flux path 2

This flux path is almost the same as that in flux path 7 at the unaligned position. So, the calculation result of L_{a2} is equal to the value of L_{u7}.

Therefore, the total self-inductance at the aligned position L_a can be expressed as

$$L_a = L_{a1} + L_{a2} \tag{3-121}$$

3.3.3 Genetic Algorithm Application for Optimization

From the above analysis, the value of self-inductance can be calculated and the error

compared with 2D-FEM result is within 3%. For the optimization of the topology and its application to EVs, the most important factors are lighter weight and higher efficiency with the same torque performance. Therefore, the target for optimization is to maximize the summation of torque per unit of weight and copper loss, both of which are multiplied by weight coefficients, to set up a suitable fitness function. Then, GA process is utilized to calculate the maximum of the function.

The weight coefficients of specific torque and torque per unit copper loss are set as ω_1 and ω_2, respectively. So the fitness function can be expressed as,

$$F = 1000 \cdot (\omega_1 \cdot \frac{T_{avg}}{weight} + \omega_2 \cdot \frac{T_{avg}}{loss}) \tag{3-122}$$

where T_{avg} is the average torque produced by one phase during half an electric period , *weight* is composed of that of steel and copper, *loss* is the copper loss during the above conducting period and *1000* is the multiplier for larger fitness value.

The value of T_{avg} can be calculated as follows:

$$T_{avg} = \frac{1}{2} \frac{L_a - L_u}{\theta_{half}} I^2 \tag{3-123}$$

where, L_a and L_u is the self-inductance at aligned and unaligned position, respectively; θ_{half} is the arc angle of half an mechanical position period; I is the ideal square waveform current injected into the windings. Mutual inductance is neglected as the value is relatively much smaller when compared with self-inductance. The value of self-inductance is a sum of individual inductances obtained from different flux lines in the EMC model as calculated before. Some parameters of the motor are kept as constants, including the outer diameter of rotor 382 mm, air gap length 0.5 mm, shaft

diameter 100 mm and stack length 74 mm according to the motor size in [95]. On the other hand, the rotor inner diameter D_{r1}, rotor pole height h_r, stator inner diameter D_{s1}, stator teeth arc angle θ_s, slot depth in the stator pole h_{s1} and rotor pole arc angle θ_r are set as the variable to be optimized.

Moreover, some constraints need to be considered. Some design limitations of the SRM structure are needed based on [100] shown in the following equations.

$$\frac{l_p}{2} \le b_s < l_p \tag{3-124}$$

$$\frac{l_p}{2} \le b_r < l_p \tag{3-125}$$

where b_s, b_r is the thickness of stator and rotor yoke, respectively and l_p is the width of stator pole. Also, the slot area should be large enough for suitable number of winding turns.

$$A_{slot} \ge 1400mm^2 \tag{3-126}$$

Moreover, to avoid high saturation in the stator pole causing large torque ripple, a minimum restriction of the width of stator pole is required.

$$l_p \ge 50mm \tag{3-127}$$

In addition, for in-wheel motors, because of natural cooling condition, the current density is limited to 3-5A/mm^2 and the slot packing factor is set at about 0.44. For this motor, considering long time stable operation, the current density is limited to no more than 3 A/mm^2. The weight coefficients ω_1 and ω_2 are both evaluated as 0.5.

For GA parameters, the considerations are as follows:

1) The population number is set as 20.

2) The maximum generation is limited to 20.

3) The crossover probability is 0.8.

4) The mutation is 0.04.

To improve the GA performance, rank fitness scaling is utilized to remove the effect of initial value boundary. For selection, stochastic uniform is preferred. Elite count can directly go into the next generation to accelerate the optimization and the number is set as 2, ten percent of the total population number. The variation of mean and best fitness function during optimization process can be obtained from Fig. 3-16. Furthermore, the optimization procedure is shown in the flowchart in Fig. 3-17. With the constant value of some parameters considered, the final optimized parameters are listed in Table 3-1.

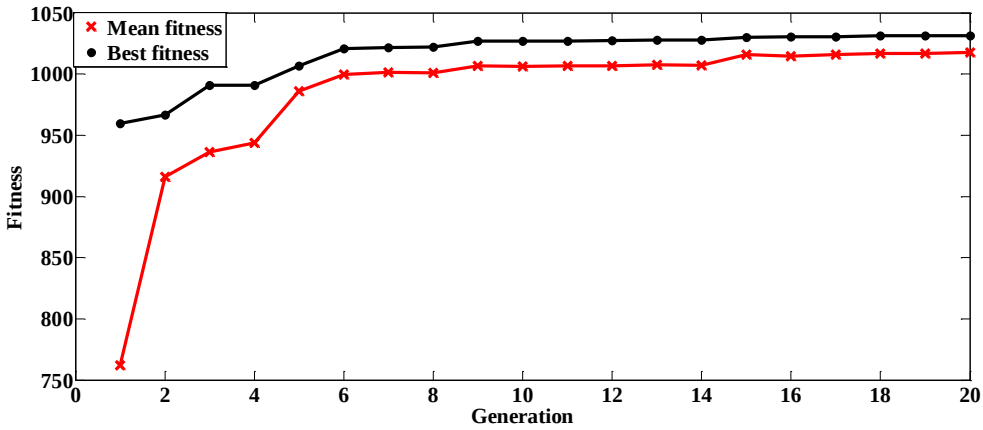

Fig. 3-16 Fitness value variation during optimization

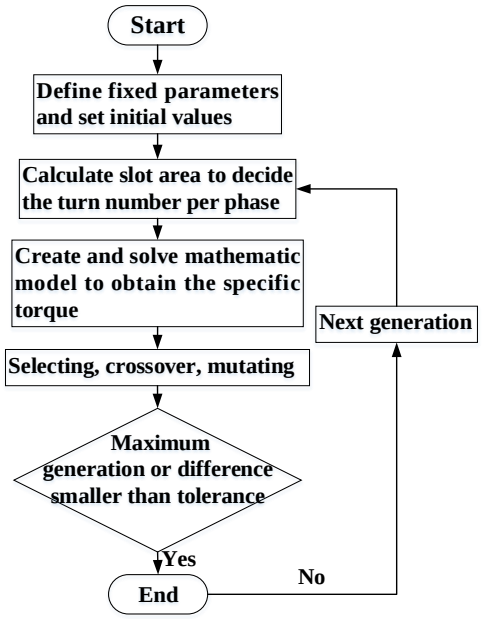

Fig. 3-17 Flowchart of the optimization procedure

Table 3-1
Optimized Variable Parameters

Parameter	Value	Parameter	Value
D_{r1} (mm)	299	h_{s1} (mm)	19
h_r (mm)	10	θ_s (degree)	8
D_{s1} (mm)	163	θ_r (degree)	9.5

3.4 Performance Analysis and Comparison

The characteristics of the optimized motor, including flux density, torque and core loss, are analyzed by 2D-FEM. For the rated operation condition of motors, flux densities of different positions when phase A is conducting are shown in Fig. 3-18.

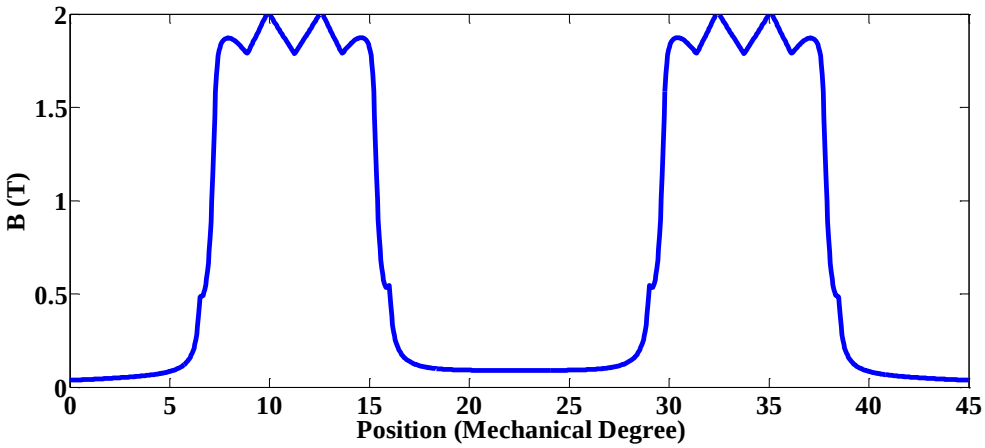

Fig. 3-18 Flux density in the airgap of different positions for the proposed topology

To show the superiority of the proposed motor in high performance, a 6/8 and a 6/10 SRMs in Fig. 3-19 (a) and (b) are chosen for comparison. They are of the same outline size with the proposed topology. The geometric parameters of the counterparts are also optimized by GA method for persuasive comparison. The objective function considers torque output, weight and energy loss as well. The basic parameters of the three optimized motors can be found in Table 3-2.

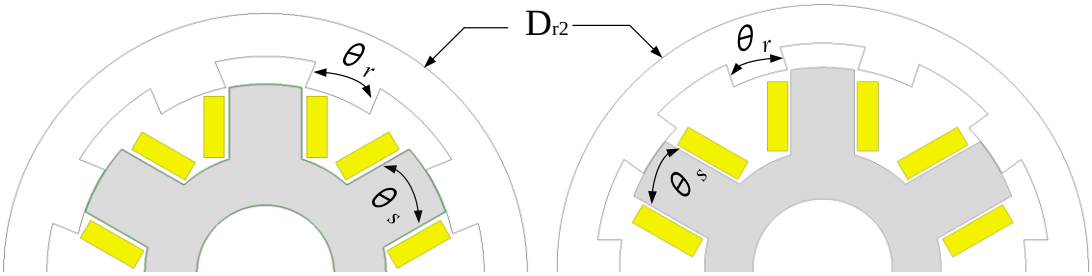

Fig. 3-19 Half cross section of (a) 6/8 SRM (b) 6/10 SRM

Table 3-2
Basic Parameters of the SRMs

Dimensions	6/8 SRM	6/10 SRM	Proposed SRM
Rotor outer diameter D_{r2} (mm)	382	382	382
Stack length l (mm)	74	74	74
Airgap length l_g (mm)	0.5	0.5	0.5
Stator pole/teeth arc angle θ_s (degree)	22	18	8
Rotor pole arc angle θ_r (degree)	21	16	9.5
Number of turns per phase N	184	248	204
Coil end length (mm)	17.5	19.7	14.9
Copper wire diameter (mm)	1.12	1.12	1.12
Number of parallel windings	8	8	8
Slot fill factor	0.44	0.44	0.44

All the three motors are running at the same suitable total energy loss according to the temperature rise effect with the rated speed of 1000 rpm which corresponds to the speed of the vehicle. The dimension of them are the same on the basis of [90], with rotor outer diameter 382 mm, stack length 74 mm, airgap length 0.5 mm. Because of a higher frequency of commutation, core loss of the proposed topology is higher than that of its counterparts under similar saturation condition. The saturation situation of the three motors can be obtained from Fig. 3-20 (a), (b) and (c). Therefore, the copper loss is at a lower value for the proposed topology, resulting in lower current density.

But for 6/10 SRM, the number of turns per phase is the largest. Considering the same loss, its current density is limited to a lower value than 6/8 SRM, only slightly higher than the proposed motor. With the same diameter of copper wire, the RMS current of 6/10 SRM is only slightly larger than the proposed one. The value of loss is on the basis of the motor of the same size in [95]. The torque performance comparisons of one phase conducting in half an electric period from the unaligned position to aligned one with ideal square wave current and full phase conducting with each phase conducting for half an electric period are shown in Fig. 3-21 and Fig. 3-22, respectively with the rated speed for EVs at 1000 rpm based on 2D-FEM computation. The detailed data of motor performance can be obtained from Table 3-3.

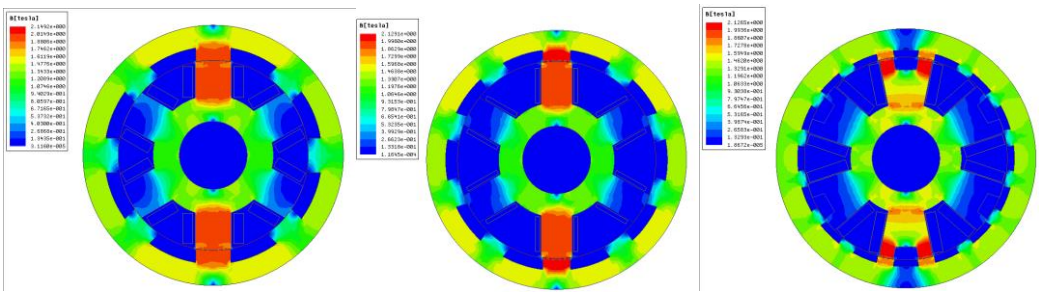

Fig. 3-20 Magnetic saturation situation of (a) 6/8 SRM (b) 6/10 SRM (c) proposed 6/16 SRM

Fig. 3-21, Fig. 3-22 and Table 3-3 indicate that for the same total loss, the novel topology can provide higher output torque and less torque ripple. Also, the specific torque is much higher than the conventional ones, about 48% more than that of 6/8 and 28% more than that of 6/10 SRM. This result shows that the proposed topology has its potential in the application to EVs for higher propulsion force, higher efficiency and lighter weight. Although the 6/10 SRM provides 77% torque output of the proposed topology, it is at the expense of increasing 14% of copper wires, which means higher

cost and heavier weight.

Table 3-3
Torque Characteristics Comparison of Three SRMs

Dimensions	6/8 SRM	6/10 SRM	Proposed SRM
Current density (A/mm^2)	3.00	2.60	2.54
RMS current(A)	23.6	20.4	20.0
Winding weight (kg)	13.2	17.4	15.2
Core weight (kg)	42.6	39.1	41.8
Total weight (kg)	55.8	56.5	57.0
Core loss (W) (FEM)	45	47	90
Winding loss (W)	274	272	229
Mechanical loss (W)	62	62	62
Stray loss (W)	27	27	27
Total loss (W)	408	408	408
Power (kW)	11.0	12.9	16.7
Torque (Nm)	105	123	159
Torque ripple (%)	63	67	36
Specific Torque ratio (Nm/kg)	1.88	2.18	2.79
Torque/copper loss (Nm/W)	0.38	0.45	0.70
Efficiency (%)	96.4%	96.9%	97.6%

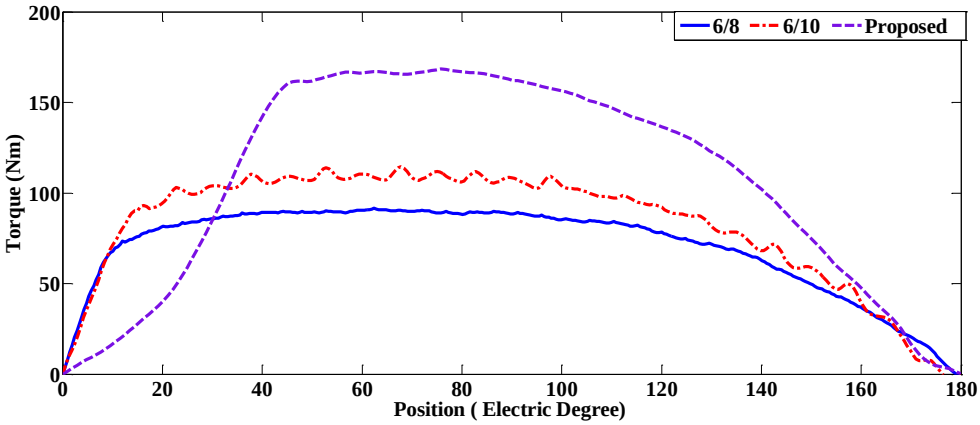

Fig. 3-21 Phase torque waveforms of three motors

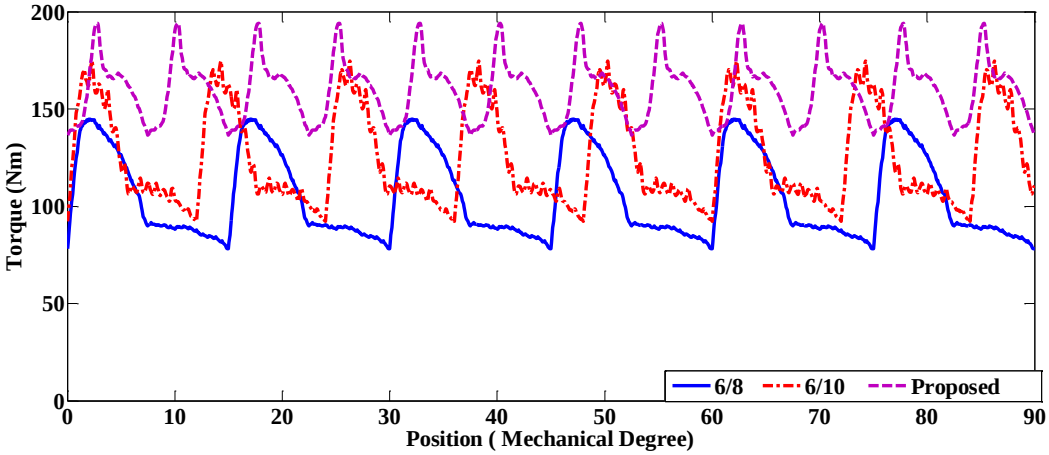

Fig. 3-22 Full phase torque waveforms of three motors

3.5 Summary

A novel in-wheel SRM topology is presented in this paper for direct drive, high propulsion and light weight application in EVs. The proposed motor combines the advantage of multi-tooth per stator pole and more rotor poles than stator teeth to achieve the purpose of enhancing the specific torque. The structure of two teeth can improve the output torque. Increasing the number of rotor poles results in larger slot area for winding and allows larger excitation current. The principle of multiple teeth

per stator pole is proved by equivalent magnetic circuit and a new design formula is put forward to select the number of rotor poles.

Then, the GA method is carried out to make optimization for the geometric parameter. Moreover, the characteristics of the motor are calculated and analyzed by utilizing 2D-FEM. The performance is compared with that of 6/8 and 6/10 three phase SRMs to prove its higher specific torque, efficiency and lower torque ripple. In addition, the shape of the stator is convenient for automatic winding and the topology will have prospects for mass production. In summary, the proposed motor shows strong competitiveness for its application to future EVs.

Chapter 4

Design of a Novel Hybrid Reluctance Motor

SRM has a simple and robust structure, independent phase conducting for better fault tolerance and possess a wide speed range. However, without the utilization of PMs, the torque density is relatively lower compared with PM motors. Therefore, introducing PM material into the SRM becomes a viable idea. PM, however, is rare earth material which is expensive. In this chapter, design of a motor with a small amount of PM material inserted into the SRM is presented. This enables to regulate the magnetic flux produced from current excitation and the torque improvement is quite significant.

4.1 Introduction

The SRM has recently received a great deal of attention due to its characteristics of simple, rugged configuration (a doubly salient structure and no windings on the rotor) and elimination of PM usage. Its torque production comes from the magnetic saliency between the stator and rotor poles. Its in-wheel version, whose outer rotor is integrated straight within the rim, further leads the new method of direct drive and thus reduces space and transmission loss.

Although PM motors have been dominating the market especially amongst in-wheel solutions due to its high torque density [101-102], unavoidable cogging torque exists and the cost is quite high due to the usage of PM poles. The idea of adding PMs into SRMs with little cogging torque is presented in [103-104] by inserting the PM material between stator poles and into the stator yoke, respectively. And a torque distribution method in [105] is proposed to separate the torque produced by PMs and excitation current individually. Due to the working condition of magnetic saturation for most SRMs [106], however, the flux increase in the airgap is quite limited. Hence, it is difficult to improve torque density significantly in [103-104].

The multi-tooth SRM topology has been proposed in the former discussion. Nevertheless, the extremely high saturation in the stator pole increases the magnetic reluctance, inhibiting higher torque output and causing higher torque ripple. Moreover, the slot area is quite small for sufficient windings.

This chapter presents an in-wheel hybrid reluctance motor combining PMs between two adjacent stator poles and multiple teeth per stator pole. PMs not only act

as a role to increase the magnetic flux, but also help to lower the saturation level in the stator pole, thus decreasing the core reluctance which is quite necessary for multiple teeth topology. Therefore, the topology of the multiple teeth per pole can provide enough torque output effectively with lower torque ripple.

4.2 Characteristics Analysis of the Novel Topology

4.2.1 Structure Analysis

A. Selection of Number of Phases & Rotor Poles

Because of inserting PMs between adjacent stator poles and stable working situation, the phase number has to be odd. Also, with the number of teeth per stator pole considered as discussed in Chapter 3, two teeth topology is the most suitable. Therefore, a three phase motor is selected in case of large number of rotor poles, and the number of rotor poles is ten.

B. Structure of the Motor

The proposed topology is a 6/10 SRM with two teeth per stator pole and a PM set between two adjacent stator poles as shown in Fig. 4-1 where the red arrows represent the magnetization direction of PMs. The counterpart is a 6/10 two teeth per pole SRM shown in Fig. 4-2.

The novel motor, consisting of three phases named AA′, BB′ and CC′, adopts the conducting mode and winding configuration of conventional SRMs, with one or two phase conducting at the same time and concentrated winding. The only difference from conventional ones is that the current direction on adjacent phases must be reversed as

shown in Fig. 4-3 (b). DR-510 silicon steel is selected as the component of the stator and rotor cores and the material of PMs is chosen as N35SH.

Six PMs in total are set between adjacent stator poles, with much smaller volume than those applied in PM synchronous motors. The magnetization direction of these PMs ensures the declination of magnetic saturation in the stator poles.

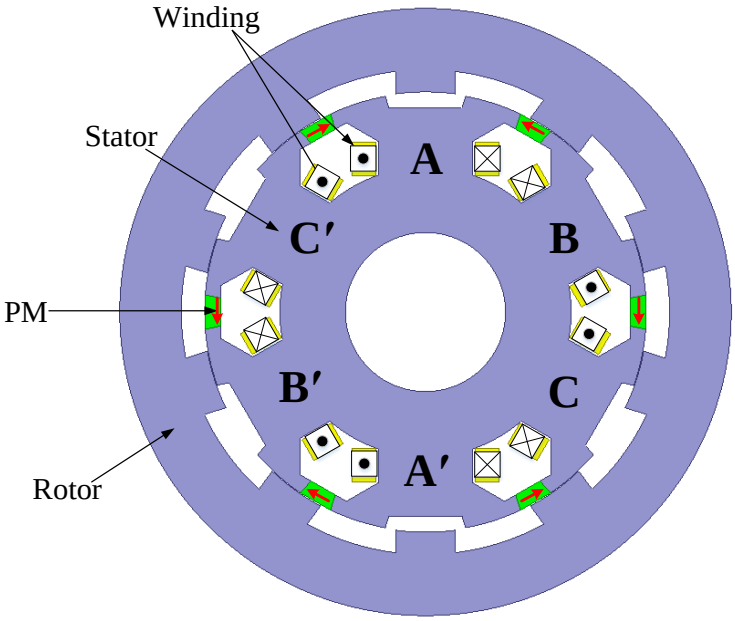

Fig. 4-1 Schematic of the proposed hybrid reluctance motor

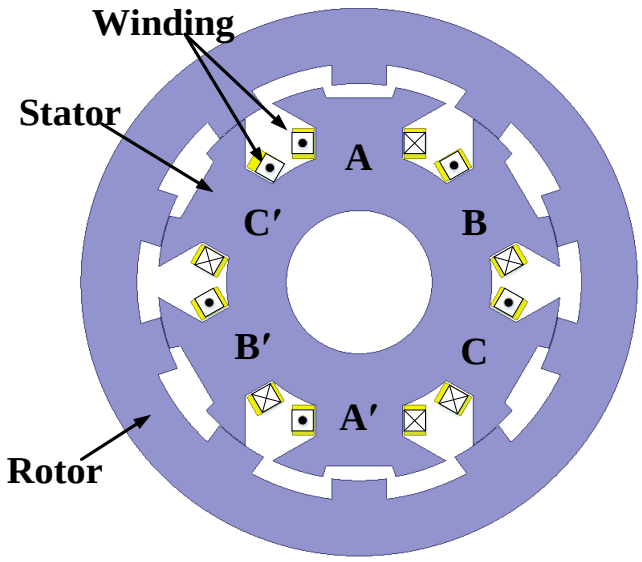

Fig. 4-2 Schematic of 6/10 two teeth per pole SRM

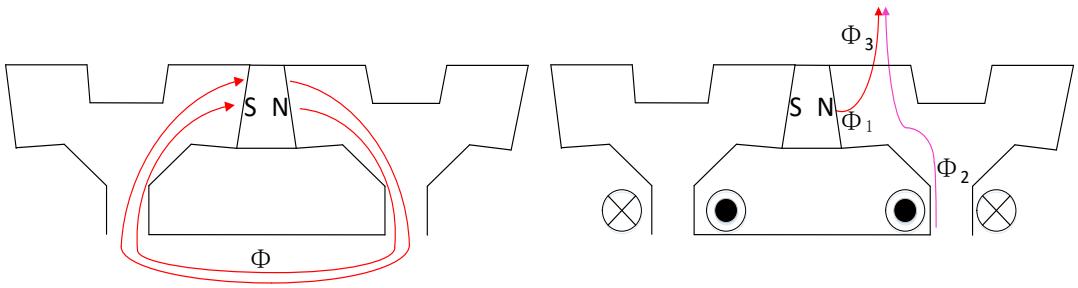

Fig. 4-3 Flux distribution with (a) non-excitation (b) excitation

4.2.2 Working Principle Analysis of the Proposed Topology

The theoretical calculation takes two adjacent phases with a PM for analysis. The flux distributions under excitation and non-excitation current conditions are shown in Fig. 4-3 (a) and (b) respectively. When there is no current excitation, the cogging torque is nearly zero due to the fact that almost all the magnetic flux passes through the stator. The results of cogging torque under no load condition, with the optimized size as discussed later, can be obtained from Fig. 4-4 by using 2D-FEM. It can be seen from Fig. 4-4 that the cogging torque has a small value. In Fig. 4-3 (b), Φ_1, Φ_2, Φ_3 is the magnetic flux in PM, stator pole and airgap, respectively. Φ_1 is greater than zero to prevent demagnetization of PM.

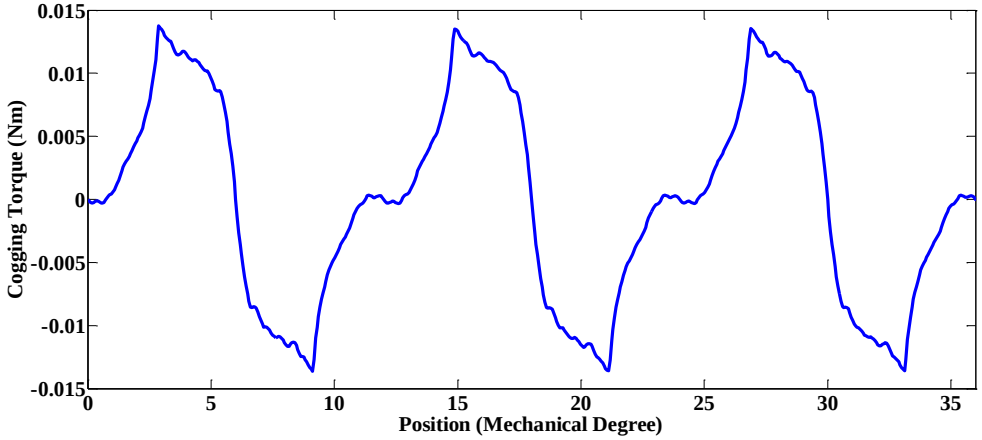

Fig. 4-4 Cogging torque of the proposed topology

The equivalent magnetic circuit model under excitation condition is shown in Fig. 4-5.

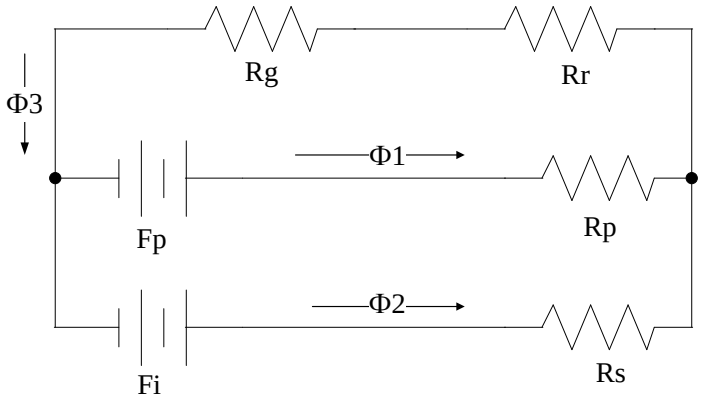

Fig. 4-5 Equivalent magnetic circuit under excitation condition

With Kirchhoff laws KVL and KCL considered, the equations of magnetic circuit are expressed as

$$\begin{cases} \Phi_3 = \Phi_1 + \Phi_2 \\ F_p = \Phi_1 R_p + F_i - R_s \Phi_2 \\ F_p = \Phi_1 R_p + (R_g + R_r)\Phi_3 \end{cases} \tag{4-1}$$

where, F_p and F_i is the magneto motive force provided by the PM and current respectively; R_g, R_r, R_p and R_s is the reluctance of airgap, rotor, PM and stator, respectively. The results can be solved as

$$\begin{cases} \Phi_1 = \dfrac{(R_r + R_g + R_s)F_p}{(R_r + R_g)(R_p + R_s) + R_s R_p} - \dfrac{(R_g + R_r)F_i}{(R_r + R_g)(R_p + R_s) + R_s R_p} \\ \Phi_2 = \dfrac{(R_r + R_g + R_p)F_i}{(R_r + R_g)(R_p + R_s) + R_s R_p} - \dfrac{(R_g + R_r)F_p}{(R_r + R_g)(R_p + R_s) + R_s R_p} \\ \Phi_3 = \dfrac{R_p F_i}{(R_r + R_g)(R_p + R_s) + R_s R_p} + \dfrac{R_s F_p}{(R_r + R_g)(R_p + R_s) + R_s R_p} \end{cases} \tag{4-2}$$

Φ_2 and Φ_3 can be transformed to

$$\Phi_2 = \frac{F_i}{R_s + \frac{R_p}{R_p + R_g + R_r}(R_r + R_g)} - \frac{R_r + R_g}{(R_r + R_g + R_s)R_p + (R_r + R_g)R_s} F_p \quad (4\text{-}3)$$

$$\Phi_3 = \frac{F_i}{R_g + R_r + R_s + \frac{R_s(R_r + R_g)}{R_p}} + \frac{R_s}{(R_g + R_r + R_s)R_p + R_s(R_r + R_g)} F_p \quad (4\text{-}4)$$

Considering about $R_p >> R_g + R_r$, $R_p >> R_s$ and the equation

$$F_p = H \cdot l \quad (4\text{-}5)$$

$$R_p = \frac{l}{\mu A} \quad (4\text{-}6)$$

where, H is the magnetic coercive force, l is the length of magnetization direction, μ and A is the magnetic permeability and cross-sectional area of PM in the magnetization direction, respectively. Equation (4-3) and (4-4) can be simplified and estimated as

$$\Phi_2 \approx \frac{F_i}{R_s + R_r + R_g} - \frac{(R_r + R_g)H\mu A}{R_r + R_g + R_s} \quad (4\text{-}7)$$

$$\Phi_3 \approx \frac{F_i}{R_s + R_r + R_g} + \frac{R_s H \mu A}{R_r + R_g + R_s} \quad (4\text{-}8)$$

For the topology without PMs, the simple EMC model can be obtained from Fig. 4-6. And Φ_2 and Φ_3 can be calculated as

$$\Phi_2 = \Phi_3 = \frac{F_i}{R_s + R_r + R_g} \quad (4\text{-}9)$$

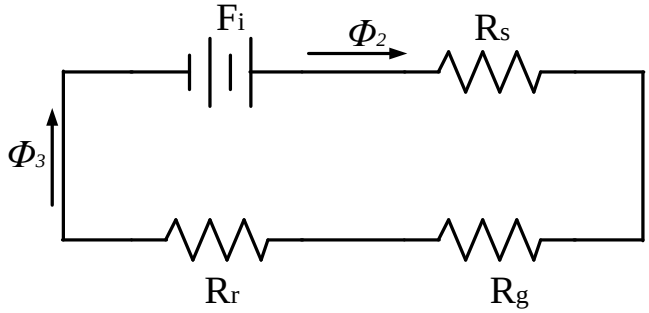

Fig. 4-6 EMC model of topology without PMs

Therefore, the comparison of Φ_2 and Φ_3 between PMs and non-PMs condition shows that the magnetic flux in the stator pole decreases while that in the air gap increases. Moreover, because of $R_s << R_g$, the increase of flux in the air gap is small while the decrease of flux in the stator pole is quite significant, thus reducing the saturation. By using 2D-FEM, the magnetic flux density distribution in the stator pole at 10 degree position (unaligned position set as zero) of the two motors is shown in Fig. 4-7 (a) and (b), respectively.

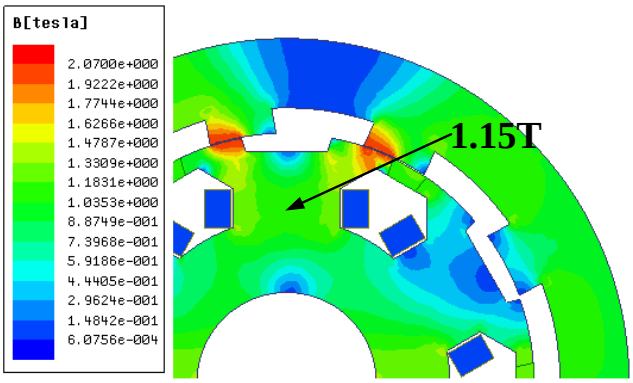

(a)

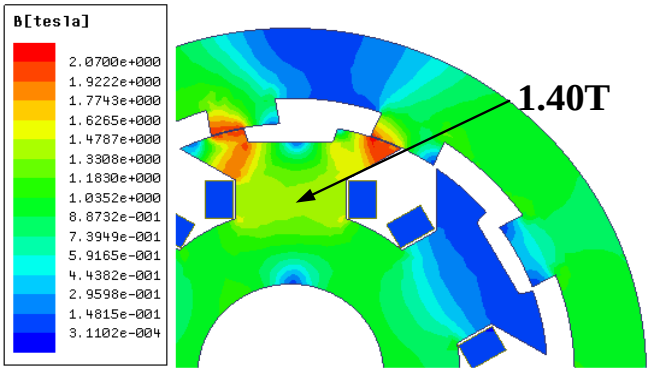

(b)

Fig. 4-7 Flux density distribution (a) with PMs (b) without PMs

A half period torque comparison between two teeth per stator pole with and without PMs is shown in Fig. 4-8. The current density of both motors is set as 5A/mm^2. The

torque improvement is about 25%.

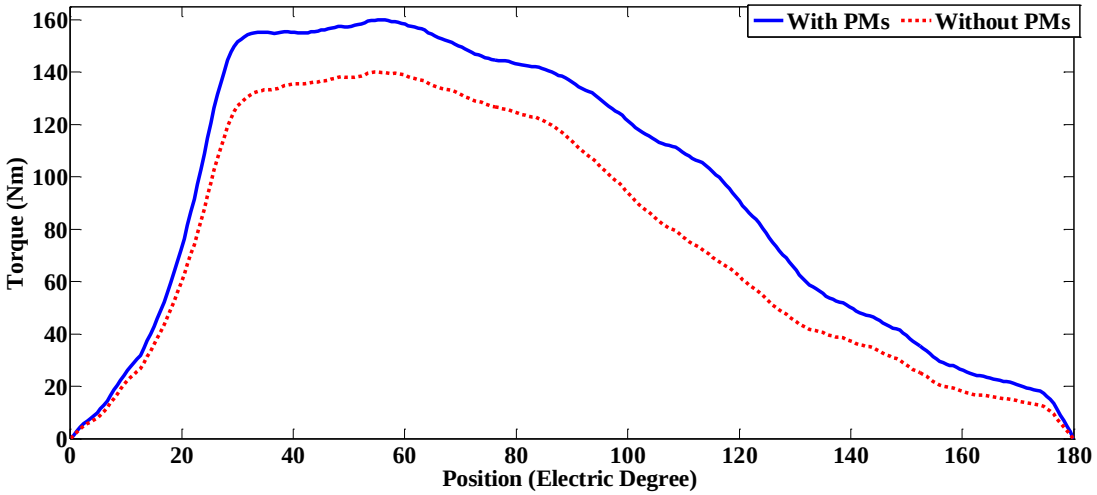

Fig. 4-8 Phase torque comparison between SRMs with and without PMs

4.3 Design & Optimization of the topology

4.3.1 Design of the Topology

The design and optimization of the motor is based on FEA and GA. For two teeth per stator pole 6/10 SRM, it should satisfy $\theta_{slot}+\theta_s=36$ ° for the purpose of continuous conducting, as defined and calculated similarly in Chapter 3, where θ_{slot} and θ_s is the arc angle of stator slot and stator teeth respectively. The commutation angle is 12 degree.

4.3.2 Optimization of the Topology

The optimization is firstly conducted by FEA to determine the shape of the stator pole, based on lower saturation and sufficient area for winding. To obtain the best torque performance and consideration of the application to EVs, the optimization

objective is to maximize the specific torque (torque per unit of motor weight), while keeping the weight as low as possible because it leads to better market performance. The equivalent magnetic circuit method and GA are utilized to set up the fitness function and calculate its maximum. The optimized shape of the stator pole is shown in Fig. 4-9 with parameters marked on it.

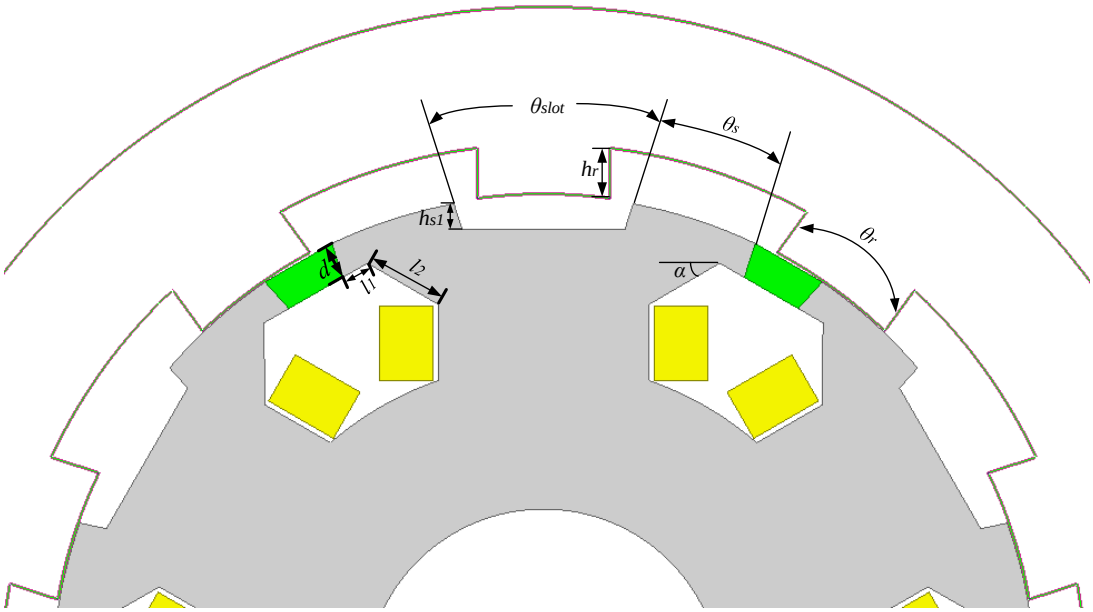

Fig. 4-9 Stator pole & its parameters

The mutual coupling effect between phases can be neglected, only self-inductance is taken into consideration. A comparison of self and mutual inductance can be found in Fig. 4-10 (a) and (b) with current value 40 Ampere ensuring suitable current density.

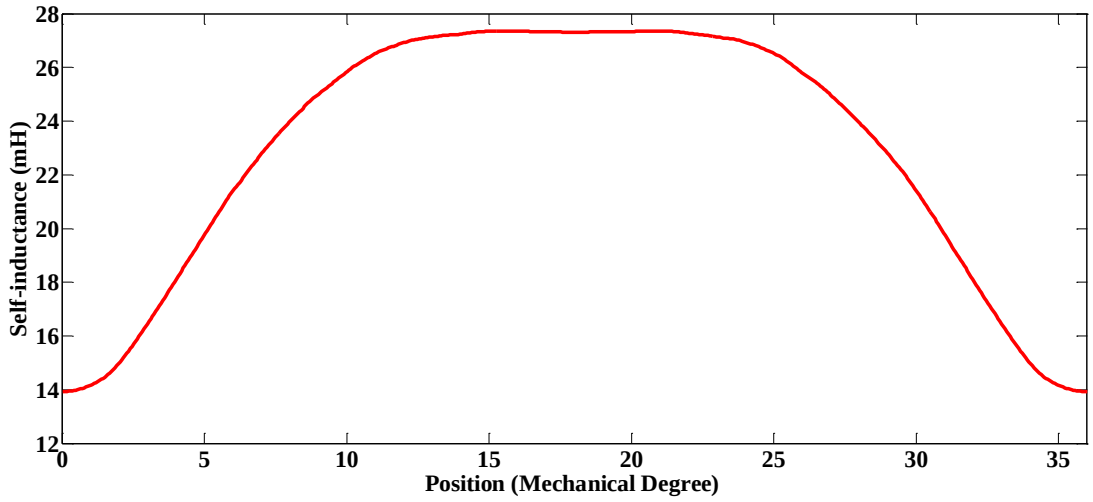

(a)

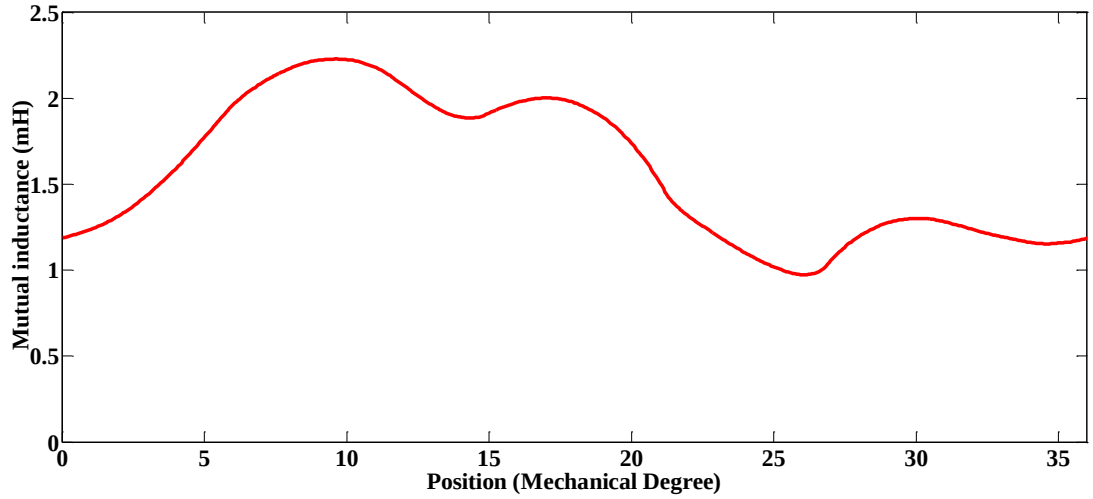

(b)

Fig. 4-10 (a) Self-inductance (b) mutual inductance of the proposed topology

Therefore, the objective function is set in proportion to specific torque as

$$F = \frac{1000 \cdot T_{avg}}{weight} \tag{4-10}$$

where, T_{avg} is the average torque of one phase for half an electric period, *weight* is composed of that of steel and copper and *1000* is the multiple for larger fitness value.

Some parameters, such as the outer diameter of stator, shaft diameter, stack active length and air-gap length are fixed as 382 mm, 100 mm, 74 mm and 0.5 mm,

respectively. Due to the difficulty of installing cooling system for in-wheel motors, the air cooling is selected. Hence, the current density is limited to about 5A/mm^2 and the slot fill factor is 0.46.

For GA optimization, the objective function should be set up at the beginning. T_{avg} is calculated according to the self-inductance variation with position. The value of self-inductance is a sum of individual inductances obtained from different flux lines in the EMC model. The magnetic flux lines at aligned and unaligned position are quite similar to those proposed in Chapter 3, which is calculated for a 6/16 two teeth topology. The only difference is that this topology should consider about the effect of PMs. The type of PMs is selected as N35SH, with the value of remanence B_r 1.2T. The quantity of magnetic flux produced by PMs is distributed in the airgap and stator pole. The value of them can be obtained from FEM at the aligned and unaligned position, respectively. Then, those are added to the flux quantity calculation of the stator pole and airgap. And the thickness of PMs d, the rotor inner diameter D_{r1}, rotor pole height h_r, stator inner diameter D_{s1}, stator teeth arc angle θ_s, slot depth in the stator pole h_{s1}, rotor pole arc angle θ_r and the parameters of l_1, l_2 and α are set as the variable to be optimized.

Moreover, some constraints need to be considered. There are also some linear and nonlinear inequalities as constraints for structures. The thickness of stator and rotor back iron should be more than one-half of the stator pole width and less than the stator pole width. Also, the slot area should be large enough to accommodate the number of winding turns. In addition, to avoid high saturation in the stator pole causing large

torque ripple, a minimum restriction of the width of stator pole is required.

The parameters of GA optimization are shown as follows: the population number is 50, the maximum generation number is 15, the crossover probability is 0.8 and the mutation is 0.06. The design flowchart of the GA procedure can be obtained from Fig. 4-11. And the average and the best fitness value during the optimization are shown in Fig. 4-12. A comparison of initial and final design can be found in Table 4-1. It is obvious that the optimization method can improve the specific torque by 22%.

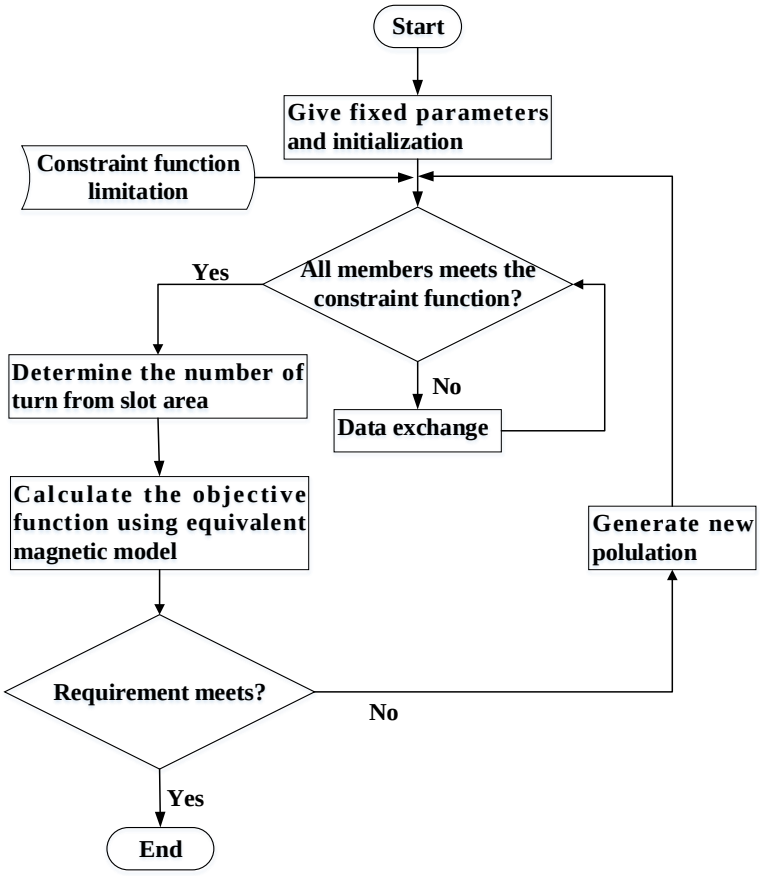

Fig. 4-11 Design flowchart of GA procedure

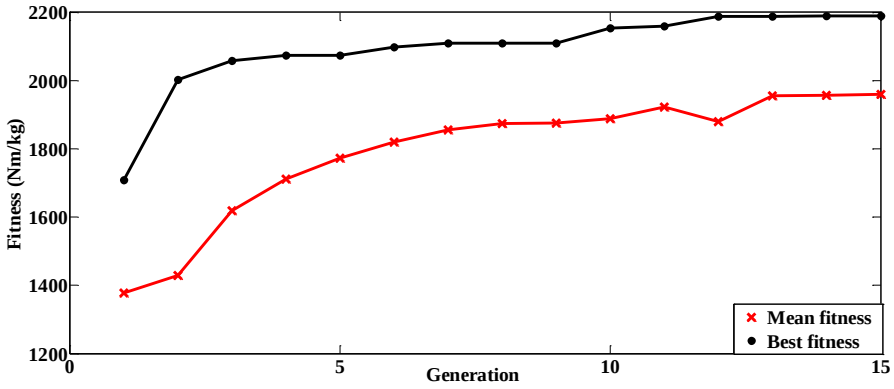

Fig. 4-12 Fitness value during GA optimization

Table 4-1
Comparison between Initial and Final Design

Parameter	Initial	Final
Stator teeth arc angle θ_s(°)	14.0	15.0
Rotor pole arc angle θ_r(°)	17.0	15.5
Number of winding turns per phase N	110	134
Stator inner diameter D_{s1}(mm)	172	182
Rotor inner diameter D_{r1}(mm)	267	277
Thickness of PMs d (mm)	10	10
Stator pole inner slot depth h_{s1} (mm)	5.0	9.5
l_1 (mm)	6.7	8.0
l_2 (mm)	18.1	23.0
α(°)	35	30
Output torque (Nm)	115	140
Specific torque (Nm/kg)	2.08	2.53

4.4 Performance Analysis & Comparison

2D-FEM is utilized to analyze the electromagnetic torque, core loss, copper loss and flux distribution of the optimized topology. Both static torque characteristics for one phase and torque produced with full phase conducting considering the commutation are computed.

To display the advantage of the proposed topology in torque output, a 6/4 and 12/8 three phase in-wheel SRMs under the same design criteria of the motor frame are also analyzed for comparison. The three motors have a common rotor outer diameter of 382 mm, stack length of 74 mm, airgap of 0.5mm.

To make the comparison fair and persuasive, the two conventional motors are optimized using GA method as well. The fitness function is proportional to specific torque with similar constraints as the proposed one. The optimized design parameters of the proposed motor are listed in Table 4-2.

Table 4-2
Geometric Parameters of Three SRMs

SRM Configuration	6/4	12/8	6/10 with PMs
Stator pole/teeth arc angle (°)	27.0	14.0	15.0
Rotor pole arc angle (°)	32.0	16.0	15.5
Number of winding turns per phase	182	192	134
Copper wire diameter (mm)	1.12	1.12	1.12
Number of parallel windings	6	6	6
Slot fill factor	0.46	0.46	0.46

Taking temperature effect into account, all three motors are running under equal current density condition with reasonable magnetic flux densities in the silicon steel for the sake of stability and avoiding high temperature demagnetization for PMs.

The analysis of the torque performance is based on 2D-FEM computation. Fig. 4-13 and Fig. 4-14 demonstrate the comparison of static torque characteristics and the torque produced with full phase conducting and commutation consideration, respectively. The detailed performance data of the three motors can be obtained from Table 4-3. It is clear that the proposed motor generates higher torque compared with the conventional counterparts. The torque waveforms of full phase conducting give a quantitative numerical analysis which indicates that the output torque of the proposed topology is 49% higher than that of 6/4 and 12/8 SRMs under the equal loss consideration. Furthermore, the novel motor has the highest specific torque among the three for its application to EVs.

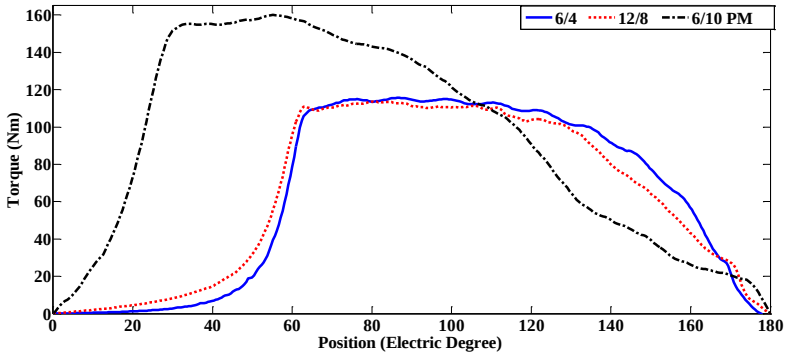

Fig. 4-13 Phase torque waveforms of three motors

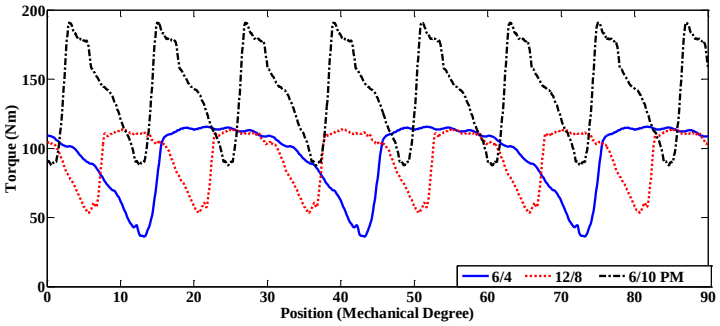

Fig. 4-14 Full phase torque waveforms of three SRMs

Table 4-3
Performance Comparison between Three SRMs

SRM Configuration	6/4	12/8	6/10 with PMs
Current density (A/mm^2)	5	5	5
Rated speed (rpm)	1000	1000	1000
Copper weight (kg)	11.52	8.23	8.32
Iron weight (kg)	47.21	40.43	46.40
PM weight (kg)	-	-	0.58
Total weight (kg)	58.73	48.66	55.30
Steel iron loss (W)	28	53	75
Copper loss (W)	670	478	482
PM loss (W)	-	-	9.6
Mechanical loss (W)	72	72	72
Stray loss (W)	54	42	45
Total Loss (W)	824	645	683.6
Torque (Nm)	94	94	140
Efficiency (%)	91.6	93.4	95.3
Torque per weight (Nm/kg)	1.60	1.93	2.53

In addition, when all the three motors under the same torque of 94 Nm, the performance data can be obtained from Table 4-4. It indicates that under the same load condition, the proposed topology is able to exhibit higher efficiency and suitable torque ripple compared with conventional counterparts.

Table 4-4
Performance Comparison with the Same Load

SRM Configuration	6/4	12/8	6/10 with PMs
Current density (A/mm^2)	5	5	3.47
Torque (Nm)	94	94	94.4
Torque ripple (%)	84.5	64.1	64.2
Efficiency (%)	91.6	93.4	95.7

4.5 Summary

This chapter proposes a novel hybrid reluctance motor incorporating the idea of adding PMs between adjacent stator poles and multi-tooth per stator pole with almost zero cogging torque. It takes the advantages of two teeth topology to provide enough torque output and PMs to weaken the magnetic flux saturation in the stator pole to increase the average torque and decline the torque ripple. The properties of the motor, including magnetic flux distribution, inductance, magnetic flux density, torque and loss, are calculated and analyzed by using 2D-FEM. GA method is utilized to optimize the parameters of the topology. The result shows that the novel motor has the ability to provide higher torque output with equal loss and lighter weight compared with

conventional counterparts. Moreover, the number of rotor poles is acceptable, highly suitable for common position sensors. Therefore, it has vast potential for future development in EVs.

In the next chapter, a prototype with a smaller size and an outer stator structure is constructed for the test of this topology. The outer diameter of the stator is selected as 120 mm, along with the stack length set as 85 mm. The speed of the motor can reach 960r/min with DC voltage 180V to achieve 730W power output.

Chapter 5

Experimental Performance of a Novel Hybrid Reluctance Motor

A motor with a smaller size and the same working principle of the hybrid reluctance topology is manufactured for high torque density experimental verification. The motor is an outer stator and inner rotor topology to enable easier manufacturing. Besides, a motor system is set up to verify the performance of the proposed topology. The characteristics of the motor are analyzed by utilizing FEM and confirmed by the experimental results. The analysis and experiment together demonstrate that the topology proposed in Chapter 4 will enhance the torque output, power density and efficiency.

5.1 Prototype & Simulation Analysis of the Motor

The prototype of the motor is an outer stator structure, along with the values of the fixed geometric parameters: stator outer diameter 120 mm, stack length 85 mm, shaft diameter 25 mm and airgap 0.3 mm. Other parameters are selected according to the optimization method combined by GA, 2D-FEM and EMC model mentioned in Chapter 4. The final optimized motor parameters are listed below in Table 5-1.

Table 5-1
Optimized Motor Parameters

Parameter	Optimized
Stator teeth arc angle θ_s(°)	15.0
Rotor pole arc angle θ_r(°)	15.5
Number of winding turns per phase N	140
Stator inner diameter D_{s1}(mm)	64
Rotor inner diameter D_{r1}(mm)	46
Thickness of PMs d (mm)	3
Length of PMs l (mm)	5
Thickness of stator yoke b_s (mm)	9
Stator pole inner slot depth h_{s1} (mm)	3.5
l_1 (mm)	2.76
l_2 (mm)	10.84
α(°)	57

The winding configuration is implemented with five parallel wires whose conductor diameter is 0.52 mm, 0.55 mm, 0.57 mm, 0.58 mm and 0.60 mm, respectively,

accumulating a total cross section area of 1.27 mm^2. For the concentrated winding, the slot fill factor is selected as 0.4. Besides, the steel type is chosen as DW470. The model setup on the basis of Ansoft Maxwell can be obtained from Fig. 5-1.

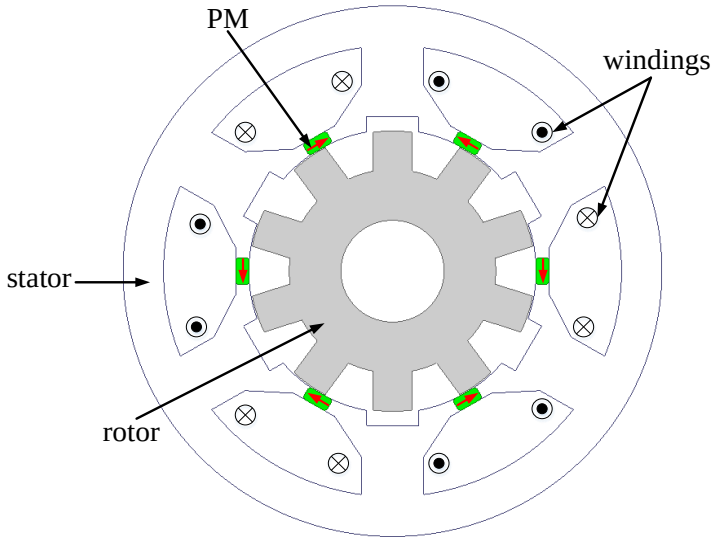

Fig. 5-1 Model of the proposed topology based on Maxwell

The red arrow represents the direction of the magnetic excitation of PMs. Besides, the fork and point mark inside the windings stand for current flowing in and out, respectively. The static torque performance with the current density 5.5A/mm^2 and each phase conducting for half an electric period is shown in Fig. 5-2.

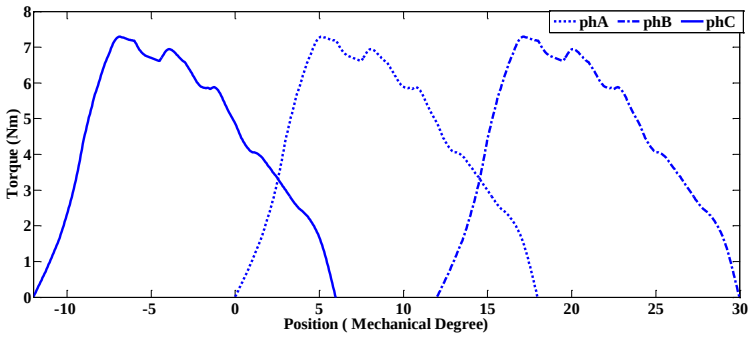

Fig. 5-2 Static torque performance of the proposed topology

Moreover, the performance comparison with a 12/8 SRM shown in Fig. 5-3 of the same dimension is demonstrated in Table 5-2 by utilizing FEM.

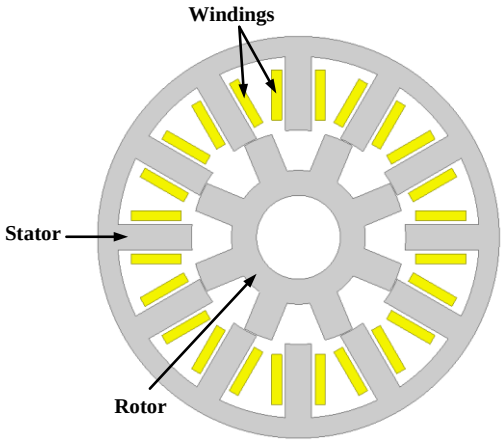

Fig. 5-3 Prototype of 12/8 SRM

Table 5-2 Comparison with 12/8 SRM by Utilizing FEM

Motor configuration	12/8 SRM	Proposed Motor
Stator outer diameter (mm)	120	120
Stack length (mm)	85	85
Airgap length (mm)	0.3	0.3
Number of turns per phase	208	140
Slot fill factor	0.4	0.4
Current density (A/mm^2)	5.5	5.5
Average Torque (Nm) (FEM)	4.49	7.40
Copper loss (W)	103.95	82.8
Core loss (W)	18.6	35.6
PM loss (W)	-	0.12
Mechanical loss (W)	4.99	4.99
Stray loss (W)	8.93	8.64
Output Power (W)	470	775
Efficiency (%)	77.5	85.4

5.2 Motor System Set up

5.2.1 Mechanical Structure of the Platform

The mechanical structures of the motor and platform are developed by the software Solidworks 2012 for manufacturing purpose. The models of the stator, rotor and platform are shown below in Fig. 5-4 (a), (b) and (c), respectively.

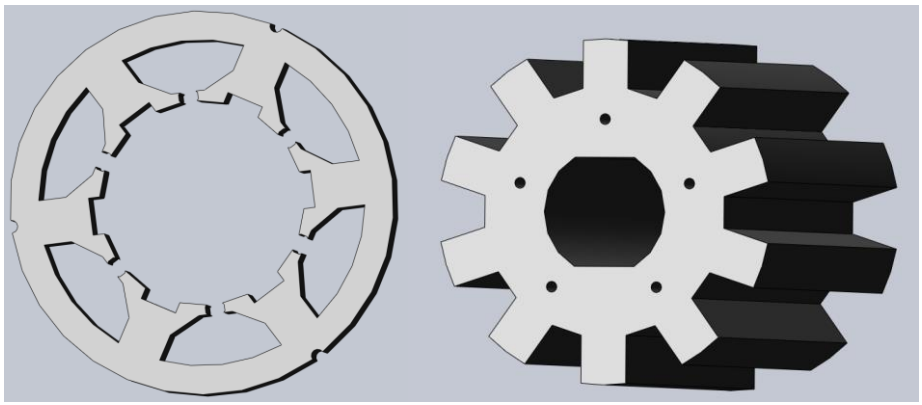

(a) (b)

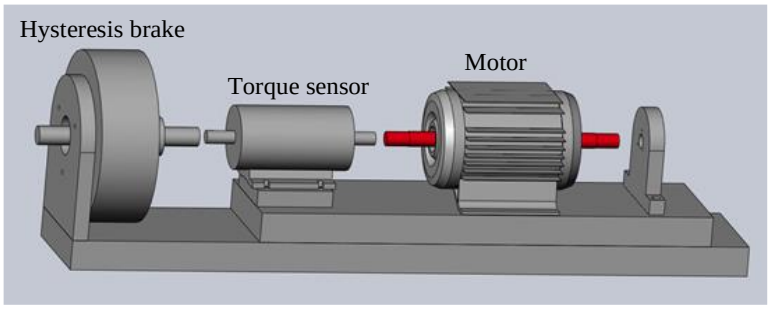

(c)

Fig. 5-4 Mechanical structure of (a) stator (b) rotor (c) platform

5.2.2 Experimental Platform Set up

The manufactured version of the stator, rotor and windings can be found in Fig. 5-5

(a), (b) and (c), respectively.

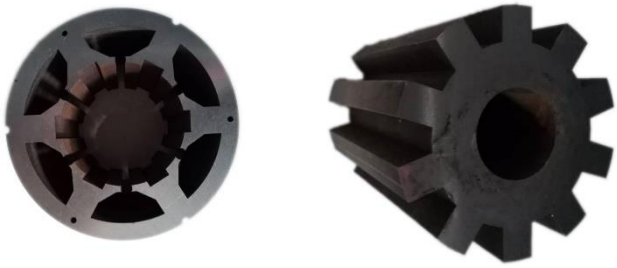

(a) (b)

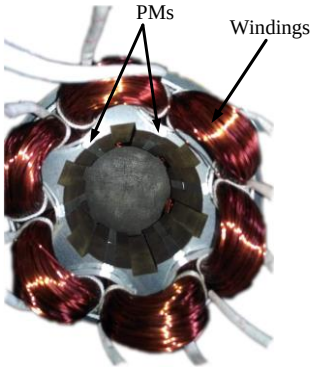

(c)

Fig. 5-5 Prototype of (a) stator (b) rotor (c) winding configuration of the motor

Moreover, the platform is set up as follows in Fig. 5-6, in which DSPACE DS1104 is utilized as the control board.

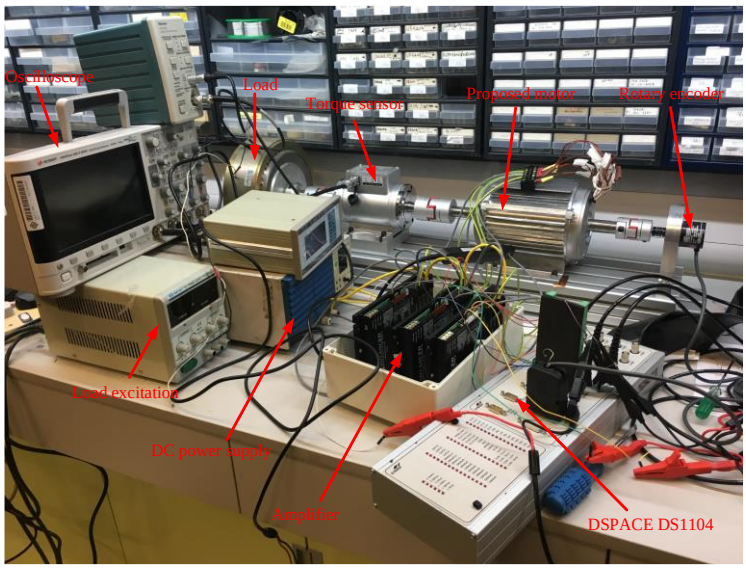

Fig. 5-6 Experimental motor system set up

5.3 Static Performance of the Motor

The static torque characteristic of the proposed motor is measured by experimental method. The result is compared with that of 2-D FEM simulation by using Ansoft Maxwell, along with the value of the excitation current for testing varies from 2A to 10A. Besides, the position covers half an electric period from the unaligned position to the fully aligned one. The results and comparison can be obtained from Fig. 5-7. The figure illustrates that most testing points correspond with the FEM simulation within an error of 10% with only some individual ones deviating from the expected due to the manufacturing and measurement errors.

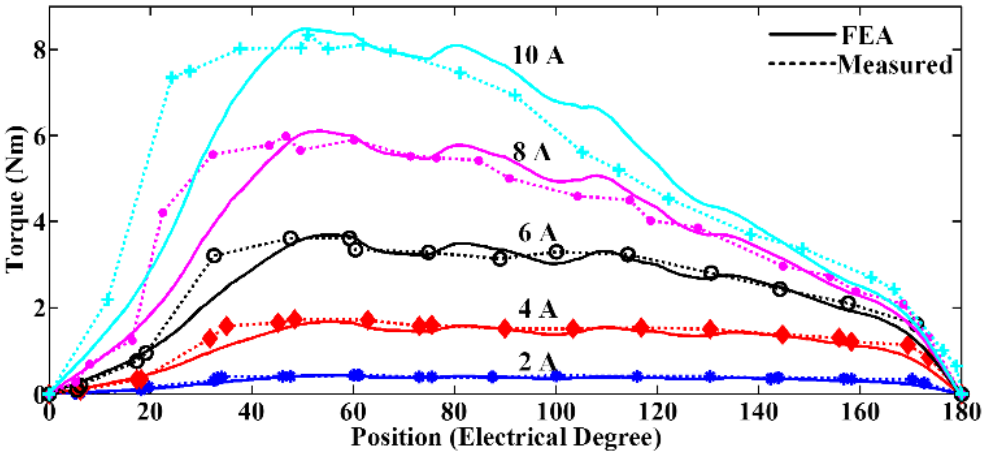

Fig. 5-7 Measured & FEA comparison of static torque performance

5.4 Dynamic Performance Analysis of the Proposed Motor

The motor is controlled by the board DSPACE DS1104, with an asymmetric bridge structure of the power converter for driving. Besides, the line number of the rotary encoder is 2000 and four folded by the control board to limit the maximal position error within 0.045 degree. Moreover, the voltage value provided by the DC power

supply is 180V. The block diagram of the control strategy is shown below in Fig. 5-8.

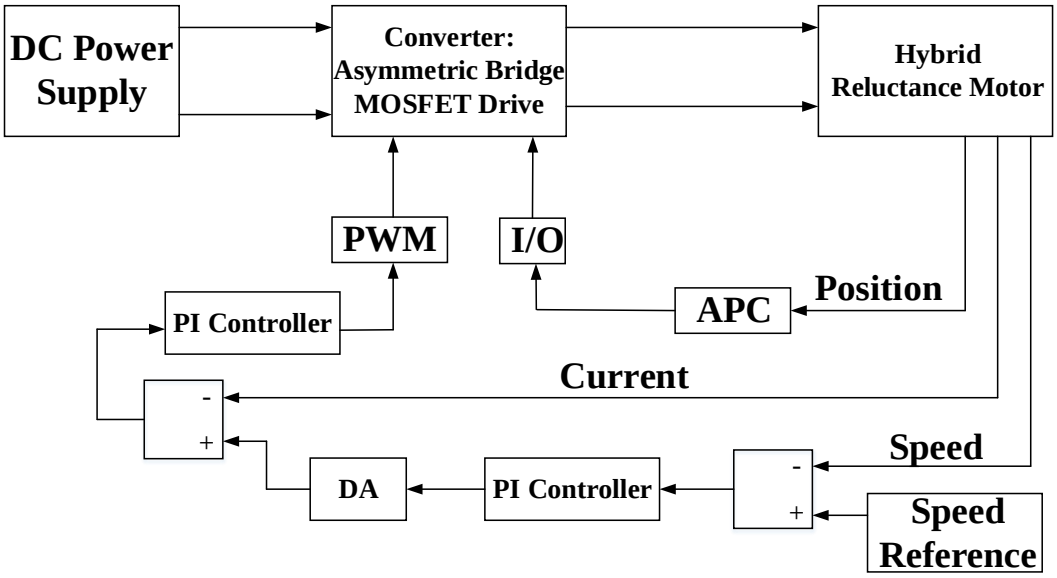

Fig. 5-8 Block diagram of the control strategy

The control method of the proposed motor is dual-closed-loop control with the outer loop of speed and inner loop of current. The transistors are selected as MOSFET to control the current value in the windings. In addition, APC stands for angle position control to define the switching on and off angles of the MOSFET.

For better operation and higher torque output of the topology, the switching on angle is set as -0.5 degree while the switching off angle is selected as 15 degree for phase A, where the fully aligned position of phase A is defined as the zero position. The rated speed of the motor is 960r/min. Through experimental analysis, the output torque can reach 7.3 Nm with the current density 5.5A/mm^2.The data are collected in Table 5-2.

Table 5-3
Motor Performance Data

Parameter	Optimized
Number of winding turns per phase N	140
Total cross-section area of each turn (mm^2)	1.27
Current density (A/mm^2)	5.5
Stator outer diameter D_{s2} (mm)	120
Stack length l (mm)	85
Airgap length (mm)	0.3
Rated speed (rpm)	960
Rated torque (Nm)	7.3
Rated power (W)	730

The FEM simulation of transient torque and measured average torque (because of the working principle of the torque sensor, transient torque cannot be acquired) at the rated speed can be obtained from Fig. 5-9. The current injected into the windings for FEM simulation is in the shape of square waveforms with each phase conducting half an electric period. The average torque value of the experimental result agrees well with that of the simulation which is 7.35 Nm. Furthermore, the current waveform of three phase full load current at the speed of 500 rpm is demonstrated in Fig. 5-10

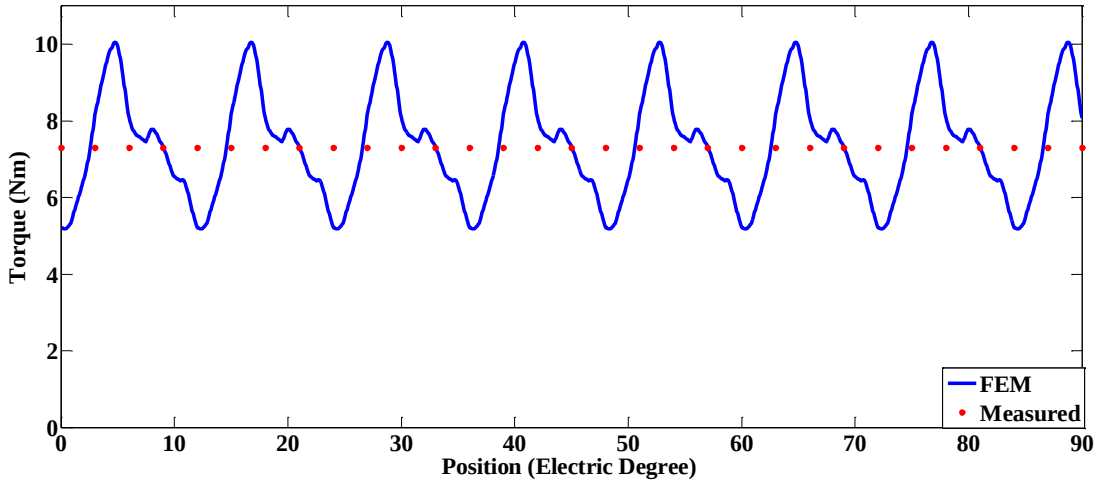

Fig. 5-9 Measured & simulated transient torque characteristic

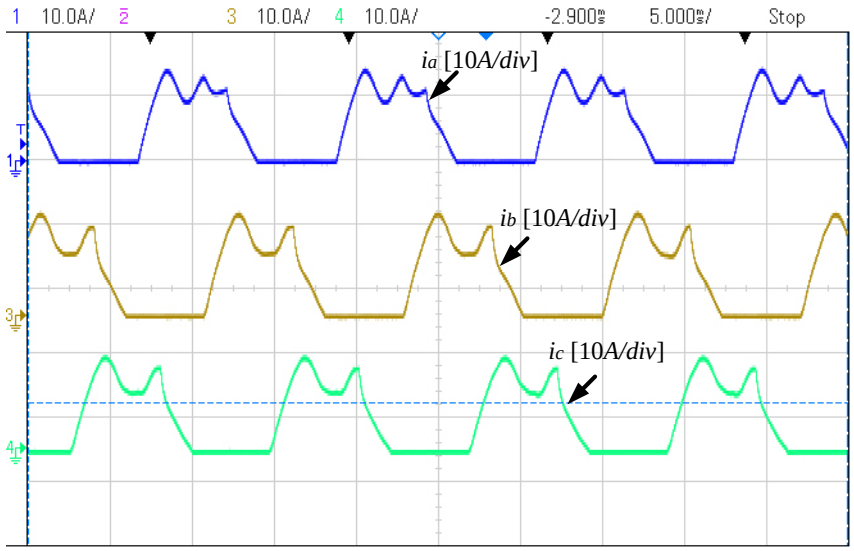

Fig. 5-10 Measured three phase current waveform of the motor

Then, the torque and speed characteristic can be measured for the proposed motor with the result shown in Fig. 5-11. The rated speed can reach 960 r/min with the torque output almost 7.3 Nm. Moreover, the maximal power output for this machine is 734 W as shown in Fig. 5-12 under various speed conditions.

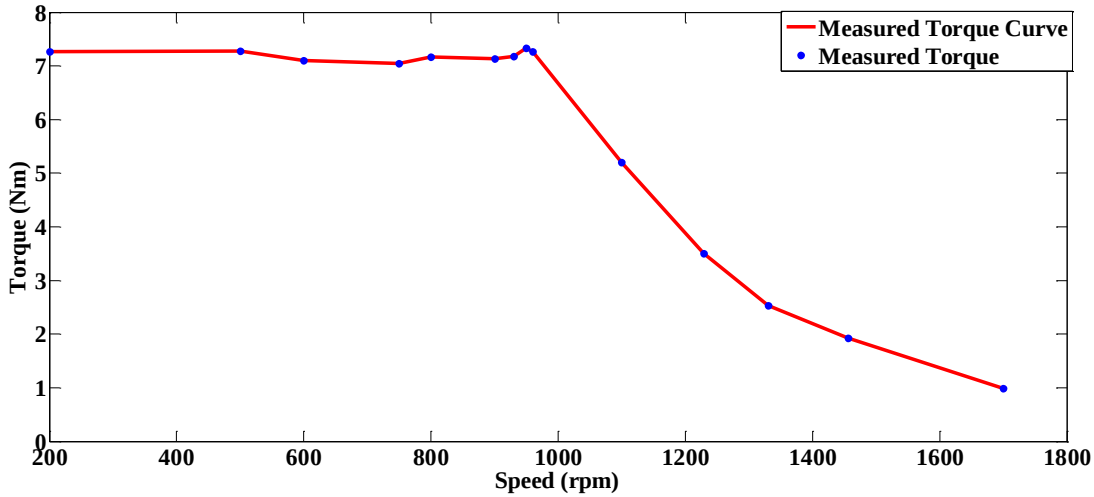

Fig. 5-11 Torque versus speed characteristic of the motor

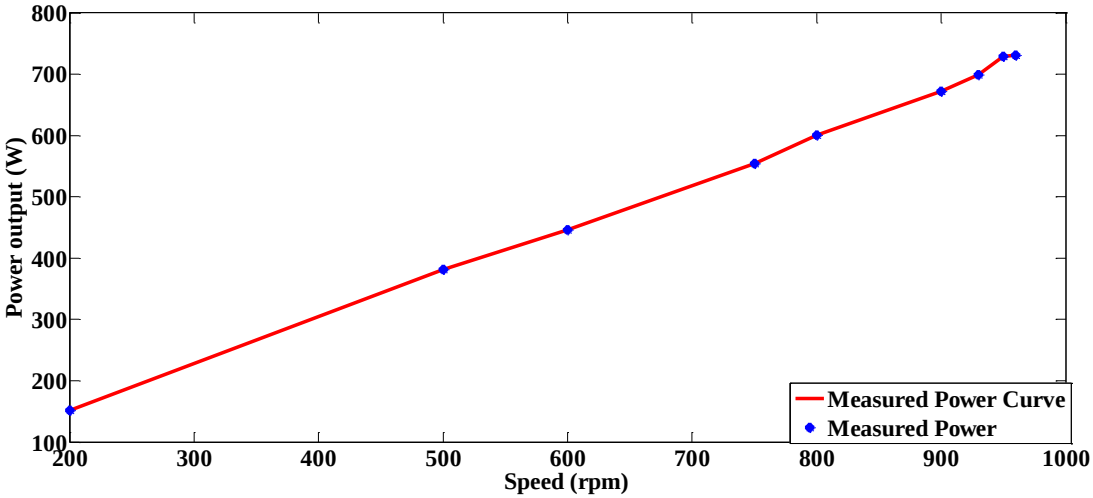

Fig. 5-12 Output power of the motor

The experimental phase current and average torque waveform in low, middle and high speed mode is shown in Fig. 5-13 (a), (b) and (c), respectively. The value of the speed is selected as 220r/min, 960r/min and 1200r/min, respectively.

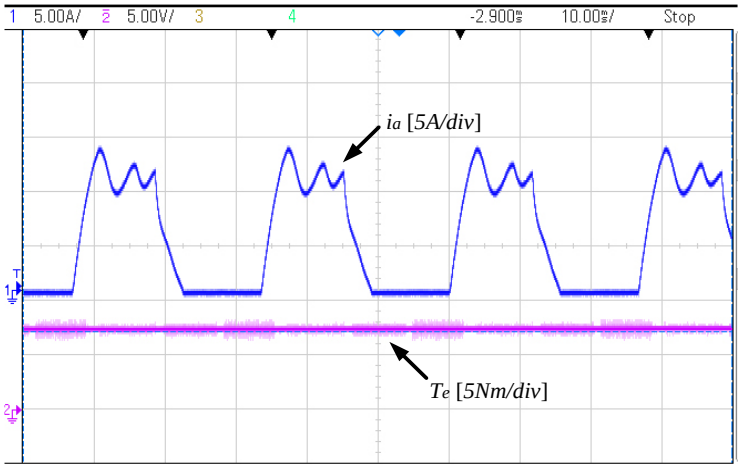

(a)

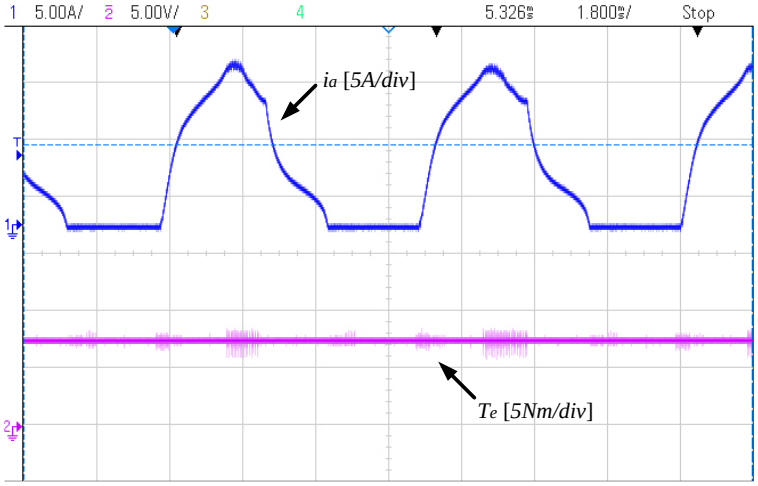

(b)

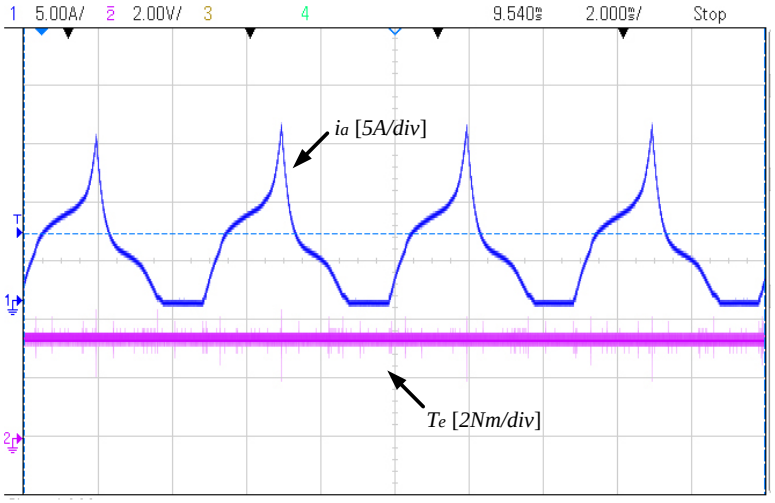

(c)

Fig. 5-13 Phase current & torque waveform with the speed of (a) 220r/min (b)

960r/min (c) 1200r/min

Also, the efficiency of the motor at the rated speed 960 rpm is evaluated through experimental method. The efficiency equation is expressed as,

$$\eta = \frac{P_{out}}{P_{in}} \cdot 100\% \tag{5-1}$$

where, P_{out} is the motor output power and is illustrated as,

$$P_{out} = T_e \cdot \omega \tag{5-2}$$

and P_{in} is the motor input power and demonstrated as,

$$P_{in} = n \cdot \frac{1}{T} \sum ui \cdot \Delta t \tag{5-3}$$

where, n is the number of phases, u is transient voltage added to each phase and i is the transient phase current. By inserting (5-2) and (5-3) into (5-1), the efficiency equation can be transferred to

$$\eta = \frac{T_e \cdot \omega}{n \cdot \frac{1}{T} \sum ui \cdot \Delta t} \cdot 100\% \tag{5-4}$$

Phase A is selected to calculate the motor input power and efficiency. The measured data and waveform can be obtained from Fig. 5-14 in which the M channel is the calculation result of the input power of Phase A.

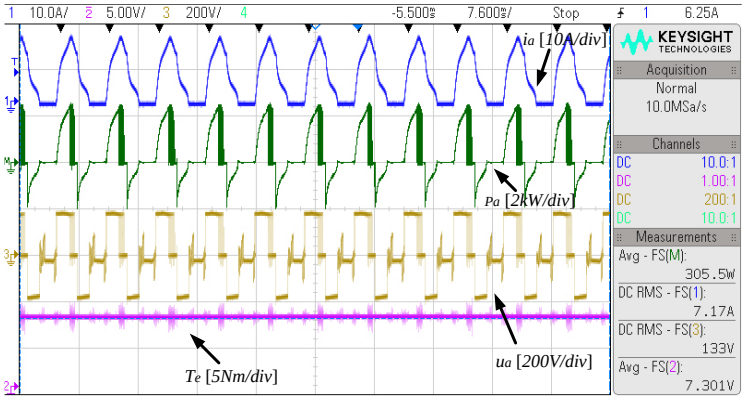

Fig. 5-14 Measured waveform related to efficiency calculation

Therefore, the measured results illustrate that the efficiency of the proposed motor at the rated speed is 81% much higher than the induction motor of the same size which only has an efficiency of 65% [107]. Furthermore, the output power of the topology is 730W, still much higher than that of an induction motor with the same physical volume of frame which can output 550W. The detailed comparison can be obtained from Table 5-4.

Table 5-4 Comparison with IM by Experiment

Motor configuration	IM [107]	Proposed Motor
Stator outer diameter (mm)	120	120
Stack length (mm)	85	85
Airgap length (mm)	0.25	0.3
Number of stator/rotor slot	24/22	6/10
Current density (A/mm^2)	7.9	5.5
Average Torque (Nm) (Measured)	5.47	7.30
Speed (rpm)	960	960
Output Power (W)	550	734
Efficiency (%)	65	81
Voltage (V)	Three-phase 220AC	180DC

5.5 Summary

A hybrid reluctance motor with the same operating principle as that mentioned in Chapter 4, but with a smaller size and inner rotor structure is further developed in this

chapter. At the beginning, mechanical design and experiment platform setup are implemented. Then, the static performance of the motor is measured and compared with FEM simulation results. Moreover, the assessment of the motor transient performance is done to verify its characteristics. The test motor can reach the rated speed of 960 r/min and output 730W power. Finally, the experimental results correspond quite well with the FEA simulation. The proposed topology achieves high torque output, high power density and good efficiency.

Chapter 6

Conclusion and Future Work

In the whole thesis, the SRM is introduced to the application of EVs. The design, optimization and performance analysis of two topologies of enhanced torque motors based on SRM working principle are carried out in Chapter 3 and Chapter 4, respectively. A motor with the same working principle of the topology proposed in Chapter 4, but with a smaller size is manufactured for experimental verification in Chapter 5. The experimental results correspond quite well with FEA to confirm the torque and power improvement. This chapter makes a conclusion of all the contributions of the thesis and suggestions for future research work.

6.1 Contributions & Achievements

A. The electric motors applied to EVs have been reported to be various types that include the brushed and brushless DC motor, induction motor and permanent magnetic motor. However, the superior features of the switched reluctance motor over other kinds of motors are simple, robust structure, low cost and better fault tolerance. Therefore, it presents a good prospect for EV applications.

B. Two special types of SRMs are discussed. One type is the SRM with more rotor poles than stator poles. The other is that with multiple teeth per stator pole. These two types are analyzed for torque improvement.

C. A novel enhanced torque density in-wheel SRM is proposed. It combines the idea of multi-teeth per stator pole and more rotor poles than stator teeth together. The magnetic principle of the proposed topology is analyzed initially. Then, the structure determination is made, including number of teeth per stator pole, number of rotor poles and number of phases. Moreover, the motor topology is optimized by GA and EMC model. In addition, the performance of the motor is analyzed by FEM and compared with SRMs with more rotor poles than stator poles to verify its advantages.

D. The topology of a new hybrid reluctance motor by inserting permanent magnets between adjacent stator poles of a multi-teeth SRM is put forward. The motor is an in-wheel version and operated based on the switched reluctance principle. Also, the structural analysis is carried out to determine the shape of stator pole by using FEM. Then, the EMC model is utilized to analyze the effect of torque improvement and the result is confirmed by FEM. Furthermore, the optimization process is based on GA for

the purpose of maximal specific torque. Finally, the torque performance and energy loss of the topology are calculated and compared with its conventional counterparts to show its dominance.

E. A hybrid reluctance motor with the same working principle as mentioned before, but of a smaller size and outer stator structure is manufactured to verify its torque and power enhancement. The analysis includes static and transient performances, along with the comparison with those analyzed by utilizing FEM. The comparison demonstrates that the experimental results agree quite well with those of the simulation. Therefore, the torque and power density improvement is demonstrated.

6.2 Suggestions for Future Research

As mentioned before, better control and optimization strategies need to be considered about for the proposed hybrid reluctance motor to achieve higher efficiency and better performance. The suggestions are put forward as follows:

(1) The control method of high speed operation needs to be changed to angle position control to keep the output power constant to enhance its dynamic performance. In the future work, control methods to optimize the performance of motor under different speed conditions are about to be proposed and analyzed.

(2) Although the experimental results have proved that the proposed hybrid reluctance motor is able to improve the power and torque density with a suitable turn on and off angle, a more optimized switch on and off angle may be possible to increase the torque output further. Therefore, substantial research work need to be conducted on that.

(3) The application of PMs inserted into two-teeth SRM is able to reduce the magnetic saturation in the stator pole, thus reducing the output torque ripple. The reluctance motor, however, has a feature of high torque ripple. As a consequence, some novel control methods to weaken the torque ripple of the proposed motor need to be further studied.

(4) Due to the high cost, speed limit and increased axial length introduced by position sensor, sensorless control has its potential application in low cost, low volume and high speed situation. Hence, some frontier control methods, including model predictive control (MPC), can be explored for deeper research.

Appendices

A. GA optimization MATLAB code for the motor in Chapter 3:

Main Function:

```
function Tw=a3(pop)
    Dr1=pop(1);
    hr=pop(2);
    Ds1=pop(3);
    seitas1=pop(4);
    hs1=pop(5);
    betar=pop(6);
miu0=4*pi*10^(-7);
Dr2=382*10^(-3);
Dsh=100*10^(-3);
lg=0.5*10^(-3);
Ds2=Dr1-2*lg;
l=74*10^(-3);
br=(Dr2-Dr1)/2-hr;
hs=(Ds2-Ds1)/2;
I=23;
rou=0.0217
bs=(Ds1-Dsh)/2;
```

```
gama=asin(Ds2*sin(seitas1/2)/Ds1)-seitas1/2;
slot=(37.5/180*pi-seitas1)/2*(Ds2/2)^2-(37.5/180*pi-seitas1-2*gama)/2*(Ds1/2)^2-
Ds2/2*Ds1/2*sin(gama);
N=slot/(2209.18e-6)*122;
N=ceil(N);
if mod(N,2)==1
    N=N+1;
end
Lu1=flux1(miu0,Dr1,Dr2,Ds1,Ds2,Dsh,seitas1,hs1,lg,l,betar,br,hs,N,I,bs,hr);
Lu2=flux2(miu0,Dr1,Dr2,Ds1,Ds2,Dsh,seitas1,hs1,lg,l,betar,br,hs,N,I,bs,hr);
Lu3=flux3(miu0,Dr1,Dr2,Ds1,Ds2,Dsh,seitas1,hs1,lg,l,betar,br,hs,N,I,bs,hr);
Lu4=flux4(miu0,Dr1,Dr2,Ds1,Ds2,Dsh,seitas1,hs1,lg,l,betar,br,hs,N,I,bs,hr);
Lu5=flux5(miu0,Dr1,Dr2,Ds1,Ds2,Dsh,seitas1,hs1,lg,l,betar,br,hs,N,I,bs,hr);
Lu6=flux6(miu0,Dr1,Dr2,Ds1,Ds2,Dsh,seitas1,hs1,lg,l,betar,br,hs,N,I,bs,hr);
Lu7=flux7(miu0,Dr1,Dr2,Ds1,Ds2,Dsh,seitas1,hs1,lg,l,betar,br,hs,N,I,bs,hr);
Lu8=flux8(miu0,Dr1,Dr2,Ds1,Ds2,Dsh,seitas1,hs1,lg,l,betar,br,hs,N,I,bs,hr);
Lu9=flux9(miu0,Dr1,Dr2,Ds1,Ds2,Dsh,seitas1,hs1,lg,l,betar,br,hs,N,I,bs,hr);
Lu10=flux10(miu0,Dr1,Dr2,Ds1,Ds2,Dsh,seitas1,hs1,lg,l,betar,br,hs,N,I,bs,hr);
Lu11=flux11(miu0,Dr1,Dr2,Ds1,Ds2,Dsh,seitas1,hs1,lg,l,betar,br,hs,N,I,bs,hr);
Lu12=flux12(miu0,Dr1,Dr2,Ds1,Ds2,Dsh,seitas1,hs1,lg,l,betar,br,hs,N,I,bs,hr);
Lu13 = flux13( miu0,Dr1,Dr2,Ds1,Ds2,Dsh,seitas1,hs1,lg,l,betar,br,hs,N,I,bs,hr );
Lu=Lu1+Lu2+Lu3+Lu4+Lu5+Lu6+Lu7+Lu8+Lu9+Lu10+Lu11+Lu12+Lu13;
```

```
La1=aflux1(miu0,Dr1,Dr2,Ds1,Ds2,Dsh,seitas1,hs1,lg,l,betar,br,hs,N,I,bs,hr);

La2=aflux2(miu0,Dr1,Dr2,Ds1,Ds2,Dsh,seitas1,hs1,lg,l,betar,br,hs,N,I,bs,hr);

La=La1+La2;

L=Lu-La;

T=0.5*L*I^2;

l1=Ds2*sin(11.25*pi/180-seitas1/2);

h1=hs1-Ds2/2+Ds2/2*cos(11.25*pi/180-seitas1/2);

l2=l1-2*h1*tan(11.25*pi/180);

S3=(l1+l2)*h1/2+(pi/16-seitas1/2)*(Ds2/2)^2-0.5*(Ds2/2)^2*sin(pi/8-seitas1);

V1=(pi*(Ds2/2)^2-6*slot-6*S3-pi*(Dsh/2)^2)*l;

V2=(pi*(Dr2/2)^2-pi*(Dr2/2-br)^2+16*betar*Dr1/2*hr)*l;

weight1=7.8e3*(V1+V2);

weight2=pi*0.56^2*8*N*378.73*3*8.9e-6;

weight=weight1+weight2;

loss=1.5*I^2*0.0217*(74+(Ds2/4+Ds1/4)*(pi/8+seitas1)+Ds1*sin(pi/6-pi/16)-

seitas1*Ds2/2)*2*1e-3/(pi*0.56^2*8)*N;

Tw=T/(pi/10)/weight+ T/(pi/10)/loss+1000

end
```

B. GA optimization MATLAB code for the motor in Chapter 4:

Main Function:

```
function Tw=main3(pop)

miu0=4*pi*10^(-7);
```

```
Dr1=pop(1);

lg=0.5*10^(-3);

Dr2=382*10^(-3);

Ds2=Dr1-2*lg;

Dsh=100*10^(-3);

hr=pop(2);

Ds1=pop(3);

seitas1=pop(4);

betar=pop(5);

hs1=4.9*10^(-3);

l=74*10^(-3);

br=(Dr2-Dr1)/2-hr;

hs=(Ds2-Ds1)/2;

I=23.3;

bs=(Ds1-Dsh)/2;

lpm=10*10^(-3);

l1=pop(6);

l2=pop(7);

arfar=pop(8);

r2=Ds2/2*cos(18*pi/180+seitas1/2)-lpm*cos(18*pi/180)+l1*sin(pi/6)-l2*sin(arfar);

r1=Ds2/2*sin(18*pi/180+seitas1/2)-lpm*sin(18*pi/180)-l1*cos(pi/6)-l2*cos(arfar);

l3=r2-sqrt((Ds1/2)^2-r1^2);
```

```
peseiFe=0.207;
peseiAir=0.032;
peseiTotal=0.239;
S1=r1*l;
seita1=seitas1*Ds2/(2*Ds2-4*hs1);
seita2=pi/10-seita1;
S2=seitas1*Dr1/2*l+hs1*l+seita2*(Ds2/2-hs1)*l;
slot=(Ds2*sin(12*pi/180-seitas1/2)-2*lpm*sin(12*pi/180)+2*l1+2*l2*sin(pi/3-
arfar)-l3*sin(pi/6))*l3*cos(pi/6)+(Ds2*sin(12*pi/180-seitas1/2)-
2*lpm*sin(12*pi/180)+2*l1+l2*sin(pi/3-arfar))*l2*cos(pi/3-arfar)-(pi/6-
asin(2*r1/Ds1))*(Ds1/2)^2+0.5*(Ds1/2)^2*sin(pi/3-2*asin(2*r1/Ds1));
N=slot/(1397e-6)*110;
N=ceil(N);
if mod(N,2)==1
    N=N+1;
end
Lu1=uflux1(miu0,Dr1,Dr2,Ds1,Ds2,Dsh,seitas1,hs1,lg,l,betar,br,hs,N,I,bs,hr,lpm,l1,l
2,l3,peseiFe,peseiAir,peseiTotal,S1,S2,r1,r2,arfar);
Lu2=uflux2(miu0,Dr1,Dr2,Ds1,Ds2,Dsh,seitas1,hs1,lg,l,betar,br,hs,N,I,bs,hr,lpm,l1,l
2,l3,peseiFe,peseiAir,peseiTotal,S1,S2,r1,r2,arfar);
Lu3=uflux3(miu0,Dr1,Dr2,Ds1,Ds2,Dsh,seitas1,hs1,lg,l,betar,br,hs,N,I,bs,hr,lpm,l1,l
2,l3,peseiFe,peseiAir,peseiTotal,S1,S2,r1,r2,arfar);
```

```
Lu4=uflux4(miu0,Dr1,Dr2,Ds1,Ds2,Dsh,seitas1,hs1,lg,l,betar,br,hs,N,I,bs,hr,lpm,l1,l
2,l3,peseiFe,peseiAir,peseiTotal,S1,S2,r1,r2,arfar);
Lu6=uflux6(miu0,Dr1,Dr2,Ds1,Ds2,Dsh,seitas1,hs1,lg,l,betar,br,hs,N,I,bs,hr,lpm,l1,l
2,l3,peseiFe,peseiAir,peseiTotal,S1,S2,r1,r2,arfar);
Lu7=uflux7(miu0,Dr1,Dr2,Ds1,Ds2,Dsh,seitas1,hs1,lg,l,betar,br,hs,N,I,bs,hr,lpm,l1,l
2,l3,peseiFe,peseiAir,peseiTotal,S1,S2,r1,r2,arfar);
Lu8=uflux8(miu0,Dr1,Dr2,Ds1,Ds2,Dsh,seitas1,hs1,lg,l,betar,br,hs,N,I,bs,hr,lpm,l1,l
2,l3,peseiFe,peseiAir,peseiTotal,S1,S2,r1,r2,arfar);
Lu9=uflux9(miu0,Dr1,Dr2,Ds1,Ds2,Dsh,seitas1,hs1,lg,l,betar,br,hs,N,I,bs,hr,lpm,l1,l
2,l3,peseiFe,peseiAir,peseiTotal,S1,S2,r1,r2,arfar);
Lu=Lu1+Lu2+Lu3+Lu4+Lu6+Lu7+Lu8+Lu9;
peseiFe=0.043;
peseiAir=0.18135;
peseiTotal=0.22435;
La1=aflux1(miu0,Dr1,Dr2,Ds1,Ds2,Dsh,seitas1,hs1,lg,l,betar,br,hs,N,I,bs,hr,lpm,l1,l
2,l3,peseiFe,peseiAir,peseiTotal,S1,S2,r1,r2,arfar);
La2=aflux2(miu0,Dr1,Dr2,Ds1,Ds2,Dsh,seitas1,hs1,lg,l,betar,br,hs,N,I,bs,hr,lpm,l1,l
2,l3,peseiFe,peseiAir,peseiTotal,S1,S2,r1,r2,arfar);
La=La1+La2;
L=Lu-La;
T=0.5*L*I^2;
S3=(Ds2*sin(pi/10-seitas1/2)-7.585e-3*sin(pi/10))*7.585e-3*cos(pi/10)+(pi/10-
```

```
seitas1/2)*(Ds2/2)^2-(Ds2/2)^2*0.5*sin(pi/5-seitas1);

V1=(pi*(Ds2/2)^2-6*slot-6*S3-pi*(Dsh/2)^2)*l;

V2=(pi*(Dr2/2)^2-pi*(Dr2/2-br)^2+10*betar*Dr1/2*hr)*l;

weight1=7.8e3*(V1+V2);

weight2=pi*0.56^2*6*N*375.3*3*8.9e-6;

weight=weight1+weight2;

Tw=T/(pi/10)/weight+1000

end
```

References

[1] Mohamed O. Badawy and Yilmaz Sozer, “Power Flow Management of a Grid Tied PV-Battery System for Electric Vehicles Charging”, *IEEE Trans. Ind. Appl.* vol. 53, no. 2, pp. 1347-1357, 2017

[2] R. Schmidt, “Information technology energy usage and our planet,” in *11th Intersociety Conf. on Thermal and Thermomechanical Phenomena in Electronic Systems*, pp.1255-1275, 28-31 May 2008.

[3] Ruoyun Shi, Sepehr Semsar and Peter W. Lehn, “Constant Current Fast Charging of Electric Vehicles via DC Grid Using Dual Inverter Drive”, *IEEE Trans. on Ind. Electron.*, vol. 64, no. 9, pp. 6940-6949, 2017.

[4] Setright, L. J. K. (2004). *Drive On!: A Social History of the Motor Car*. Granta Books. ISBN 1-86207-698-7

[5] “Internal combustion engine”, Wikipedia, https://en.wikipedia.org/wiki/Internal_combustion_engine

[6] “Gasoline”, Wikipedia, https://en.wikipedia.org/wiki/Gasoline#Density

[7] Shiwei Wang and D. l. Yu, “An Application of Second-Order Sliding Mode Control for IC Engine Fuel Injection”, *2006 Canadian Conference on Electrical and Computer Engineering*, Ottawa, Ont., Canada, pp. 1035-1038, 2006.

[8] “Diesel Fuel”, Wikipedia, https://en.wikipedia.org/wiki/Diesel_fuel#Cars

[9] Nice Karim, “How Turbochargers Work”, 4 December 2000, Auto.howstuffworks.com

[10] Yu-Chao Wang, Shi-Xue Wang and Chuanshan Dai “A Theoretic Model of Thermoelectric Device Using Automobile Exhaust Gas for Power Generation”, *2012 Asia-Pacific Power and Energy Engineering Conference*, Shanghai, China.

[11] G. Venkatesh, “Power Production Technique Using Exhaust Gas From Present Automobiles via Convergent-Divergent Nozzle”, *2006 IEEE Conference on Electric and Hybrid Vehicles*, Pune, India.

[12] Zhang Xueyi, Wang Yujuan, Jia Liliang and Shi Liwei, "Structure Design and Finite-element Analysis of Rectification Tower of Refrigeration Making Use of Automobile Exhaust Gas Remaining Energy", *Proceedings 2011 International Conference on Transportation, Mechanical, and Electrical Engineering (TMEE)*, pp. 1181-1184.

[13] "Natural Gas", Wikipedia, https://en.wikipedia.org/wiki/Natural_gas#Transportation

[14] Muhammad Iram Baig and Taufeeq Elahi, "Accurate Measurement of Pressure in Natural Gas Vehicles: A Digital/Electronic Design and Fabrication", *2008 IEEE International Multitopic Conference*, Karachi, Pakistan, pp. 520-524, 2008.

[15] M. Orzechowska and D. Kryzia, " Estimation of the future demand for natural gas in road transport in Poland", *5th International Youth Conference on Energy (IYCE)*, Pisa, Italy, 2015.

[16] George Martinas, Ovidiu Sorin Cupsa, Nicolae Buzbuchi and Andreea Arsenie, "Modeling with Finite Volume the Combustion in Direct Injection Natural Gas Engine Using Non-Premixed Combustion Model", *Fifth International Conference on the Innovative Computing Technology (INTECH 2015)*, Pontevedra, Spain, 2015.

[17] Luo Yong and Yanfei Sui, "Risk Analysis for Explosion and Burning of Compressed Natural Gas (CNG) Station Vehicles Exclusively", *International Conference on Industrial Mechatronics and Automation*, Chengdu, China, pp. 113-116, 2009.

[18] Ma A. Seijo, A. Filgueira, E. Munoz and Ma M. Iglesias, "Viability study of the facilities for the provision of compressed natural gas (cng) to vehicles destined to the public transport", *International Conference on Clean Electrical Power*, Capri, Italy, pp. 662-665, 2007.

[19] "What is a Hybrid Vehicle?", What-is-what.com.

[20] " Hybrid Cars Technology Overviews", www. Green-vehicles.com

[21] Youngkwan Ko, Jeeho Lee and Hyeongcheol Lee, "A Supervisory Control Algorithm for a Series Hybrid Vehicle With Multiple Energy Sources", *IEEE Trans. Veh. Technol.*, vol. 64, no. 11, pp. 4942–4953, Nov. 2015.

[22] Thomas Miro-Padovani, Guillaume Colin, Ahmed Ketfi-Chérif and Yann Chamaillard, “Implementation of an Energy Management Strategy for Hybrid Electric Vehicles Including Drivability Constraints”, *IEEE Trans. Veh. Technol.*, vol. 65, no. 8, pp. 5918–5929, Aug. 2016.

[23] Andreas Gerlach, Niklas Förster, Hermann Rottengruber and Roberto Leidhold, “Efficient Control of Internal Combustion Engines for Electric Power Generation Without Throttle Actuator”, *IECON 2016 - 42nd Annual Conference of the IEEE Industrial Electronics Society*, Florence, Italy, pp. 1802-1807, 2016.

[24] Aureli Somà, Fabio Bruzzese, Francesco Mocera and Ezio Viglietti, “Hybridization Factor and Performance of Hybrid Electric Telehandler Vehicle”, *IEEE Trans. on Ind. Appl.*, vol. 52, no. 6, pp. 5130–5138, Nov/Dec. 2016.

[25] Shuwei Zhang, Yugong Luo, Junmin Wang, Xiao Wang and Keqiang Li, “Predictive Energy Management Strategy for Fully Electric Vehicles Based on Preceding Vehicle Movement”, *IEEE Trans. Intel. Transport. Sys.*, vol. no. ,pp. , 2017.

[26] Furkan Akar, Yakup Tavlasoglu and Bulent Vural, “An Energy Management Strategy for a Concept Battery/Ultracapacitor Electric Vehicle With Improved Battery Life”, *IEEE Trans. Transport. Electrific.*, vol. 3, no. 1, pp. 191–200, Mar. 2017.

[27] Huang-Jen Chiu and Li-Wei Lin, “A Bidirectional DC–DC Converter for Fuel Cell Electric Vehicle Driving System”, *IEEE Trans. Power Electron.*, vol. 21, no. 4, pp. 950–958, July. 2006.

[28] Qingchun Wang, Kaushik Rajashekara, Yijiang Jia and Jie Sun, “A Real-time Vibration Suppression Strategy in Electric Vehicles”, *IEEE Trans. Veh. Technol.*, 2017, Early Acess.

[29] Christos T. Krasopoulos, Minos E. Beniakar and A. G. Kladas, “Velocity and Torque Limit Profile Optimization of Electric Vehicle Including Limited Overload”, *IEEE Trans. on Ind. Appl.*, vol. 53, no. 4, pp. 3907–3916, 2017.

[30] Bimal K. Bose and Robert L. Steigerwald, “A DC Motor Control System for Electric Vehicle Drive”, *IEEE Trans. on Ind. Appl.*, vol. IA-14, no. 6, pp. 565–572, Nov/Dec. 1978.

[31] M. Sri-Jayantha, Gordon F. Hayhoe and John J. Henry, “SCR-Controlled DC-

Motor Model for an Electric Vehicle Propulsion System Simulation", *IEEE Trans. on Ind. Electron.* vol. IE-31, no. 1, pp. 18–25, Feb. 1984.

[32] J. G. W. West, "DC, induction, reluctance and PM motors for electric vehicles", *Power Engineering Journal*, vol. 8, no. 2, pp. 77-88, 1994.

[33] "General Theory on Motors", http://mechatronics.mech.northwestern.edu/design_ref/actuators/motor_theory.html

[34] T.G. Wilson, P.H. Trickey, "D.C. Machine. With Solid State Commutation", AIEE paper I. CP62-1372, October 7, 1962

[35] Yaonan Wang, Xizheng Zhang, Xiaofang Yuan and Guorong Liu, "Position-Sensorless Hybrid Sliding-Mode Control of Electric Vehicles With Brushless DC Motor", *IEEE Trans. Veh. Technol.*, vol. 60, no. 2, pp. 421–432, 2011.

[36] Xiaohong Nian, Fei Peng and Hang Zhang, "Regenerative Braking System of Electric Vehicle Driven by Brushless DC Motor", *IEEE Trans. on Ind. Electron.* vol. 61, no. 10, pp. 5798–5808, Oct. 2014.

[37] Farshid Naseri, Ebrahim Farjah and Teymoor Ghanbari, "An Efficient Regenerative Braking System Based on Battery/Supercapacitor for Electric, Hybrid and Plug-In Hybrid Electric Vehicles with BLDC Motor", *IEEE Trans. Veh. Technol.*, vol. 66, no.5, pp. 3724–3738, 2016.

[38] "Module 4 Drives and Mechanisms Lecture 1 Elements of CNC machine tools: electric motors", http://nptel.ac.in/courses/112103174/module4/lec1/3.html

[39] Junzhi Yu, Wenhui Pei and Chenghui Zhang, "A Loss-Minimization Port-Controlled Hamilton Scheme of Induction Motor for Electric Vehicles", *IEEE/ASME Trans. Mechatronics*, vol. 20, no. 6, pp. 2645–2653, Dec. 2015.

[40] Mehdi Farasat, Andrzej M. Trzynadlowski and Mohammed Sami Fadali, "Efficiency improved sensorless control scheme for electric vehicle induction motors", *IET Electr. Syst. Transp.* vol. 4, no. 4, pp. 122–131, 2014.

[41] Woosuk Sung, Jincheol Shin and Yu-seok Jeong, "Energy-Efficient and Robust Control for High-Performance Induction Motor Drive With an Application in Electric Vehicles", *IEEE Trans. Veh. Technol.*, vol. 61, no. 8, pp. 3394–3405, 2012.

[42] Yang Liu, Jin Zhao, Rui Wang and Chengguang Huang, "Performance

Improvement of Induction Motor Current Controllers in Field-Weakening Region for Electric Vehicles", *IEEE Trans. Power Electron.*, vol. 28, no. 5, pp. 2468–2482, May. 2013.

[43] Xi Zhang, "Sensorless Induction Motor Drive Using Indirect Vector Controller and Sliding-Mode Observer for Electric Vehicles", *IEEE Trans. Veh. Technol.*, vol. 62, no. 7, pp. 3010–3018, 2013.

[44] "Construction of induction motor", http://www.theelectricalportal.com/2017/02/construction-of-induction-motor-stater.html

[45] Conggan Ma, Qinghe Liu, Dafang Wang, Qing Li and Lei Wang, "A Novel Black and White Box Method for Diagnosis and Reduction of Abnormal Noise of Hub Permanent-Magnet Synchronous Motors for Electric Vehicles", *IEEE Trans. on Ind. Electron.* vol. 63, no. 2, pp. 1153–1167, Feb. 2016.

[46] Conggan Ma, Qing Li, Liwei Deng, Chaoyi Chen, Qinghe Liu and Haibo Gao, "A Novel Sound Quality Evaluation Method of the Diagnosis of Abnormal Noise in Interior Permanent Magnet Synchronous Motors for Electric Vehicles", *IEEE Trans. on Ind. Electron.* vol. 64, no. 5, pp. 3883–3891, 2017.

[47] Conggan Ma, Qing Li, Qinghe Liu, Dafang Wang, Jiajun Gao, Huiyao Tang and Yanhua Sun, "Sound Quality Evaluation of Noise of Hub Permanent-Magnet Synchronous Motors for Electric Vehicles", *IEEE Trans. on Ind. Electron.* vol. 63, no. 9, pp. 5663–5673, Sep. 2016.

[48] Bochao Du, Shaopeng Wu, Shouliang Han and Shumei Cui, "Interturn Fault Diagnosis Strategy for Interior Permanent-Magnet Synchronous Motor of Electric Vehicles Based on Digital Signal Processor", *IEEE Trans. on Ind. Electron.* vol. 63, no. 3, pp. 1694–1706, 2016.

[49] Mehdi Salehifar, Ramin Salehi Arashloo, Manuel Moreno-Eguilaz, Vicent Sala and Luis Romeral, "Observer-based open transistor fault diagnosis and fault-tolerant control of five-phase permanent magnet motor drive for application in electric vehicles", *IET Power Electron.*, vol. 8, no. 1, pp. 76-87, 2015.

[50] Ki-Chan Kim, "A Novel Calculation Method on the Current Information of Vector

Inverter for Interior Permanent Magnet Synchronous Motor for Electric Vehicle", *IEEE Trans. Magn.*, vol. 50, no. 2, Feb. 2014.

[51] Yoshihiro Miyama, Moriyuki Hazeyama, Shota Hanioka, Norihiro Watanabe, Akihiro Daikoku and Masaya Inoue, "PWM Carrier Harmonic Iron Loss Reduction Technique of Permanent-Magnet Motors for Electric Vehicles", *IEEE Trans. on Ind. Appl.*, vol. 52, no. 4, pp. 2865–2871, 2016.

[52] Enrico Carraro and Nicola Bianchi, "Design and comparison of interior permanent magnet synchronous motors with non-uniform airgap and conventional rotor for electric vehicle applications", *IET Electr. Power Appl.*, vol. 8, no. 6, pp. 240–249, 2014.

[53] Yue Zhang, Wenping Cao, Sean McLoone and John Morrow, "Design and Flux-Weakening Control of an Interior Permanent Magnet Synchronous Motor for Electric Vehicles", *IEEE Trans. Appl. Supercond.*, vol. 20, no. 3, pp. 861–864, Jun. 2010.

[54] Jiabin Wang, Xibo Yuan and Kais Atallah, "Design Optimization of a Surface-Mounted Permanent-Magnet Motor With Concentrated Windings for Electric Vehicle Applications", *IEEE Trans. Veh. Technol.*, vol. 62, no. 3, pp. 1053–1064, 2013.

[55] Kukhyun Ahn, Alparslan Emrah Bayrak and Panos Y. Papalambros, "Electric Vehicle Design Optimization: Integration of a High-Fidelity Interior-Permanent-Magnet Motor Model", *IEEE Trans. Veh. Technol.*, vol. 64, no. 9, pp. 3870–3877, 2015.

[56] Athanasios Georgios Sarigiannidis, Minos E. Beniakar and Antonios G. Kladas, "Fast Adaptive Evolutionary PM Traction motor Optimization based on Electric Vehicle Drive Cycle", *IEEE Trans. Veh. Technol.*, vol. 66, no. 7, pp. 5762-5774, 2016.

[57] Jim Montague, "Motor Designs Get Moving",
http://www.controldesign.com/articles/2011/motordesign1103/

[58] Wei Hua, Ming Cheng and Gan Zhang, "A Novel Hybrid Excitation Flux-Switching Motor for Hybrid Vehicles", *IEEE Trans. Magn.*, vol. 45, no. 10, pp. 4728-4731, Oct. 2009.

[59] Hui Yang, Heyun Lin, Z. Q. Zhu, Dong Wang, Shuhua Fang and Yunkai Huang, "A Variable-Flux Hybrid-PM Switched-Flux Memory Machine for EV/HEV

Applications", *IEEE Trans. on Ind. Appl.,* vol. 52, no. 3, pp. 2203–2214, May/June, 2016.

[60] E. Sulaiman, T. Kosaka and N. Matsui, "High Power Density Design of 6-Slot–8-Pole Hybrid Excitation Flux Switching Machine for Hybrid Electric Vehicles", *IEEE Trans. Magn.*, vol. 47, no. 10, pp. 4453-4456, Oct. 2011.

[61] Olivier Maloberti, Rémi Figueredo, Claude Marchand, Yahya Choua, Dominique Condamin, Luc Kobylanski and Edouard Bommé, "3-D–2-D Dynamic Magnetic Modeling of an Axial Flux Permanent Magnet Motor With Soft Magnetic Composites for Hybrid Electric Vehicles", *IEEE Trans. Magn.*, vol. 50, no. 6, Jun. 2014.

[62] Sung-Il Kim, Sunghyuk Park, Taesang Park, Jinwoo Cho, Wonho Kim and Seongtaek Lim, "Investigation and Experimental Verification of a Novel Spoke-Type Ferrite-Magnet Motor for Electric-Vehicle Traction Drive Applications", *IEEE Trans. on Ind. Electron.*, vol. 61, no. 10, Oct. 2014.

[63] Sung-Il Kim, Jinwoo Cho, Sunghyuk Park, Taesang Park and Seongtaek Lim, "Characteristics Comparison of a Conventional and Modified Spoke-Type Ferrite Magnet Motor for Traction Drives of Low-Speed Electric Vehicles", *IEEE Trans. on Ind. Appl.*, vol. 49, no. 6, pp. 2516–2523, 2013.

[64] M. Kimiabeigi, J. D. Widmer, R. Long, Y. Gao, J. Goss, R. Martin, T. Lisle, J. M. Soler Vizan, A. Michaelides and B. Mecrow, "High-Performance Low-Cost Electric Motor for Electric Vehicles Using Ferrite Magnets", *IEEE Trans. on Ind. Electron.*, vol. 63, no. 1, Jan. 2016.

[65] Marco Ferrari, Nicola Bianchi, Alberto Doria and Emanuele Fornasiero, "Design of Synchronous Reluctance Motor for Hybrid Electric Vehicles", *IEEE Trans. on Ind. Appl.,* vol. 51, no. 4, pp. 3030–3040, 2015.

[66] Nicola Bianchi, Silverio Bolognani, Enrico Carraro, Mosè Castiello and Emanuele Fornasiero, "Electric Vehicle Traction Based on Synchronous Reluctance Motors", *IEEE Trans. on Ind. Appl.,* vol. 52, no. 6, pp. 4762–4769, 2016.

[67] Infolytica Corporation, "AC Synchronous Reluctance Machine for Traction Application", http://www.infolytica.com/en/applications/ex0185/

[68] E. Afjei, A. Siadatan, and H. Torkaman, "Magnetic modeling, prototyping, and

comparative study of a quintuple-set switched reluctance motor," *IEEE Trans. Magn.*, vol. 51, no. 8, Aug. 2015

[69] Shuanghong Wang, Qionghua Zhan, Zhiyuan Ma, and Libing Zhou, "Implementation of a 50-kW Four-Phase Switched Reluctance Motor Drive System for Hybrid Electric Vehicle", *IEEE Trans. Magn.*, vol. 41, no. 1, pp. 501 – 504, Jan. 2005

[70] B. Mecrow, E. El-Kharashi, J. Finch, and A. Jack, "Preliminary performance evaluation of switched reluctance motors with segmental rotors," *IEEE Trans. Energy Convers.*, vol. 19, no. 4, pp. 679–686, Dec. 2004.

[71] R. Vandana, S. Nikam and B. G. Fernandes, "High torque polyphase segmented switched reluctance motor with novel excitation strategy," *IET Elect. Power Appl.* vol. 6, no. 7, pp. 375-384, 2012.

[72] C. Lee, R. Krishnan, and N. S. Lobo, "Novel two-phase switched reluctance machine using common-pole E-core structure: Concept, analysis, and experimental verification," *IEEE Trans. Ind. Appl.*, vol. 45, no. 2, pp. 703–711, Mar./Apr. 2009.

[73] S.-G. Oh and R. Krishnan, "Two phase SRM with flux-reversal-free stator: Concept, analysis, design and experimental verification," *IEEE Trans. Ind. Appl.*, vol. 43, no. 5, pp. 1247–1257, Sep./Oct. 2007.

[74] H. Eskandari and M. Mirsalim, "An improved 9/12 two phase E-core switched reluctance machine," *IEEE Trans. Energy Convers.*, vol. 28, no. 4, pp. 951–958, Dec. 2013.

[75] Seyed Reza Mousavi-Aghdam, Mohammad Reza Feyzi, Nicola Bianchi, Mattia Morandin, "Design and Analysis of a Novel High-Torque Stator-Segmented SRM," *IEEE Trans. Ind. Electron.* , vol. 63, no. 3, pp. 1458-1466, Mar. 2016.

[76] H. Torkaman, E. Afjei, and M. S. Toulabi, "New double-layer-per-phase isolated switched reluctance motor: Concept, numerical analysis, and experimental confirmation," *IEEE Trans. Ind. Electron.*, vol. 59, no. 2, pp. 830–838, Feb. 2012.

[77] M. Abbasian, M. Moallem, and B. Fahimi, "Double stator switched reluctance motors: Fundamentals and magnetic force analysis," *IEEE Trans. Energy Convers.*, vol. 25, no. 3, pp. 589–597, Sep. 2010.

[78] E. Cosoroaba, W. Wang, and B. Fahimi, “Comparative study of two winding configurations for a double stator switched reluctance machine,” in *Proc. ICEM*, Sep. 2014, pp. 1013–1017.

[79] H. Arihara and K. Ataksu, “Basic properties of an axial-type switched reluctance motor,” *IEEE Trans. Ind. Appl.*, vol. 49, no. 1, pp. 59–65, Jan./Feb. 2013.

[80] S. Murakami, H. Goto, and O. Ichinokura, “A study about optimum stator pole design of axial-gap switched reluctance motor,” in *Proc. ICEM*, Sep. 2014, pp. 975–980.

[81] A. Labak and N. C. Kar, “Novel approaches toward leakage flux reduction in axial flux switched reluctance machines,” *IEEE Trans. Magn.*, vol. 49, no. 8, pp. 4738–4741, Aug. 2013.

[82] Yihua Hu, Chun Gan, Sideng Hu, Wenping Cao, Xiaoming Wang, Stephen Finney, “Winding-centre-tapped switched reluctance motor drive for multi-source charging in electric vehicle applications”, *IET Power Electron.*, vol. 8, no. 11, pp.2067-2075, 2015

[83] Yihua Hu, Chun Gan, Wenping Cao, Chushan Li, Stephen J. Finney, “Split Converter-Fed SRM Drive for Flexible Charging in EV/HEV Applications”, *IEEE Trans. on Ind. Electron.*, vol. 62, no. 10, pp. 6085 – 6095, Oct. 2015

[84] Yihua Hu, Chun Gan, Wenping Cao, Wuhua Li, Stephen J. Finney, “Central-Tapped Node Linked Modular Fault-Tolerance Topology for SRM Applications”, *IEEE Trans. Power Electron.*, vol. 31, no. 2, pp. 1541 – 1554, Feb. 2016

[85] Yihua Hu, Chun Gan, Wenping Cao, Jiangfeng Zhang, Wuhua Li, Stephen J. Finney, “Flexible Fault-Tolerant Topology for Switched Reluctance Motor Drives”, *IEEE Trans. Power Electron.*, vol. 31, no. 6, pp. 4654 – 4668, Jun. 2016

[86] Yihua Hu, Xueguan Song, Wenping Cao, Bing Ji, “New SR Drive With Integrated Charging Capacity for Plug-In Hybrid Electric Vehicles (PHEVs)”, *IEEE Trans. on Ind. Electron.*, vol. 61, no. 10, pp. 5722 – 5731, Oct. 2014

[87] Bulent Sarlioglu, Casey T. Morris, Di Han and Silong Li, “ Driving Toward Accessibility: A Review of Technological Improvements for Electrical Machines, Power Electronics, and Batteries for Electric and Hybrid Vehicles”, *IEEE Ind. Appl.*

Mag. vol. 23, no. 1, pp. 14-25, 2017

[88] P. Desai, M. Krishnamurthy, N. Schofield, and A. Emadi, "Novel switched reluctance machine configuration with higher number of rotor poles than stator poles: Concept to implementation," *IEEE Trans. Ind. Electron.*, vol. 57, no. 2, pp. 649–659, Feb. 2010.

[89] Berker Bilgin, Ali Emadi and Mahesh Krishnamurthy, "Design Considerations for Switched Reluctance Machines With a Higher Number of Rotor Poles," *IEEE Trans. Ind. Electron.* , vol. 59 , no. 10, pp. 3745-3756, Oct. 2012.

[90] Smaka, S., Masic, S., Hadzimejlic, N. and Cosovic, M., "Design considerations for novel 8/14 and comparison with conventional 8/6 and 8/10 switched reluctance machines". Int. Symp. Power Electronics, Electrical Drives, Automation and Motion (SPEEDAM), 2012, pp. 614 – 619.

[91] J. F. Lindsay, R. Arumugam, R. Krishnan, "Finite-element analysis characterization of a switched reluctance motor with multitooth per stator pole," *IEE Proceedings B, Elect. Power. Appl.* vol. 133, no. 6, pp. 347-353, Nov. 1986.

[92] J. Faiz, M. B. B. Sharifian, "Core Losses Estimation in a Multiple Teeth per Stator Pole Switched Reluctance Motor," *IEEE Trans. Magn.*, vol. 30, no. 2, pp. 189-195, Mar. 1994.

[93] Jawad Faiz, J.W. Finch, "Aspects of design optimization for multiple tooth per stator pole switched reluctance motors," *Electric Power Systems Research* 42, pp. 77-86, 1996.

[94] Saurabh P. Nikam, Vandana Rallabandi, B. G. Fernandes, "A High-Torque-Density Permanent-Magnet Free Motor for in-Wheel Electric Vehicle Application," *IEEE Trans. Ind. Appl.* vol. 48, no. 6, pp. 2287-2295, 2012.

[95] X. D. Xue, K.W.E. Cheng, T.W. Ng, and N. C. Cheung, "Multi-Objective Optimization Design of In-Wheel Switched Reluctance Motors in Electric Vehicles", *IEEE Trans. Ind. Electron.*, Vol. 57, No. 9, pp. 2980 – 2987, Sep. 2010.

[96] http://www.infomine.com/investment/metal-prices/copper/5-year/

[97] J. Widmer and B. Mecrow, "Optimised segmental rotor switched reluctance machines with a greater number of rotor segments than stator slots," in *Proc. IEEE*

IEMDC, May 2011, pp. 1183–1188.

[98] Saurabh P. Nikam, Vandana Rallabandi, B. G. Fernandes, "A High-Torque-Density Permanent-Magnet Free Motor for in-Wheel Electric Vehicle Application," *IEEE Trans. Ind. Appl.* vol. 48, no. 6, pp. 2287-2295, 2012.

[99] Vandana Rallabandi, Baylon Godfrey Fernandes, "Design procedure of segmented rotor switched reluctance motor for direct drive applications," *IET Elect. Power Appl.* vol. 8, no. 3, pp. 77-88, 2014.

[100] R.Krishnan, *Switched Reluctance Motor Drives-Modeling, Simulation, Analysis, Design and Applications.* Boca Raton, FL:CRC Press, 2001.

[101] K. T. Chau, Dong Zhang, J. Z. Jiang, Chunhua Liu, and Yuejin Zhang, "Design of a Magnetic-Geared Outer-Rotor Permanent-Magnet Brushless Motor for Electric Vehicles", *IEEE Trans. Magn.*, vol. 43, no. 6, pp. 2504 – 2506, Jun. 2007.

[102] Ping Zheng , Yi Sui , Jing Zhao , Chengde Tong , T.A. Lipo , and Aimeng Wang, "Investigation of a Novel Five-Phase Modular Permanent-Magnet In-Wheel Motor", *IEEE Trans. Magn.*, vol. 47, no. 10, pp. 4084 – 4087, Oct. 2011.

[103] Yu Hasegawa, Kenji Nakamura, and Osamu Ichinokura, "A Novel Switched Reluctance Motor with the Auxiliary Windings and Permanent Magnets", *IEEE Trans. Magn.*, vol. 48, no. 11, pp. 3855 – 3858, Nov. 2012.

[104] Pere Andrada, Balduí Blanqué, Eusebi Martínez, and Marcel Torrent, "A Novel Type of Hybrid Reluctance Motor Drive", *IEEE Trans. on Ind. Electron.*, vol. 61, no. 8, pp. 4337 - 4345, Aug. 2014.

[105] Hongsik Hwang, Sungwoo Bae, and Cheewoo Lee, "Analysis and Design of a Hybrid Rare-Earth-Free Permanent Magnet Reluctance Machine by Frozen Permeability Method", *IEEE Trans. Magn.*, vol. 52, no. 7, July. 2016.

[106] Qiang Yu, Xuesong Wang, and Yuhu Cheng, "Magnetic Modeling of Saliency Effect for Saturated Electrical Machines with a New Calculation Method", *IEEE Trans. Magn.*, vol. 52, no. 6, Jun. 2016.

[107] Guozhi Huang, Fengli Fu, "Design Handbook of Middle and Small-sized Rotary Motors" (in Chinese), China Electric Power Press, 2007.